DOCTORAL THESIS

End-to-end performance simulations of infrared vortex coronagraphs for extremely large telescopes.

Author:
Brunella CARLOMAGNO

Advisor:
Dr. Olivier ABSIL

Jury members:
Pr. Serge HABRAKEN
Dr. Christian DELACROIX
Dr. Gilles ORBAN DE XIVRY
Pr. Jean SURDEJ
Dr. Pierre BAUDOZ
Pr. Matthew KENWORTHY

Dissertation submitted in partial fullfilment of the requirements for the degree of Doctor of Science

Faculty of Sciences
Université de Liège

May 2023

Per Charlotte

Acknowledgements

First and foremost, I would like to express my sincere gratitude to my advisor, Olivier, for believing in this thesis more than me. I have enjoyed very much working with him, and I am deeply grateful for the support, accademic and personal, that he has given me all these years. His dedication to his job and his caring guidance are inspiring, and I am very happy he gave me the opportunity to be part of this project. A special thanks to Jean, for his kind and wise words.
I would also like to extend my thanks to the members of the jury for accepting to evaluate my work: Serge Habraken, Pierre Baudoz, Matt Kenworthy.
I want to thank the members of the VORTEX team and colleagues from Uliège: Aissa, Bikram, Carlos, Christian, Chloi, Elsa, Gilles, Maddalena, Valentin. Thank you for the discussions, the evening parties, the lunches. It has been a real priviledge to work with you, and I am very grateful for your friendship and unlimited support.

Vorrei ringraziare i miei amici, Anna, Antonella, Barbara, Elena, Marco Lucio, Marianna, Mirko. Siamo amici da tanti anni, e riuscite sempre a trovare il modo di coccolarmi: che sia una canzone inventata di sana pianta, o un corso di cucito, o un pomeriggio di relax a mangiare gelato. Vi sono grata per l'aiuto che mi avete dato, anche se non ve lo dico spesso. Vi ringrazio per essere sempre lì al mio fianco, a sostenermi e ad aiutarmi a raccogliere i pezzi, quando tutto va in frantumi.
Infine, vorrei ringraziare la mia famiglia: mia mamma, mia sorella Giusi, i miei nipotini Pinuccio e Linuccio, e Paolo. Facciamo sempre tanti progetti, ma a volte la vita decide per noi. Vi sono grata per l'amore e il sostegno che mi date, e, anche se siamo lontani, vi sento sempre vicini.

Je ne pourrais que terminer cette liste par toi, Romain. Je te remercie pour ton soutien et ta patience envers mes mille phobies. Je te remercie pour ton enthousiasme contagieux, parce que tu me montres toujours le coté lumineux du monde. Je te remercie de partager avec moi cette vie qui nous a frappé si fort, et pourtant tu es toujours là, à mes cotés. Je t'aime, et je n'aurais pas pu faire grand chose sans toi.

Questa tesi é per te, mia piccola stella.

Abstract

Since the first discovery of an exoplanet in the 1990s, the number of confirmed exoplanets has increased exponentially, with several ground-and space-based missions dedicated to exoplanet detection. Most of these detections have been obtained via indirect methods, in which the presence of the exoplanets is derived by its effect on the host star. Direct detection methods, in which the exoplanet is observed directly, are still in the background, but the improvement of hardware and software techniques is progressively closing the gap with the most successful detection methods. The Extremely Large Telescope (ELT) is one of the most anticipated telescopes of the next years. With its 39m diameter, it will be the biggest eye on the universe in the optical/infrared range. It will be equipped with three state-of-the-art instruments: HARMONI (the high angular optical and near-infrared spectrograph), MICADO (the imaging camera for deep observations) working in tandem with MORFEO (the multiconjugate adaptive optics system), and METIS (the mid-infrared imager and spectrograph). One of the main science cases for the latter is direct detection of exoplanets, and, for this purpose, it will be equipped with two of the most advanced coronagraphs, the apodized phase plate (APP) and the vortex coronagraph (VC). In this dissertation, we present the results of our work on the preparation of the high-contrast imaging modes of METIS. The coronagraphs are optimized for the instrument wavebands, and end-to-end performance simulations are performed for several instrumental and environmental parameters. The expected observational capabilities of the METIS instrument show the great leap in sensitivity to faint companions in the thermal infrared regime that the instrument will enable.

Resumé

Depuis la découverte de la première exoplanète dans les années 90, le nombre de exoplanètes confirmées a augmenté exponentiellement, avec plusieurs missions dédiées à la détection d'exoplanètes. La plupart de ces détections ont été obtenues via des méthodes indirectes, où la présence de l'exoplanète est dérivée par son effet sur l'étoile hôte. Les méthodes de détection directe, pour lesquelles la planète est observée directement, sont encore en second plan, mais l'amélioration des techniques de hardware et software permet de combler la distance avec les méthodes les plus fructueuses. Le Extremely Large Telescope (ELT) est l'un des télescopes les plus attendus dans les prochaines années. Avec un diamètre de 39m, il représentera le plus grand œil sur l'univers depuis la Terre. Il sera équipé de trois instruments de pointe: HARMONI (le spectrographe à champ intégral en visible et proche infrarouge), MICADO (la caméra observant dans le proche infrarouge) en collaboration avec MORFEO (le système d'optique adaptative), et METIS (le spectrographe imageur en moyen infrarouge). Un des objectifs de ce dernier instrument est la détection directe d'exoplanètes, et il sera donc équipé de deux coronographes parmi les plus efficaces, la Apodized Phase Plate (APP) et le Vortex Coronagraph (VC). Dans cette dissertation, nous présentons les résultats de notre travail sur la préparation des modes d'imagerie à haut contraste de l'instrument METIS. Les coronographes sont optimisés pour les longueurs d'ondes de l'instrument, et les performances sont simulées de bout en bout pour plusieurs paramètres instrumentaux et environnementaux. Les capacités observationnelles attendues de METIS montrent le grand bond en sensitivité pour la détection de compagnons faibles dans le régime de l'infrarouge thermique.

Contents

List of Figures

List of Tables

List of publications

PEER-REVIEWED JOURNALS

- G. J. Ruane, E. Huby, O. Absil, D. Mawet, C. Delacroix, B. Carlomagno, and G. A. Swartzlander (2015a). *Lyot-plane phase masks for improved high-contrast imaging with a vortex coronagraph*. A&A, 583, A81, A81.
- E. Vargas Catalán, E. Huby, P. Forsberg, A. Jolivet, P. Baudoz, B. Carlomagno, C. Delacroix, S. Habraken, D. Mawet, J. Surdej, O. Absil, and M. Karlsson (2016). *Optimizing the subwavelength grating of L-band annular groove phase masks for high coronagraphic performance*. A&A, 595, A127, A127.
- D. Mawet, E. Choquet, O. Absil, E. Huby, M. Bottom, E. Serabyn, B. Femenia, J. Lebreton, K. Matthews, C. A. Gomez Gonzalez, O. Wertz, B. Carlomagno, V. Christiaens, D. Defrère, C. Delacroix, P. Forsberg, S. Habraken, A. Jolivet, M. Karlsson, J. Milli, C. Pinte, P. Piron, M. Reggiani, J. Surdej, and E. Vargas Catalan (2017). *Characterization of the Inner Disk around HD 141569 A from Keck/NIRC2 L-Band Vortex Coronagraphy*. AJ, 153.1, 44, p. 44.
- E. Serabyn, E. Huby, K.Matthews, D. Mawet, O. Absil, B. Femenia, P. Wizinowich, M. Karlsson, M. Bottom, R. Campbell, B. Carlomagno, D. Defrère, C. Delacroix, P. Forsberg, C. Gomez Gonzalez, S. Habraken, A. Jolivet, K. Liewer, S. Lilley, P. Piron, M. Reggiani, J. Surdej, H. Tran, E. Vargas Catalan, O. Wertz (2017). *The W. M. Keck Observatory Infrared Vortex Coronagraph and a First Image of HIP 79124 B*. AJ, 153.1, 43, p. 43.
- M. Reggiani, V. Christiaens, O. Absil, D. Mawet, E. Huby, E. Choquet, C. A. Gomez Gonzalez, G. Ruane, B. Femenia, E. Serabyn, K. Matthews, M. Barraza, B. Carlomagno, D. Defrère, C. Delacroix, S. Habraken, A. Jolivet, M. Karlsson, G. Orban de Xivry, P. Piron, J. Surdej, E. Vargas Catalan, and O. Wertz (2018). *Discovery of a point-like source and a third spiral arm in the transition disk around the Herbig Ae starMWC758*. A&A, 611, A74, A74.
- S. Hippler, M. Feldt, T. Bertram, W. Brandner, F. Cantalloube, B. Carlomagno, O. Absil, A. Obereder, I. Shatokhina, and R. Stuik (2019). *Single conjugate adaptive optics for the ELT instrument METIS*. Experimental Astronomy 47.1-2, pp. 65105.
- B. Carlomagno, C. Delacroix, O. Absil, F. Cantalloube, G. Orban de Xivry, P. Pathak, T. Agocs, T. Bertram, B. Brandl, L. Burtscher, D. Doelman, M. Feldt, A. Glauser, S. Hippler, M. Kenworthy, E. Por, F. Snik, R. Stuik, and R. van Boekel (2020). *METIS high-contrast imaging: design and expected performance*. JATIS, 6, 035005, p. 035005.
- D. S. Doelman, F. Snik, E. H. Por, S. P. Bos, G. P. P. L. Otten, M. Kenworthy, S. Y. Haffert, M. Wilby, A. J. Bohn, B. J. Sutlieff, K. Miller, M. Ouellet, J. de Boer, C. U. Keller, M. J. Escuti, S. Shi, N. Z. Warriner, K. Hornburg, J. L. Birkby, J. Males, K. M. Morzinski, L. M. Close, J. Codona, J. Long, L. Schatz, J. Lumbres, A. Rodack, K. Van Gorkom, A. Hedglen, O. Guyon, J. Lozi, T. Groff, J. Chilcote, N. Jovanovic, S. Thibault, C. de Jonge, G. Allain, C. Vallée, D. Patel, O. Côté, C. Marois, P. Hinz, J. Stone, A. Skemer, Z. Briesemeister, A. Boehle, A. M. Glauser,W. Taylor, P. Baudoz, E. Huby, O. Absil, B. Carlomagno, and C. Delacroix (2021). *Vector-apodizing phase plate coronagraph: design, current performance, and future development [Invited]*. AO, 60.19, p. D52.

- R. Bowens, M. R. Meyer, C. Delacroix, O. Absil, R. van Boekel, S. P. Quanz, M. Shinde, M. Kenworthy, B. Carlomagno, G. Orban de Xivry, F. Cantalloube, and P. Pathak (2021). *Exoplanets with ELT-METIS. I. Estimating the direct imaging exoplanet yield around stars within 6.5 parsecs*. A&A, 653, A8, A8.

NON-PEER-REVIEWED JOURNALS AND CONTRIBUTIONS TO INTERNATIONAL CONFERENCES

- O. Absil, D. Mawet, C. Delacroix, P. Forsberg, M. Karlsson, S. Habraken, J. Surdej, P.-A. Absil, B. Carlomagno, V. Christiaens, D. Defrère, C. Gomez Gonzalez, E. Huby, A. Jolivet, J. Milli, P. Piron, E. Vargas Catalan, and M. Van Droogenbroeck (2014). *The VORTEX project: first results and perspectives*. Adaptive Optics Systems IV. Vol 9148, Proc. SPIE, p. 91480M.

- P. Forsberg, E. Vargas, C. Delacroix, O. Absil, B. Carlomagno, D. Mawet, S. Habraken, J. Surdej, and M. Karlsson (2014). *Realizing the diamond annular groove phase masks for the mid infrared region: five years of successful process development of diamond plasma etching*. Advances in Optical and Mechanical Technologies for Telescopes and Instrumentation, Vol. 9151. Proc. SPIE, p. 44.

- C. Delacroix, O. Absil, B. Carlomagno, P Piron, P Forsberg, M Karlsson, D Mawet, S Habraken, and J Surdej (2014). *Development of a subwavelength grating vortex coronagraph of topological charge 4 (SGVC4)*. Ground-based and Airborne Instrumentation for Astronomy V. Vol. 9147. Proc. SPIE, p. 91478Y.

- B. Carlomagno, C. Delacroix, O. Absil, P. Forsberg, S. Habraken, A. Jolivet, M. Karlsson, D. Mawet, P. Piron, J. Surdej, and E. Vargas Catalan (2014). *Mid-IR AGPMs for ELT applications*. Ground-based and Airborne Instrumentation for Astronomy V. Vol. 9147. Proc. SPIE, p. 914799.

- D. Defrere, O. Absil, D. Mawet, K. Michael, S. Habraken, J. Surdej, P.-A. Absil, B. Carlomagno, V. Christieans, C. Delacroix, J. Girard, P. Forsberg, C. Gonzalez Gomez, P. Hinz, E. Huby, A. Jolivet, J. Milli, E. Pantin, P. Piron, E. Serabyn, M. Van Droogenbroeck, E. Vargas Catalan, and O. Wertz (2015). *Direct exoplanet imaging with small-angle Vortex coronagraphs*. Pathways Towards Habitable Planets, p. 89

- G. J. Ruane, O. Absil, E. Huby, D. Mawet, C. Delacroix, B. Carlomagno, P. Piron, and G. A. Swartzlander (2015b). *Optimized focal and pupil plane masks for vortex coronagraphs on telescopes with obstructed apertures*. Techniques and Instrumentation for Detection of Exoplanets VII. Vol. 9605. Proc. SPIE, p. 96051I.

- B. Femenía Castellá, E. Serabyn, D. Mawet, O. Absil, P. Wizinowich, K. Matthews, E. Huby, M. Bottom, R. Campbell, D. Chan, B. Carlomagno, S. Cetre, D. Defrère, C. Delacroix, C. Gomez Gonzalez, A. Jolivet, M. Karlsson, K. Lanclos, S. Lilley, S. Milner, H. Ngo, M. Reggiani, J. Simmons, H. Tran, E. Vargas Catalan, and O. Wertz (2016). *Commissioning and first light results of an L-band vortex coronagraph with the Keck II adaptive optics NIRC2 science instrument*. Adaptive Optics Systems V. Vol. 9909. Proc. SPIE, p. 990922.

- B. Carlomagno, O. Absil, M. Kenworthy, G. J. Ruane, C. U. Keller, G. Otten, M. Feldt, S. Hippler, E. Huby, D. Mawet, C. Delacroix, J. Surdej, S. Habraken, P. Forsberg, M. Karlsson, E. Vargas Catalan, and B. R. Brandl (2016). *End-to-end simulations of the E-ELT/METIS coronagraphs*. Adaptive Optics Systems V. Vol. 9909. Proc. SPIE, p. 990973.

- O. Absil, D. Mawet, M. Karlsson, B. Carlomagno, V. Christiaens, D. Defrère, C. Delacroix, B. Femenía Castella, P. Forsberg, J. Girard, C. A. Gómez González, S. Habraken, P. M. Hinz, E. Huby, A. Jolivet, K. Matthews, J. Milli, G. Orban de Xivry, E. Pantin, Pi. Piron, M. Reggiani, G. J. Ruane, G. Serabyn, J. Surdej, K. R. W. Tristram, E. Vargas Catalán, O. Wertz, and P. Wizinowich (2016a). *Three years of harvest with the vector vortex coronagraph in the thermal infrared*. Ground-based and Airborne Instrumentation for Astronomy VI. Vol. 9908. Proc. SPIE, p. 99080Q.

- M. Kasper, R. Arsenault, H. U. Käufl, G. Jakob, E. Fuenteseca, M. Riquelme, R. Siebenmorgen, M. Sterzik, G. Zins, N. Ageorges, S. Gutruf, A. Reutlinger, D. Kampf, O. Absil, B. Carlomagno, O. Guyon, P. Klupar, D. Mawet, G. Ruane, M. Karlsson, E. Pantin, and K. Dohlen (2017). *NEAR: Low-mass Planets in a Cen with VISIR*. The Messenger 169, pp. 1620.

- H.-U. Käufl, M. Kasper, R. Arsenault, G. Jakob, S. Leveratto, G. Zins, E. Fuenteseca, M. Riquelme, R. Siebenmorgen, M. Sterzik, N. Ageorges, S. Gutruf, D. Kampf, A. Reutlinger, O. Absil, B. Carlomagno, O. Guyon, P. Klupar, D. Mawet, G. J. Ruane, M. Karlsson, E. Pantin, and K. Dohlen (2018). *NEAR: new earths in the Alpha Cen Region (bringing VISIR as a visiting instrument to ESO-VLT-UT4)*. Ground-based and Airborne Instrumentation for Astronomy VII. Vol. 10702. Proc. SPIE, p. 107020D.

- M. Kenworthy, O. Absil, B. Carlomagno, T. Agócs, E. Por, S. Bos, B. Brandl, and F. Snik (2018). *A review of high contrast imaging modes for METIS*. Ground-based and Airborne Instrumentation for Astronomy VII. Vol. 10702. Proc. SPIE, p. 10702A3.

- T. Bertram, O. Absil, P. Bizenberger, W. Brandner, F. Briegel, F. Cantalloube, B. Carlomagno, M. Concepción Cárdenas Vázquez, M. Feldt, A. Glauser, T. Henning, S. Hippler, A. Huber, N. Hurtado, M. Kenworthy, M. Kulas, L. Mohr, V. Naranjo, P. Neureuther, A. Obereder, R.- R. Rohloff, S. Scheithauer, I. Shatokhina, R. Stuik, and R. van Boekel (2018). *Single conjugate adaptive optics for METIS*. Adaptive Optics Systems VI. Vol. 10703. Proc. SPIE, p. 1070314.

- N. Jovanovic, O. Absil, P. Baudoz, M. Beaulieu, M. Bottom, E. Cady, B. Carlomagno, A. Carlotti, D. Doelman, K. Fogarty, R. Galicher, O. Guyon, S. Haffert, E. Huby, J. Jewell, C. Keller, M. Kenworthy, J. Knight, J. Kuhn, K. Miller, J. Mazoyer, M. NDiaye, E. Por, L. Pueyo, A. J. E. Riggs, G. J. Ruane, D. Sirbu, F. Snik, J. K. Wallace, M. Wilby, and M. Ygouf (2018). *Review of high-contrast imaging systems for current and future ground-based and space-based telescopes: Part II. Common path wavefront sensing/control and coherent differential imaging*. Adaptive Optics Systems VI. Vol. 10703. Proc. SPIE, p. 107031U.

- F. Snik, O. Absil, P. Baudoz, M. Beaulieu, E. Bendek, E. Cady, B. Carlomagno, A. Carlotti, N. Cvetojevic, D. Doelman, K. Fogarty, R. Galicher, O. Guyon, S. Haffert, E. Huby, J. Jewell, N. Jovanovic, C. Keller, M. Kenworthy, J. Knight, J. Kuhn, J. Mazoyer, K. Miller, M. NDiaye, B. Norris, E. Por, L. Pueyo, A. J. Eldorado Riggs, G. J. Ruane, D. Sirbu, J. Kent Wallace, M. Wilby, and M. Ygouf (2018). *Review of high-contrast imaging systems for current and future ground-based and space-based telescopes III: technology opportunities and pathways*. Advances in Optical and Mechanical Technologies for Telescopes and Instrumentation III. Vol. 10706. Proc. SPIE, p. 107062L.

- G. J. Ruane, A. Riggs, J. Mazoyer, E. H. Por, M. NDiaye, E. Huby, P. Baudoz, R. Galicher, E. Douglas, J. Knight, B. Carlomagno, K. Fogarty, L. Pueyo, N. Zimmerman, O. Absil, M. Beaulieu, E. Cady, A. Carlotti, D. Doelman, O. Guyon, S. Haffert, J. Jewell, N. Jovanovic, C. Keller, M. A. Kenworthy, J. Kuhn, K. Miller, D. Sirbu, F. Snik, J. Kent Wallace, M. Wilby, and M. Ygouf (2018). *Review of high-contrast imaging systems for current and future ground- and space-based telescopes I: coronagraph design methods and optical performance metrics*. Space Telescopes and Instrumentation 2018: Optical, Infrared, and Millimeter Wave. Vol. 10698. Proc. SPIE, p. 106982S.

- C. Delacroix, O. Absil, G. Orban de Xivry, M. Shinde, P. Pathak, F. Cantalloube, B. Carlomagno, V. Christiaens, A. Boné, D. Dolkens, M. Kenworthy, and D. Doelman (2022). *The High-contrast End-to-End Performance Simulator (HEEPS): influence of ELT/METIS instrumental effects*. Modeling, Systems Engineering, and Project Management for Astronomy X. Vol. 12187. Proc. SPIE, p. 121870F.

Part I

Science background

Chapter 1

Introduction

Since the first discovery of an exoplanet in the 1990s, the interest around possible planets orbiting other stars has increased exponentially. Several ground- and space-based telescopes have been designed and built with as major objective to detect exoplanets: from the James Webb Space Telescope (JWST), to the Extremely Large Telescope (ELT), with many more small-scale experiments like the TRAPPIST telescope. The increasing number of discoveries has fed the exoplanetary science field with crucial insight about planet formation, their evolution, their structure. If biosignatures have not been detected yet, the continuous improvement of hardware and software techniques has certainly made it closer. The first (and most) exoplanets have been detected via indirect methods, which analyse the effect of the companion on the parent star. These methods have been extremely successful over the years, leading to the discovery of almost 5000 exoplanets, between ground- and space-based projects. Between them, the Kepler space telescope has certainly broken all records, by detecting 2662 confirmed exoplanets (as of 05/2022).

1.1 Context of the thesis

The detection of exoplanets has inspired many researchers for years, leading to the first ever detection around pulsar PSR B1257 +12 (Wolszczan et al., 1992) and the first exoplanet around a Sun-like star, 51 Peg (Mayor et al., 1995). In less than 30 years, the number of confirmed exoplanets has jumped to more than 5000 (as of 07/2023, see Fig. 1.1) with many more still in the confirmation process.

Figure 1.1 shows the number of exoplanets detected per year and per detection method. The big majority of these exoplanets have been discovered via indirect methods (see Sect. 1.3), in particular transit and radial velocity. The launch of the James Webb Space Telescope (JWST), and the planned construction of three giant segmented mirror telescopes, among which the Extremely Large Telescope (ELT), are creating the perfect environment for a substantial increase in these numbers. The study of exoplanets has two major objectives: to establish a more complete understanding of the existing exoplanets and planetary systems; and to constrain the formation and evolution process of these objects. An implicit wish is to find exoplanets similar to Earth, that could shelter life. From these two objectives, we can derive two major observational components: the first one consists in detecting exoplanets (with indirect, see Sect. 1.3, and direct, see Chapt. 2, techniques), and the second one is the characterisation of these objects (mass, radius, orbital parameters, chemical components), mostly done by integrating several techniques (detection methods and spectroscopy, for example). Both are strongly linked to the theoretical aspects of the exoplanetary science, whose fundamentals are presented in Sect. 1.2.

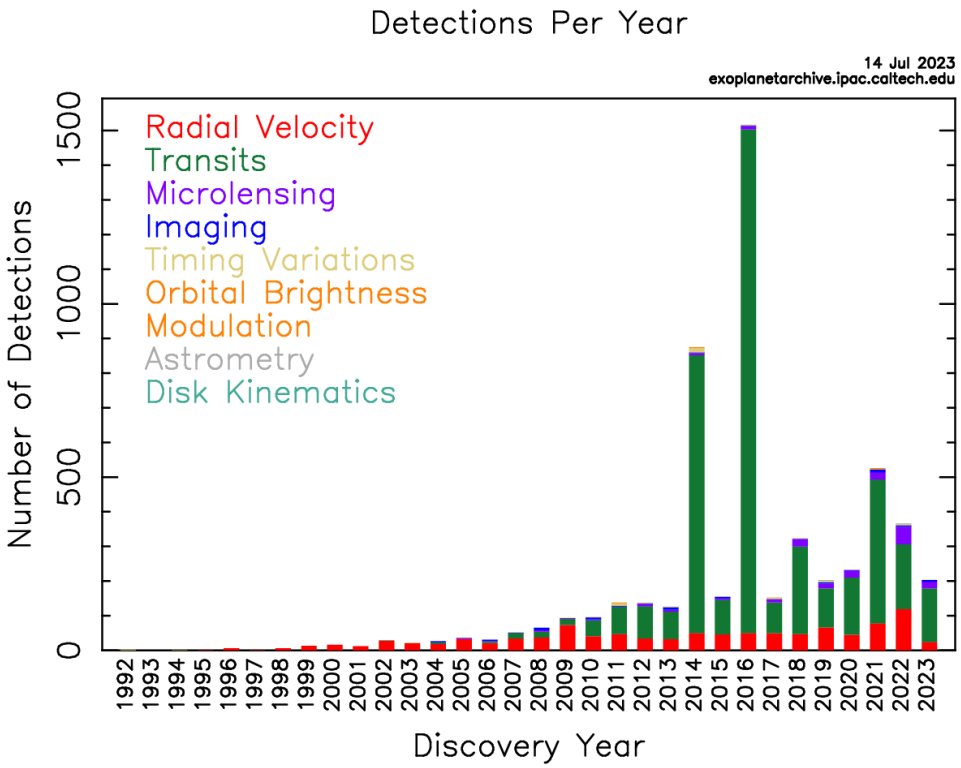

FIGURE 1.1: Number of confirmed exoplanets detected per year per detection method (up to July 2023). The high number of detected exoplanets in the latest years via transit is mostly due to the space telescope Kepler, which has discovered more than 2000 planets since its launch in 2009. Credits: Caltech https://exoplanetarchive.ipac.caltech.edu/exoplanetplots/.

1.2 Exoplanets

The definition of a (exo)planet has been debated over the years. Not every object orbiting around a star is a planet: the most famous example is the declassification of Pluto as a dwarf planet following the International Astronomical Union (IAU) definition of a planet. For the IAU, a planet is an object:

1. orbiting around a star (as the Sun) or an evolution of a star (as a pulsar or a white dwarf);
2. with a mass sufficently large to develop a spherical shape due to its gravity;
3. it must have cleared the neighborhood around its orbit;
4. with mass lower than $\sim 13 M_{Jup}$ (corresponding to the minimal mass to start burning deuterium). Between $\sim 13 M_{Jup}$ and $\sim 80 M_{Jup}$ (minimal mass to burn hydrogen), the celestial object is defined as a brown dwarf.

This last distinction between a planet and a brown dwarf, linked to the mass of the object, is more a practical one, because it is relatively easier to estimate the mass of an object. However, from a theoretical point of view, two other characteristics should be considered: the formation process and the internal structure and composition. Brown dwarfs are thought to be formed by gravitational collapse of a cold interstellar cloud of gas and dust, as stars, and have a small quantity of metals. On

the contrary, planets are thought to be formed in a circumstellar disk and their metal fraction to be quite significant. Planets formed in a circumstellar disk with mass higher than $\sim 13 M_{Jup}$ have been detected, together with object with an accretion disk (as stars) with a mass lower than $\sim 13 M_{Jup}$: this mass limit should therefore not be considered as firm.

1.2.1 Exoplanet formation and evolution process

Planets are formed alongside the star, in a protoplanetary disk, built around the star during the gravitational collapse of the cold interstellar cloud. This disk is formed essentially of gas (hydrogen and helium), volatile elements (like water, methane, ammonia, carbon monoxide, and carbon dioxide; with low condensation temperature, between 10 and 200K), and refractory elements (like silicates and metals, as nickel or aluminium, with high condensation temperature). It shows a temperature gradient: close to the star, the temperature is so high that only gas is allowed, while further away, because of the lower temperature, refractory elements are present in solid form. Behind a certain distance from the star, called the *snow line* (which depends on the temperature of the star itself), water and other volatile elements condense on the dust grains.
At the beginning of the planet formation process, the dust grains about $1 - 10 \mu m$ in size settle on the disk plane. By collision and accretion (*core accretion* theory), these grains create bigger objects ($0.01 - 10 m$). Further collisions allow the formation of planetesimals, km-sized objects kept together by their own gravity. The gravitational force between these objects deviates their orbit, causing new collisions. A subsequent phase of rapid accretion, called *runaway accretion*, forms planetary embryos, of about $100 km$ diameter. At this point, the biggest embryo grows by collision with the neighbouring planetesimals, creating protoplanets of about few thousands kilometer diameter. Inside the snow line, these protoplanets will evolve, by accretion and collision, into terrestrial planets.

For the formation of giant planets in the circumstellar disk, two major theories exist: the *core accretion* (see Fig. 1.2, a), and the *disk gravitational instability* (see Fig. 1.2, b). In the *core accreation* theory (Safronov, 1969), a solid core of $\sim 5 - 10 M_{\oplus}$ is formed behind the snow line, by a rapid accretion of refractory and volatile elements. Now sufficiently massive, the planetesimal traps the gas of the circumstellar disk. If this gas layer is extensive, the planet is a gas giant (like Jupiter), while, if the gas in the disk is rapidly exhausted, an ice giant is formed (like Nepture or Uranus). This theory can explain several features observed in our Solar System together with other planetary systems: the metal accumulation of Jupiter and Saturn with respect to the Sun, a correlation between the presence of giant planets and the metallicity of the disk, the small number of planets at big separation ($> 100 AU$), where the disk density is weaker. However, the duration of the planet formation is of the same order of magnitude as the typical lifespan of the disk, which is not compatible with the presence of planets at larger separation ($> 20 AU$), for which the formation would be too slow. A second issue is the presence of *hot Jupiters*, very close to the star: the in-situ formation process cannot explain the presence of these planets, because, on one side, the temperature in these regions is too high for solid particles to condensate to create the solid core; and on the other side, the gas necessary to create these gaseous planets is insufficient so close to the star, because of the star itself. The only possiblity would be that these planets are formed far from the star and, through a *migration process*, they are forced to migrate close in the inner region.
At least three different migration mechanisms have been proposed:

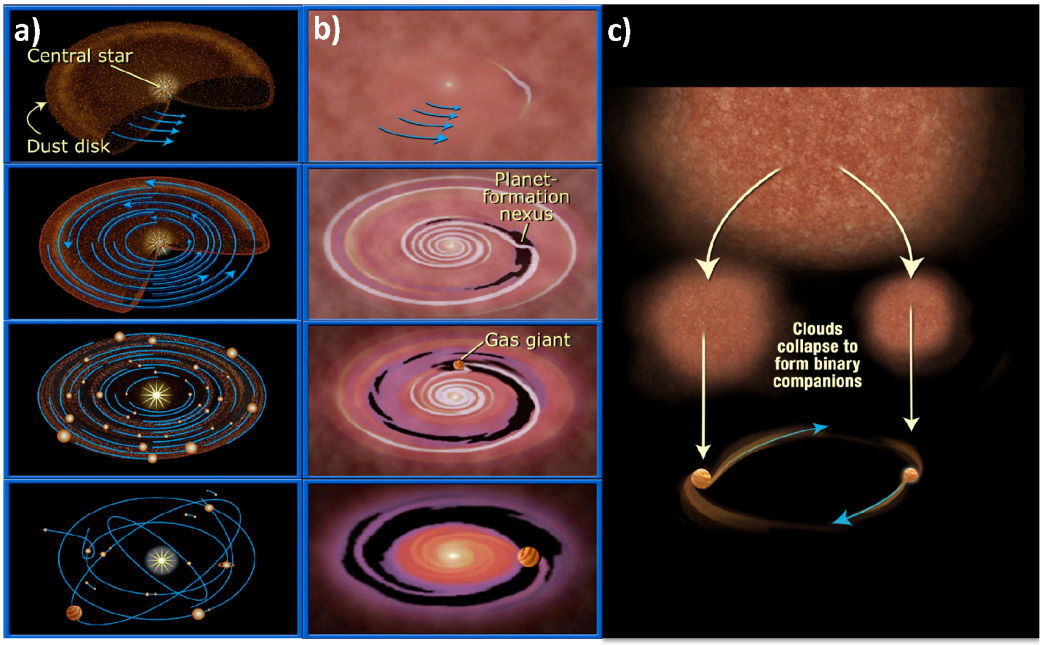

FIGURE 1.2: Possible mechanisms for giant planets formation. **a)** By core accretion in the protoplanetary disk, the dust grains collide to form protoplanets (first and second image). Giant planets attract gas (third image). The interaction between planets may lead to planet migration and ejection. **b)** By gravitational instability, a zone of the disk collapses to form a protoplanet. **c)** Companions can be formed by collapsing of a fragmented molecular cloud, as for brown dwarves and stars. Credits: NASA, ESA, and A. Feild (STScI)

1. Gravitational interaction between two or more Jupiter mass planets would result in the ejection of one or more planets, leaving one close to the star (Rasio et al., 1996, Weidenschilling et al., 1996). However, this mechanism cannot explain the high number of hot Jupiters.

2. Migration instability (Malhotra, 1993, Murray et al., 1998): the interaction between the planet and close planetesimals would force the planets to migrate closer to the star, while ejecting the planetesimals outside. However, this would imply a very massive disk, which is very unlikely.

3. Tidal interaction between the protoplanet and the gas (Goldreich et al., 1979, Lin et al., 1979): the disk-planet interaction induces an angular momentum exchange between the planet and the disk material. Three possible causes have been identified: wave excitation (called *type I* migration, Ward, 1997, see Fig. 1.3, a), a combination of wave excitation and shock dissipation (called *type II* migration, Lin et al., 1986, see Fig. 1.3, b), and direct exchange with disk material traversing the orbit (called *type III* migration, Masset et al., 2003)

The *disk gravitational instability* theory (Boss, 2001, see Fig. 1.2, b) allows to rapidly create giant planets. In the disk, a gravitational perturbation causes an instability in the disk itself, creating spiral pertubations (see Fig. 1.2, b, first image). The dust and gas layer of the plane of the disk could reach, locally, a density sufficiently high to form an object, a protoplanet, kept by its own gravity (see Fig. 1.2, b, second image). This theory seems to work quite well for massive disks and planets at large separation (mostly detected by direct methods). However, the high metallicity of giant

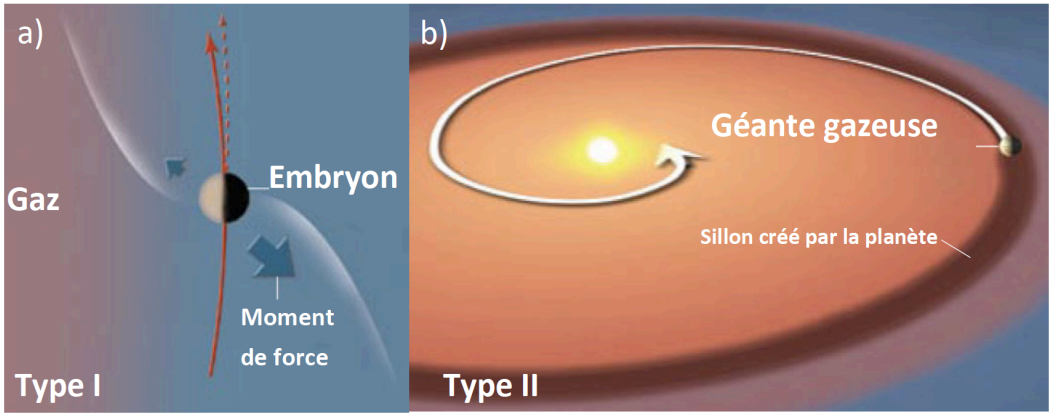

FIGURE 1.3: Possible mechanisms for planets migration. **a)** Type I: The migration is due to the interaction between a small body and the disk gas. **a)** Type II: The migration is caused by the contraction of the disk, due to the groove created by the massive planet. Credits: Lin et al., 2009

planets, as Jupiter and Saturn, cannot be explained by this theory.
Finally, there are planets too far from the star to be formed in the protoplanetary disk: these objects could have been formed by the contraction of the molecular cloud, during the star formation process (see Fig. 1.2, c).
Unlike stars, planets do not have nuclear reaction inside their core and they cool down throughout their life. A young object has a larger radius than later in its life, and the luminosity is higher for a hot, massive, and young planet. The classic core accretion models consider a very hot adiabatic sphere as a starting point, while more modern models predict a colder one. These differences are quite important for young objects, and the direct detection methods, which observe mainly hot (and brighter) planets, can have a huge impact in the study of these evolution models.

1.2.2 Exoplanet composition and atmosphere spectral properties

Following our Solar System, we can identify two major groups of planets: the *terrestrial planets*, and the *giant planets*. The *terrestrial planets* (Wanke, 1981) have a metallic core, with a silicate mantle and a rocky crust, which lead to a higher density (e.g. $> 5 g/cm^3$ for the Earth and Venus). The atmosphere, when present, represents a small percentage of the total mass. The *giant planets* (Hubbard et al., 2002) are very massive ($> 10 M_\oplus$), with a core made of rocks, metals, and ice of about $10 M_\oplus$, and a gaseous atmosphere (mostly hydrogen and helium). Following our Solar System, we can separate the giant planets into two subgroups: the *gas giants*, and the *ice giants*. The gas giants, as Jupiter and Saturn, often called just *jupiters*, have a layer of liquid metallic hydrogen between the core and the atmosphere. They present the smallest density (e.g. $1.3 g/cm^3$ for Jupiter, and $0.69 g/cm^3$ for Saturn), because they are mostly made of gas ($> 90\%$). The ice giants, like Nepture and Uranus, often called just *neptunes*, present a layer of volatile elements below their atmosphere. For this reason, they have a higher density (e.g. $1.27 g/cm^3$ for Uranus, and $1.64 g/cm^3$ for Neptune), and a lower gas fraction ($\sim 20\%$).
In the high variety of the detected exoplanets (see Sect. 1.2.3), we can observe planets with mass between $1.5 M_\oplus$ and $10 M_\oplus$, called *super-earths*. Despite the name, these

planets are not necessarily similar to our Earth, as their definition is only linked to their size. Between the super-earths and the giant planets, we can identify the *ocean planets*, and the *mini-neptunes*. Both are most probably planets formed behind the snow line, that have accumulated a large fraction of volatile elements. The rocky crust has been replaced by a ice water layer, possibly with liquid and gaseous water. When a gas layer is also present, the planets are called mini-neptunes. These last two planet types can be recognized by their lower density with respect to the terrestrial planets, but with similar size.
The light from a planet is composed of the starlight reflected by the planet, and the light emitted by the planet itself. In order to analyse this light, spectroscopy is the privileged technique. The spectrum of a planet is affected by the molecules present in the atmosphere. The giant planets atmosphere is mostly composed of hydrogen and helium. Few other elements are present in significant quantity: carbon (mostly as methane, CH_4, and carbon monoxyde, CO), nitrogen (as molecular nitrogen, N_2, and ammonia, NH_3), and oxygen (mostly in water molecules). The pressure and temperature gradients inside the atmosphere define the altitude of most components: methane, ammonia and water are quite high in the atmosphere, while silicates and metals are closer to the core, where the temperature and pressure are higher. At lower temperature, nitrogen and carbon are mostly present as gaseous ammonia and gaseous methane, while at higher temperature, we can observe principally gaseous nitrogen and gaseous carbon monoxyde. The position and depth of the absoption line of these molecules can be an indication of the effective temperature of the planet: for example, colder planets have a deeper absoption line at $10\mu m$, indication of the presence of gaseous ammonia. Planets with an effective temperature of $\sim 900 - 1000K$ present a deeper absoption line for the methane.

1.2.2.1 Biomarkers

The analysis of the spectrum of an exoplanet, together with its atmosphere, is necessary to determine the presence of life. A *biomarker* is an indication of the presence of biological activity. In particular, a thermodynamic disequilibrium of the components of the atmosphere could indicate the presence of a biosphere. Earth is an example: the gases released by the organisms, O_2, CO_2, CH_4, N_2O, are between the most present components in the atmosphere. The disequilibrium is particularly evident by the simultaneous presence of CH_4 and O_2: the latter should completely dissociate the former.

Figure 1.4 shows the absorption spectrum from Venus, Earth and Mars as observed from space. From the Earth spectrum (see Fig. 1.5), we can observe that the strong absoption of H_2O implies a strong presence of liquid water, the presence of CO_2 points to the presence of an atmosphere, the ozone absorption implies the presence of O_2, and finally the methane CH_4 could have a biological origin.

1.2.2.2 Habitable Zone

The circumstellar habitable zone (CHZ, Kasting et al., 1993) is the region around a star where the conditions are favourable to shelter life. This is mostly linked to the presence of liquid water on the surface: this means that planets outside the CHZ could see the development of life underground, where the conditions for liquid water are reached. The conditions to be inside the habitable zone depend on the mass of the planet, its orbit (distance from the star or the host planet, for the moons), and

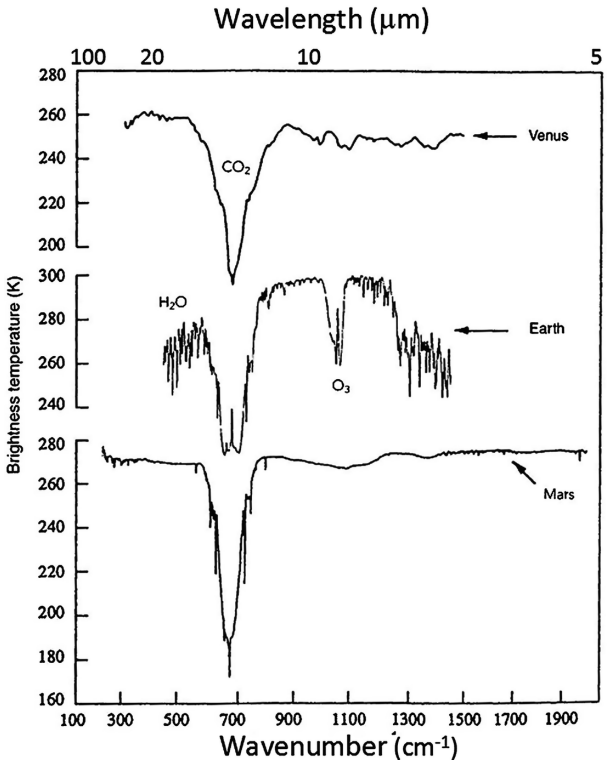

FIGURE 1.4: Absorption spectrum from Venus, Earth and Mars (Hanel et al., 1992).

the radiative flux of the star. Figure 1.6 shows the different habitable zones for two different stars: Gliese 581 (a red dwarf), and the Sun.

1.2.3 Statistics and characteristics of observed exoplanets

About 25 years ago, two major announcements opened the road for a better understanding of our universe: the discovery of a bona-fide brown dwarf companion to a nearby star (Nakajima et al., 1995) and a Jupiter-sized planet around a Sun-like star (Mayor et al., 1995). The first closed the gap between planetary and stellar mass objects; the second opened the road for exoplanetary science as we know it today. The vast diversity in planets that we can see in our solar system cannot be explained by few parameters, a more comprehensive theory has to be elaborated, leaning on a sufficiently large statistical survey.
More than 5000 exoplanets have been confirmed since the first discovery in 1995, another 4000 are yet to be confirmed, for a total of 4000 planetary systems, which result from dozens of surveys. From this number of exoplanets, statistical studies can be performed. It is worth noting that the vast majority of surveys (and so planet discoveries) have been obtained with radial velocity (see Sect. 1.3.1) and transit (see Sect. 1.3.2) detection methods. As explained later, these methods are sensitive to shorter orbit planets, while direct imaging (see Chap. 2) can observe bigger planets at larger distance (see Fig. 1.7). Because of this bias, the most commonly observed exoplanets are Neptune-size planets (34%), followed by gas giants (32%), of which hot Jupiter in sub-0.1 AU are 10% (statistically they represent quite an important fraction of detected exoplanets, because of the ease of the detection; but only 1% of stars have one), Super-Earth (30%), and finally terrestrial planets, which are only 4%.

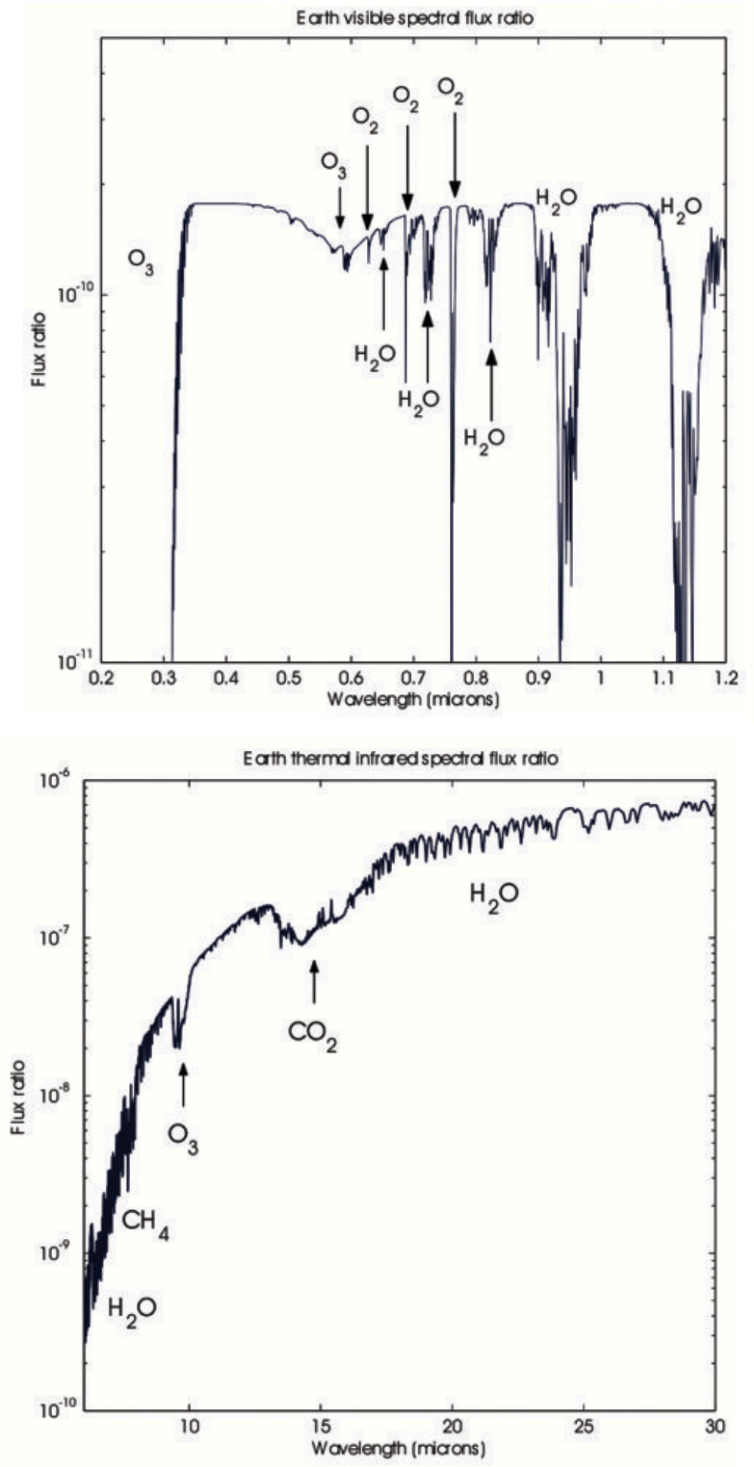

FIGURE 1.5: Absorption spectrum from Earth in the visible and infrared. In the visible, biosignatures like O_2, O_3, and H_2O are visible. In the infrared, the molecules CO_2 and CH_4 are well detected (Pearl et al., 1997).

Using the detected planets, the Eta-Earth Survey at Keck found that 15% of Sun-like stars host one or more planets with $M \sin i = 3 - 30 M_\oplus$ orbiting within 0.25 AU. The HARPS survey (Lovis et al., 2009) extended it to $1 - 3 M_\oplus$ planets, showing that

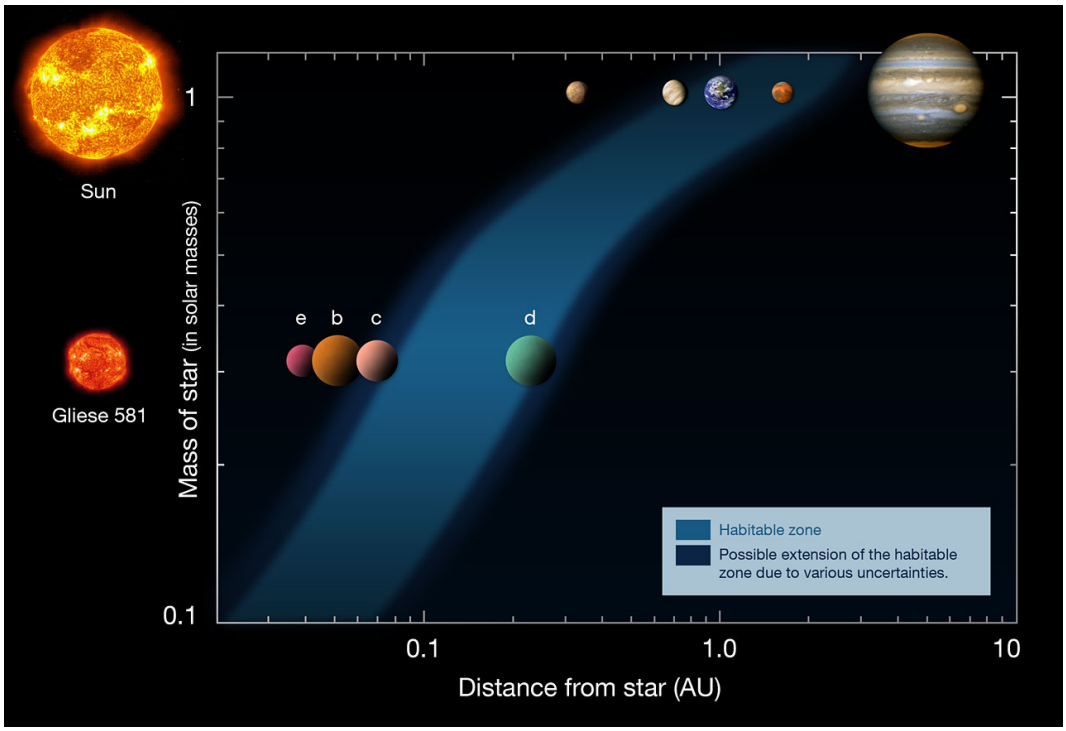

FIGURE 1.6: The definition of habitable zone for two different star systems, the Solar System (upper row), and the Gliese 581 system (a red dwarf, lower row). Based on a diagram by Franck Selsis, Univ. of Bordeaux. Credis: ESO.

low-mass planets have small orbital eccentricities and are commonly found in multi-planet systems with 2-4 small planets with short orbital periods (weeks or months). At least 50% of stars have one or more planets of any mass with periods shorter than 100 days.
The Kepler mission (Howard, 2013) showed that the most common planets are small (up to $2.8M_{\oplus}$, below which the occurance stagnates) with shorter periods (below 50 days). These planets seem to be more common around cool stars. In particular, M dwarfs seem to have 0.9 planets per star with size $0.5-4R_{\oplus}$ and periods below 50 days. 15% of M dwarfs observed by Kepler seem to have Earth-size planets ($0.5-1.4R_{\oplus}$) orbiting the habitable zone. However, with more recent HZ models, this value could be three times higher. Of the Kepler planet host stars, 23% have one or more transiting planets, which likely orbit in the same plane, with mutual inclinations of a few degrees. Fang et al., 2012 found that 54% of systems have at least 1 planet with period below 200 days. This occurance decreases to 27% for 2-planets systems, to 13% for 3-planets systems, 5% for 4-planets systems, and 2% for 5-planets systems. The vast majority (85%) have mutual inclinations of less than 3° (finding also suggested by HARPS). This coplanarity is consistent with the hypothesis of planets forming in a protoplanetary disk without dynamical perturbations.

10.5% of G and K-type dwarf stars host one or more giant planets ($0.3-1M_J$) with orbital periods spanning between 2 and 2000 days and orbital distances between 0.03 and 3 AU (Keck Observatory, around 1000 F, G, and K-type dwarf stars observations). By extrapolation (Cumming et al., 2008), $17-20$% of G and K-type dwarf stars have giant planets orbiting within 20 AU and P= 90 years, which is consistent with microlensing (see Sect. 1.3.3) survey. The giant planet semi-major axis distribution (Wright et al., 2011, see Fig. 1.8) shows that single planet systems have

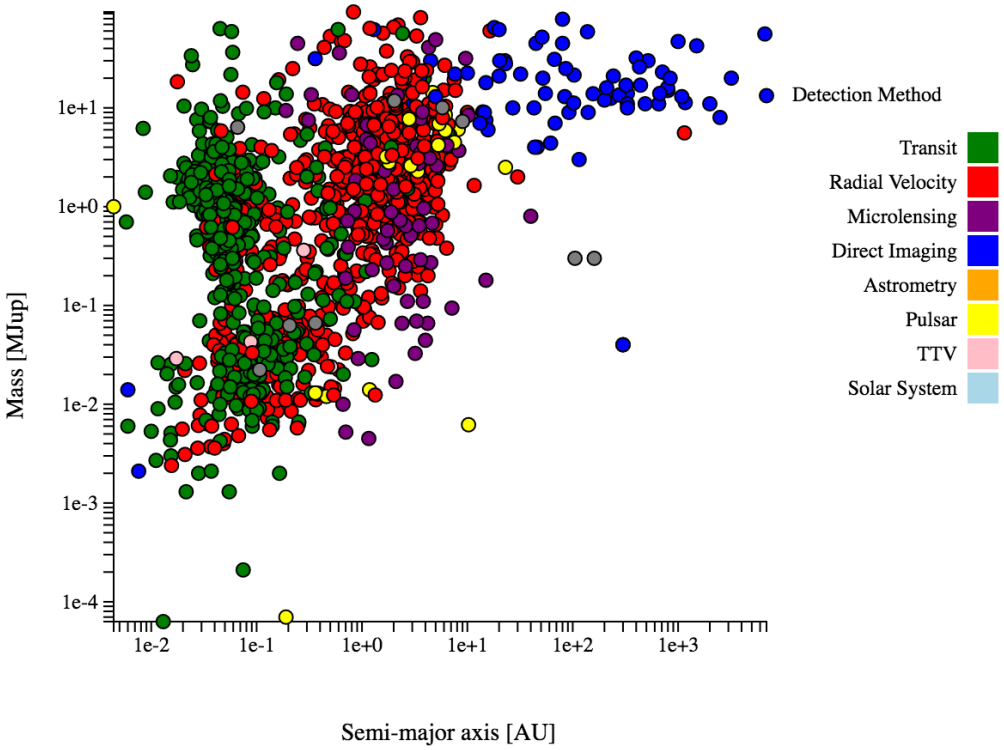

FIGURE 1.7: Masses and orbital distances of planets from the catalog exoplanet.eu of March 2021. Planets in the Solar System are colored in grey. Credits: Lesia

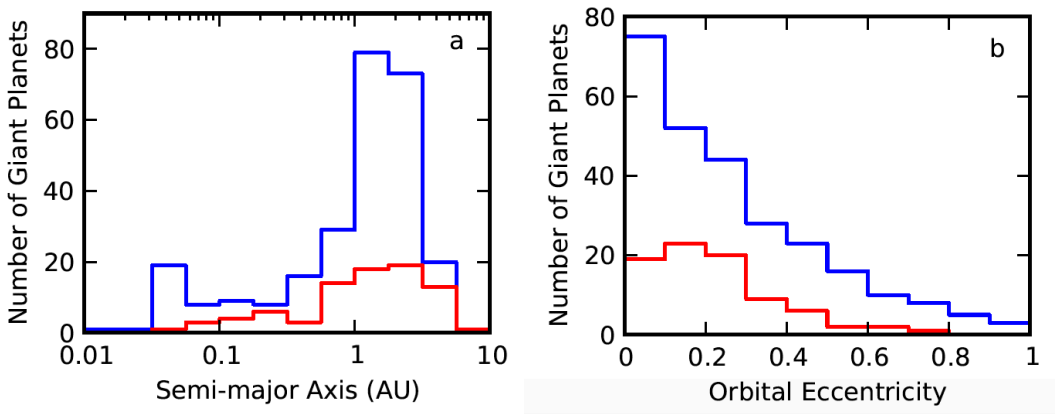

FIGURE 1.8: Orbital characteristics of giants planets: semi-major axis (a), and orbital eccentricity (b). In blue, the occurance for single planet system, in red for multiple planet system (Fischer et al., 2014).

higher occurance for orbits higher than 1 AU and around 0.05 AU. These *hot Jupiters* seem to disappear for multi-planet systems. Metal-rich stars with mass $0.3 - 2M_{\odot}$ are more likely to host giant planets within 5 AU (Fischer et al., 2005, Johnson et al., 2010). Neptune-size planets ($R > 4R_{\oplus}$) prefer metal-rich stars, while smaller planets don't show any preference.

The mass-radius relationships is very difficult to establish, mostly because only few planets have sufficent data to define these two characteristics. For giant planets ($M > 100M_{\oplus}$), the radius varies by a factor 2, while smaller planets ($M = 30M_{\oplus}$)

show higher dispersion (factor 5). This scatter implies a more complex definition of the planets composition. A very emblematic case is *GJ 1214b* ($M = 6.5M_{\oplus}$, $R = 2.7R_{\oplus}$, density of $1.9g/cm^3$, Charbonneau et al., 2009), for which several compositions are possible: a "super-Earth" with rock/iron core and hydrogen atmosphere; a water world with a rock/iron core, a water ocean, and a massive atmosphere; or a mini-Neptune with rock/iron core, water ocean and hydrogen/helium atmosphere.

1.3 Indirect methods

Historically, the first exoplanets have been discovered by indirect methods. The most important advantages of these techniques are, on one side, the high sensitivity to a variety of planets sizes and on the other side, their diversity: several aspects of the star-planet interconnection can be exploited to effectively detect the exoplanet and obtain its characteristics.

1.3.1 Radial Velocity

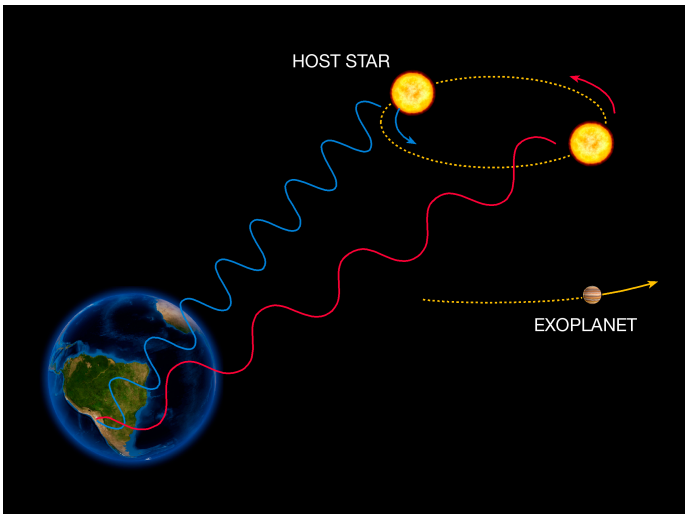

FIGURE 1.9: The radial velocity method to detect exoplanet is based on the detection of variations in the velocity of the central star, due to the changing direction of the gravitational pull from an orbiting exoplanet as it orbits the star. Credits: ESO

The first indirect method to be developed is the radial velocity method, which produced the very first exoplanet ever detected around a Sun-like star, $51Peg$ (Mayor et al., 1995). This detection technique is based on the Doppler effect and the reciprocal attraction between two masses orbiting around each other: the gravitational force of the exoplanet attracts the star, forcing it to orbit around the center of mass of the star-planet system (see Fig. 1.9). This orbit with respect to Earth is seen as a back and forth movement, resulting in a change in the radial velocity of the star. This change affects its spectrum, following the Doppler effect: the spectrum is redshifted when the star moves away from Earth; it is blueshifted when it moves towards Earth. The actual detection comes from the periodical observation of these wavelength shifts (see Fig. 1.10). Because the mass difference between the planet and the star is quite important, the speed of the star is very small: for example, the Sun moves by about $13m/s$ due to Jupiter, but only $9cm/s$ due to Earth. However, modern spectrographs,

as HARPS in La Silla, Chile, and ESPRESSO at the VLT, Chile, are able to detect radial velocity down to few tens of cm/s.

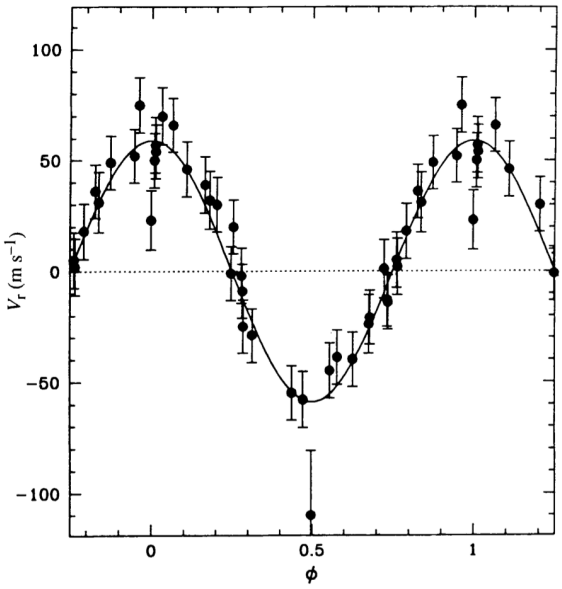

FIGURE 1.10: Radial Velocity curve of 51Peg (Mayor et al., 1995).

The radial velocity method requires high signal-to-noise ratio spectra to achieve high precision, so it is usually used for brighter and late-type main-sequence stars. The reasons behind this is threefold: first, late-type stars are more affected by the gravitational effect of the planets, due to the smaller difference in masses between the two. Secondly, these stars rotate generally slowly, providing clearer spectral-line data. And finally, these stars have generally a larger number of spectral lines when compared to early type stars. Detecting planets around more massive stars is easier if the star has left the main sequence, which has reduced its rotation speed. A complete orbit must be measured by radial velocity to allow a robust description of the orbital period. It is therefore easier to detect close-in planets. The radial velocity method allows a direct measurement of the eccentricity of the planet orbit, while only giving access to a lower limit of the mass (M*sin i). However, for some strongly irradiated giant planets (hot Jupiter) around nearby stars, the planet spectral lines can be separated from those of the host star and enable the measurement of the radial velocity of the planet itself. In this way, on one hand the inclination of the orbit is fixed, and the mass is obtained as a result, and on the other hand the composition of the planet can be established. The future of the radial velocity method must face two important challenges: a technological one and a theoretical one. The technological one lies in the capability of the instrument to have stable measurements wrt temperature, pressure and vibrations together with a stable optical CCD detector. The theoretical challenge is linked to the stellar activity, which can lead to a misinterpretation of spectral lines as Doppler effect due to the presence of a planet. The easier targets for radial velocity are in principle close-in planets (e.g. in the habitable zone) of low-mass stars. However, most of these stars are faint in the optical and peak in the NIR (between 0.8 and 1.8ţm). Infrared instrumentation has different challenges wrt the optical: stable cold operating temperatures of the instrument, and need for NIR detector. NIR spectroscopy is essential to discriminate between giant planets and stellar activity, when observing young active stars. Space based Doppler measurements will ease the detection. On one hand, the PSF is very stable and the image

size quite small, making it easier to have high resolution with a smaller instrument, due to the lack of the Earths atmosphere. On the other hand, the issues created by sky subtraction and telluric contamination would be eliminated.

1.3.2 Transit

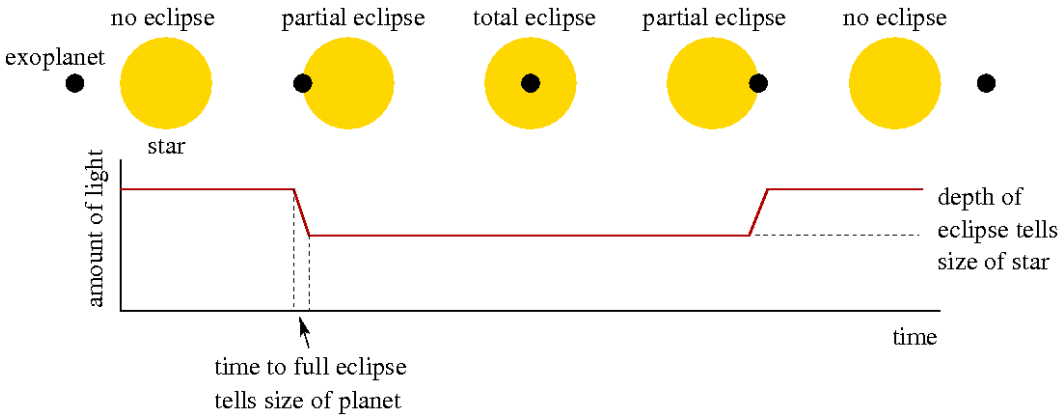

FIGURE 1.11: Light curve for transiting planet: when the exoplanet passes in front of the star and blocks some of its light, the light curve indicates this drop in brightness. Credits: T. Sanders, F. Rasio, S. Chatterjee and F Valsecchi; Northwestern University.

When an exoplanet transits periodically in the line of sight between Earth and its host star, it masks some of the starlight, attenuating its brightness. This decrease in brightness can be detected by telescopes, giving an indication on the presence of the exoplanet. In particular, the attenuation in starlight depends on the relative size of the exoplanet with respect to the star, giving an information on the radius of the exoplanet. Assuming that the stellar disk is uniform, and the orbit is circular, a transit observation can measure certain quantities (see Fig. 1.11): the transit depth, the transit duration, the ingress/egress duration, and the period of the exoplanet. The transit depth describes the decrease in the normalized flux of the star during the transit, giving an indication on the radius of the exoplanet, by comparison with the stellar radius. The transit duration is the time the exoplanets needs to transit the star, giving an indication on the orbital period. The ingress/egress duration is the time needed by the exoplanet to cover (ingress) and uncover (egress) the star. The more the exoplanet transits the star close to the full diameter, the smaller are these durations. By analyzing these elements, it is possible to derive different physical parameters of the star-planet system (star mass, star radius, exoplanet radius, eccentricity, inclination). The transit method prefers smaller orbits, because several transits (needed to confirm the nature of the eclipse) can be observed in a reasonable time.
The main advantages of the transit method are twofold: on one hand, it derives the exoplanet radius and inclination, which, in combination with the radial velocity measurements, gives the actual mass of the planet and so its density; on the other hand, the analysis of the star spectrum during the transit can give an indication of the composition of the atmosphere of the planet (during transit, the exoplanet atmosphere absorbs part of the light from the star). An important result of the density measurement is the definition of the exoplanets nature: a low density will indicate a gaseous planet, a medium density a water planet, and a higher density will direct to a rocky planet. The secondary eclipse (when the planet passes behind the star)

allows in favourable cases a direct measurement of the planet radiation and it helps constrain the planets orbital eccentricity. By subtracting the intensity of the star during the secondary eclipse to the intensity before or after (when both star and planet are measured), the signal of the planet can be isolated, allowing for the measurements of the planet temperature or even signs of clouds.

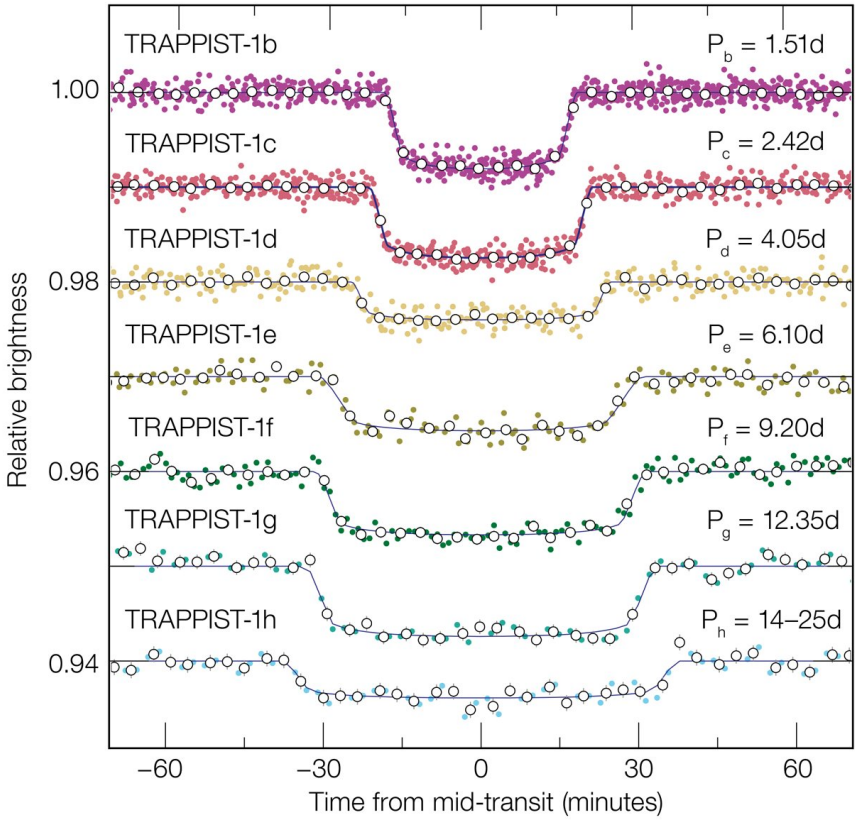

FIGURE 1.12: Transit light curves for the TRAPPIST-1 system (Gillon et al., 2016): the more massive planets have a deeper luminosity attenuation, while the most distant planets have longer transits.

The transit method has two major disadvantages. The first is linked to the actual possibility of observing a transit: in order to measure the decrease in starlight, the planets orbit has to be aligned with the observer's point of view. The probability of such an alignment is about 10% for planets with small (< 0.1AU) orbits, and even lower for larger orbits. A planet orbiting a sun-sized star at 1 AU has a probability of 0.01% to be inclined so as to produce a transit observable from Earth. The second disadvantage is linked to the high rate of false detections. On one side, signals similar to transit can come from different objects in the sky (as blended eclipsing binary system, grazing eclipsing binary systems, planet size stars); on the other, some stars, as red giant branch stars, have pulsations in brightness with similar period as transiting planets. Several missions, ground- and space-based, have been dedicated to transit detections, with Kepler and TESS being the most productive. With around 4000 exoplanets detected, these two missions have given access to an important population statistic, allowing a better comprehension of the planet formation process. On the other side, ground-based missions, as TRAPPIST (see Fig. 1.12), have been able to detect multi-planetary systems around M dwarfs, with sufficiently simple instruments.

1.3.3 Microlensing

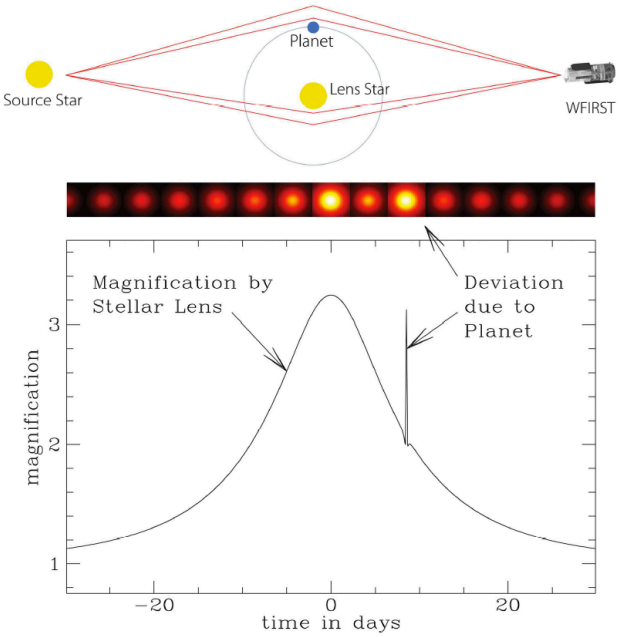

FIGURE 1.13: Gravitational lensing caused by the presence of a star and an exoplanet. Credits: WFIRST/NASA.

Gravitational microlensing occurs when a star acts like a lens, magnifying the light of a distant aligned star. The light from the source star is bent by the lens star, so that the observer sees an amplified, multiple image of the source. If the lensing star has a planet, it can be detected if the source image passes near the position of the planet. This creates a perturbation in the microlensing light curve of the host star (see Fig. 1.13 and 1.14). This method is most useful for stars located towards the galactic center, because of the huge number of stars, which increases the chances of alignment. Its main advantage is the very diverse type of planets it can detect: low-mass planets, wider orbits (comparable to Saturn and Uranus), very distant stars. The microlensing method is more sensitive to planets around 1-10 AU from late-type stars. However, it is easier to detect planets around low-mass stars, because they are much more abundant in the galaxy. The main disadvantage of this method is the rarity of the event: on one side the event can be detected once and never again (since the stars have moved away from the alignment), on the other side the event is very rare, because a perfect alignment is quite difficult to obtain. Furthermore, the only physical characteristics that can be determine is the mass of the planet relative to the stellar mass (which is usually not well known), while the semi-major axis could be wrongfully determined for a very eccentric or inclined orbit. Several ground-based observing programs have been dedicated to the microlensing method, such as OGLE (Udalski et al., 1992).

1.3.4 Astrometry

The astrometry method corresponds to the measurement of a star's position relative to the background sky: an astrometric orbit corresponds to the barycentric motion of a star caused by an invisible companion (see Fig. 1.15). If a star has a planet, its gravitational influence will cause the star to move in a tiny orbit (circular or elliptical).

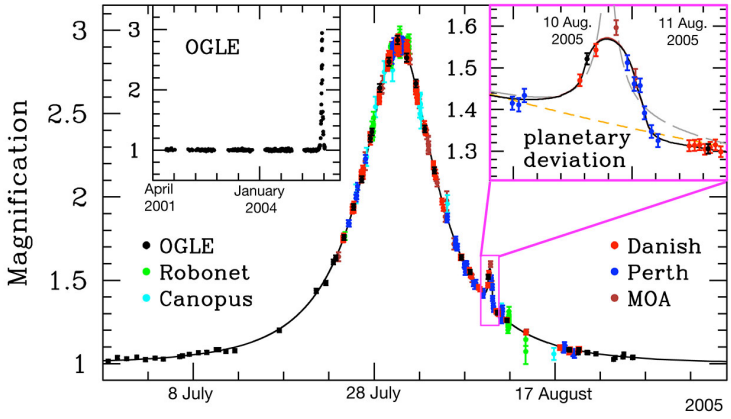

FIGURE 1.14: Light curve for OGLE-2005-BLG-390, showing the planetary deviation, lasting about a day. Each point represents the brightness in a single image and the data are colour-coded in order to indicate the telescope. Credits: ESO.

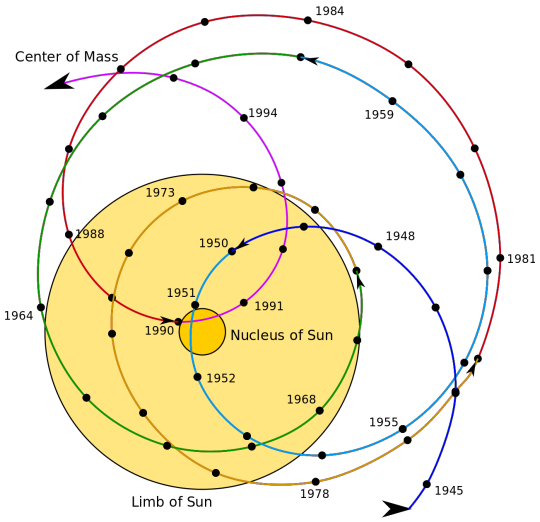

FIGURE 1.15: Solar System Barycentre orbit around Sun. Credits: C. Smith.

The star and the planet each orbit around their mutual center of mass (barycenter). The star being much more massive than its companion, this barycenter lies normally within the radius of the larger body. This method is more sensitive to wider orbits, because the center of mass displacement amplitude increases with orbital period. As a result, detectable orbital periods are typically several years. Because this method measures the photocenter, it is sensitive to the detection of planets around fast rotating stars with broad spectral lines or around very faint objects like brown dwarfs. The need for measurement stability and precision over such long time baselines has been a challenging requirement for currently available instruments. Even though the impact of astrometry on exoplanet detection has been limited so far, it has enormous potential and is complementary to other techniques. Since this technique determines the value of $m_2^3/(m_1 + m_2)^2$, with m_1 and m_2 being respectively the mass of the star and its companion, by knowing the stellar mass, the mass of the companion is determined, without the sin i ambiguity of the radial velocity. An astrometric study of statistical samples of exoplanets could therefore accurately determine the planet

mass function and help to refine theories of planet formation.
The achievable astrometric precision improves with the aperture size. The most successful application of astrometry in the exoplanet detection is in combination with radial velocity. The RV can constrain five out of seven parameters, while the astrometry can determine the other two.
For observations from the ground, the turbulence in the Earth's atmosphere above the telescope is the dominant source of error. It can be mitigated by modeling of seeing-limited observations, by the use of adaptive optics (for instance for a planet search targeting binaries with separations of few arcseconds), and with off-axis fringe tracking in dual-field interferometry. Accuracies better than 0.1*mas* have been achieved, which satisfies the performance improvement necessary for efficient planet detection (see Fig. 1.16).
Space-borne instruments avoid atmospheric perturbations and give access to nearly diffraction-limited observations, thus are ideal for high-precision astrometric work. Space astrometry has started with the Hipparcos mission (1989-1992) and resulted in the determination of positions, proper motions, and absolute parallaxes at 1*mas* level for 120,000 stars. The next space astrometric mission capable of detecting exoplanets is Gaia, launched in 2013.

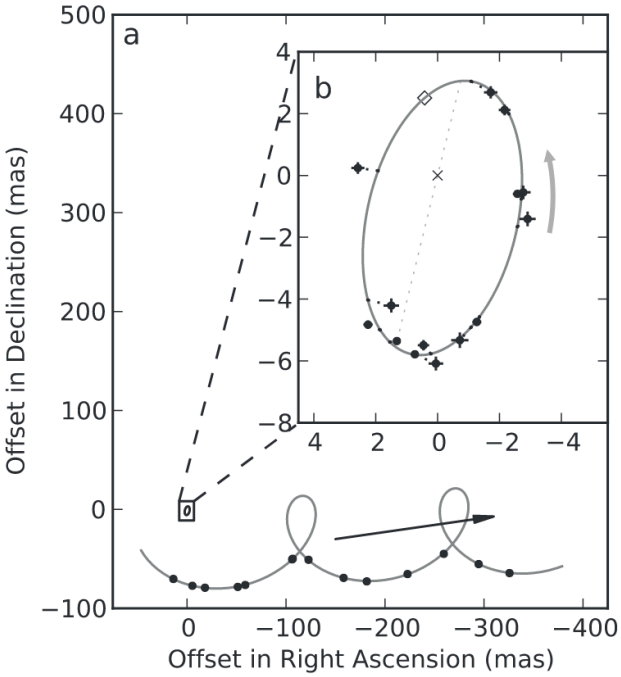

FIGURE 1.16: The barycentric orbit of the L1.5 dwarf DENISP J082303.1-491201 caused by a 28 Jupiter mass companion in a 246 day orbit discovered through ground-based astrometry with an optical camera on an 8 m telescope (Sahlmann et al., 2013).

1.3.5 Results and limitations

Indirect methods have been very prolific over the years, both from ground and space-based telescopes, with large-scale surveys detecting hundreds of exoplanets. As shown in Fig. 1.1, starting in 2014, the number of detected exoplanets has exploded, principally due to the Kepler telescope.
The first space-based telescope to be used for exoplanet detection is the Hubble

Space Telescope, in orbit for more than 30 years. Even though it was not designed to detect exoplanets, the HST has been extensively used over the years, in particular using the transit technique. Lately, HST has observed the TRAPPIST-1 system, via spectroscopy, revealing that at least the first five inner planets do not have hydrogen-rich atmospheres similar to Neptune, but possibly an atmosphere rich in heavier gases like carbon dioxide, methane, and oxygen (de Wit et al., 2018), or no atmosphere at all.

After the first detection of an exoplanet, the interest concerning this branch of astronomy has increased, leading to several new ground and space-based telescopes. In this last category, at least four telescopes have given major improvements: CoRoT, KEPLER, TESS, and GAIA. The CoRoT (in French, *Convection, Rotation et Transits planétaires*, Auvergne et al., 2009) telescope is the first space telescope designed for exoplanets detection, in particular rocky planets, exploiting the transit technique. During its almost 8 years mission, the telescope has detected more than 600 candidate exoplanets, a lot of them still in the confirmation process. The telescope has detected the first Earth-like planet: *CoRoT-7b* (Léger et al., 2009). Orbiting CoRoT-7, at about 150 pc, this rocky planet has a diameter of 1.58 times the one of the Earth, probably with a mass around $8M_{\oplus}$, and a very short orbital period (20 hours). Thanks to its design, the CoRoT telescope could cover a large range of masses, between 0.01 and $100M_J$. From the mission results, it seems that massive planets are more probable around massive stars.

The Kepler telescope (Borucki et al., 2010) was launched in 2009, and retired in 2018. Up to now (May 2022), it is the most successful exoplanet detection space mission, with 5011 exoplanet candidates and 2662 confirmed exoplanets, via transit technique. The first rocky planet detected by the telescope is *Kepler-10b*, a lava world orbiting very close to its star. The first planet, orbiting a double-star system was detected in 2011, *Kepler-16b* (a gas giant). In the same year, Kepler discovered the first planet orbiting the habitable zone of a Sun-like star: *Kepler-22b*, a super-Earth with a diameter twice that of the Earth (see Fig. 1.17). *Kepler-186f* is the first Earth-sized planet detected in the habitable zone of its star, a red-dwarf about 180pc from Earth (see Fig. 1.17). *Kepler-452b* is a super-Earth ($5M_{\oplus}$, $1.5R_{\oplus}$), orbiting a sun-like star, at about $1.04AU$, in the habitable zone of the star. From its characteristics, the planet should be a rocky planet, but its habitability is still unknown. Receiving 10% more energy than Earth, it is possible that it is subjected to a runaway greenhouse effect similar to that seen on Venus.

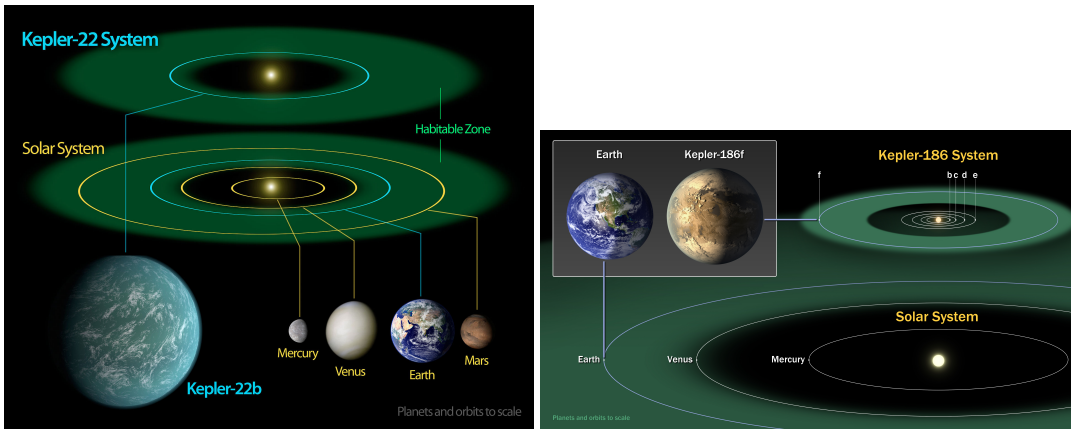

FIGURE 1.17: An artistic concept of the Kepler-22 (left), and Kepler-186 (right) system. Credits: NASA Ames/SETI Institute/JPL-Caltech.

The Kepler mission has demonstrated that there are a lot of multi-planetary systems, with a considerable diversity in planet types (see Sect. 1.2.3).
The successor of Kepler, TESS (Transiting Exoplanet Survey Satellite), and the successor of Hipparcos, GAIA (Global Astrometric Interferometer for Astrophysics) are currently in orbit. TESS, launched in 2018, exploits the transit technique to detect exoplanets in an area 400 times larger than Kepler. It observes brighter (30 to 100 times) stars than Kepler, in particular G- and K-type stars. These targets will be studied in more details by more powerful instruments, as the James Webb Space Telescope (JWST). Up to now (May 2022), the telescope has detected 5725 candidate exoplanets, and 217 confimed exoplanets. The first earth-sized planet was discovered in 2019: *HD 21749 c* is likely a rocky planet, orbiting a K-type main sequence star, with a diameter slightly smaller than the Earth and orbital period of about 8 days. GAIA has been launched in 2013 and it is expected to continue its mission until 2025. Exploiting astrometry, and radial velocity measurements, it determines the true mass of candidate exoplanets, by measuring orbits and inclinations. By coupling Hipparcos and Gaia data, scientists have been able to confirm several planets. From the second Gaia data release, Michel et al., 2021 have analysed 289 targets, all within 500pc from the Sun, and have detected exoplanets around 41 binary, and 5 triple star systems.
These indirect methods have proven to be very successful in detecting exoplanets, but they can only provide limited information about the planets themselves. For example, the radial velocity methods can only provide a lower limit to the mass, because of the unknown inclination angle of the orbit. Transit can provide the planet's radius and possibly its spectrum, but with numerous observations and a bit of luck, because the orbit of the planet has to be aligned with the observer. A great disadvantage of indirect methods is the bias they can create in planet statistics: mostly old, quiet, and solar mass (G-K) stars are being studied, and planets closer to their stars (few AU) with small orbital periods are privileged.
Direct detection methods can increase the statistics of the detected planets, and so ameliorate our knowledge of planet variety, formation, and evolution.

Chapter 2

High Contrast Imaging

Indirect methods have delivered more than 5000 confimed exoplanets over the years, but formation and evolution models require a step forward. These techniques privilege old, quiet stars and planets closer to their parent star. This leaves a full range of planets aside: larger separation, younger and hotter planets. Direct techniques can be used to complement indirect methods: because of the challenges they face (brightness difference between star and planet is high, while the angular separation is quite small), they have focused their attention on hotter planets with larger orbits. The complementarity of these techniques has improved our knowledge of exoplanets formation and evolution. Despite the small number of exoplanets detected up to now (less than 100), direct methods have seen an increased interest, because of the significant improvement in the exoplanetary science field they can provide. For this reason, most of the latest ground- and space-based telescopes have been built to exploit direct detection techniques, as the James Webb Space Telescope, and the Extremely Large Telescope.

The direct detection technique has firstly delivered images of sub-stellar objects, such as the first brown dwarf discovered in 1995, G1 229B (Nakajima et al., 1995). Ten years later, the first planetary companion was detected around the brown dwarf 2M 1207, with a mass of $\sim 5M_J$ and a separation of $\sim 55AU$ (Chauvin et al., 2004). This technique is based on a *direct* image of the planet, by detecting the light coming from the planet (reflected or emitted by the planet itself), and not the effect of the companion on the star, as for indirect methods (see Sect. 1.3). The great challenge is to spatially resolve the planet from its host star. This is essentially due to three problems:

- the difference in brightness between the star and its exoplanet is very high, with images' contrast varying from 10^{-3} to 10^{-10}
- the angular separation between them is very small
- the Earth's atmosphere and/or the imperfect optics and instrument create a distorted wavefront

Theoretically, the image of a point source, as a star, through a telescope is a diffraction pattern, known as the Airy-pattern in case of a circular aperture (as in most telescopes). Its size is directly proportional to the observation wavelength, and inversely proportional to the diameter of the primary mirror. The consequence is that, by increasing the diameter of the telescope, both the angular resolution and the collecting area (and so the sensitivity to fainter stars) are increased. Unfortunately, for ground-based telescopes (for which bigger primary mirrors are easier to built with respect to space-based telescopes), the Earth's atmosphere distorts the wavefront, creating a fuzzy blob, and limiting the angular resolution.

High angular resolution and high dynamic range can be obtained by a combination of hardware (*Coronagraphy*, *Adaptive Optics*, see Sect. 2.1, and 2.2) and software (*Observing techniques*, *Post-processing techniques*, see Sect. 2.3, and 2.3) techniques.

2.1 Coronagraphy

A first hardware method to enhance the contrast difference between the star's and its exoplanet's images is to suppress the light of the star without blocking the one from the exoplanet. This is of course even more complicated when the angular separation between the two is very small. The first coronagraph was designed by Lyot to detect the corona of the Sun by putting an opaque mask at the focal plane of the telescope that blocked the light of the Sun and a pupil stop in a downstream pupil plane (usually called Lyot stop). Its name has now been used to indicate any device that allow the suppression of the on-axis starlight from the star, while permitting the off-axis light of the companion to pass through the optical system.
Coronagraphs can be catalogued into four basic categories, depending on which part of the light they affect (amplitude or phase) and in which plane they are positioned in the optical train (pupil or focal plane). Beyond these four categories, hybrid versions are now very common and very promising.
Amplitude coronagraphs are devices that modify/suppress directly the light of the source (as the Lyot coronagraph for the corona of the Sun). *Phase* coronagraphs induce spatially distributed phase shifts, that redistribute the light in a downstream pupil or focal plane (where it can eventually be stopped). *Pupil* plane coronagraphs are normally composed of one filter that modifies the starlight distribution in a downstream focal plane. *Focal* plane coronagraphs are composed of at least two filtering devices, one in the focal plane and one in the exit pupil plane.

2.1.1 Focal Plane Amplitude Coronagraph

A focal plane amplitude coronagraph consists of a focal plane and a pupil plane amplitude mask.

The *classical Lyot coronagraph* (Lyot, 1939, Sivaramakrishnan et al., 2001) blocks the on-axis source with a focal plane mask, followed by a pupil-plane Lyot mask that blocks a large fraction of the Airy rings not blocked by the focal plane mask. However, this device cannot completely stop the starlight and the finite size of the focal-plane mask prevents from observing regions close to the star. A solution to improve the light extinction is to use apodization (with a prolate function) at the entrance pupil (Soummer et al., 2003).

2.1.2 Focal Plane Phase Coronagraph

A *focal plane phase coronagraph* consists of a focal plane phase mask and an amplitude pupil mask. The first focal plane mask is generally fully transparent (to affect only the phase of the starlight) and it generates phase shifts that reject, by destructive interferences, the light of the star out of the area of interest. This light is then blocked by an opaque amplitude mask at the exit pupil plane, referred to as "Lyot stop".

The *Roddier mask* (Roddier et al., 1997, see Fig. 2.1) is created by introducing a phase step in the mask, with a well-chosen diameter. This step produces a phase shift: it shifts a fraction of the light by half a wave to create destructive interferences in the downstream pupil. However, the phase step is strongly dependent on the index of the material and the wavelength. The diameter of the mask is also dependent

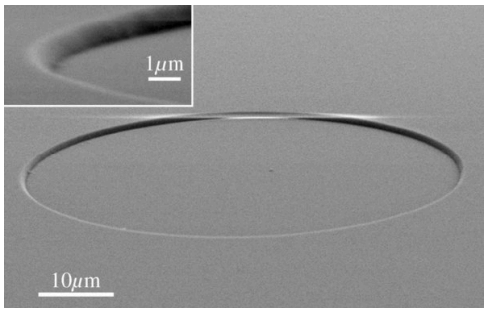

FIGURE 2.1: Scanning electron microscope image of the Roddier phase mask (N'diaye et al., 2010).

on the wavelength (geometric chromatism).
The chromatism of the mask can be reduced by creating several steps. However, the technical difficulty of such devices is of course increased. In order to solve the geometric chromatism of the Roddier mask, the mask can be divided into four symmetrical parts, two of them inducing a π shift to the starlight (see Fig. 2.2, Rouan et al., 2007), creating a *Four Quadrant Phase Mask*.
When perfectly aligned with the center of the four quadrants, the light from the star is rejected outside of the geometric image of the telescope pupil in a downstream pupil plane, where it is blocked by an opaque amplitude mask (the Lyot stop). The planet signal passes through the mask almost intact, especially if sufficiently far from the center of the mask, and from any quadrant edge. This mask is still chromatic with respect to the phase shift (the depth of the mask strongly depends on the wavelength, if the mask is implemented through a single substrate thickness). It is also sensitive to central obscuration and spider arms, and the perfect alignment (both optical-star vs center of the mask-, and fabrication-the four quadrants) is hard to achieve.

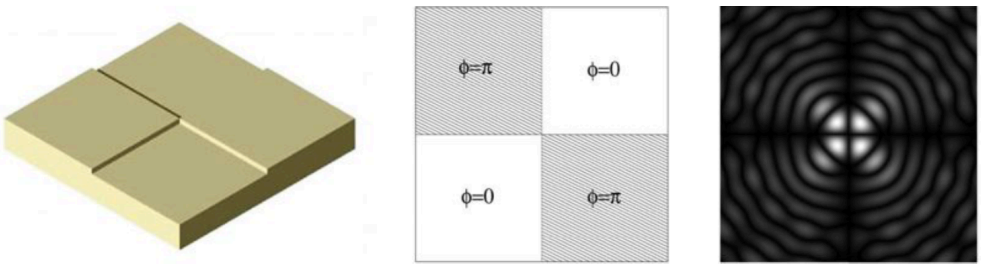

FIGURE 2.2: *Left* Design of the four quadrant phase mask (FQPM). *Middle* Two quadrants on one diagonal make the light undergo a π-phase shift, whereas the two other quadrants let it pass without shifting the phase. *Right* Resulting PSF.

The *Vortex Coronagraph* (VC) (Mawet et al., 2005a, Foo et al., 2005) produces a continuous helical phase ramp, with a singularity at the center, which creates an optical vortex and hence nulls the light locally. A more detailed description is presented in Chap. 3.

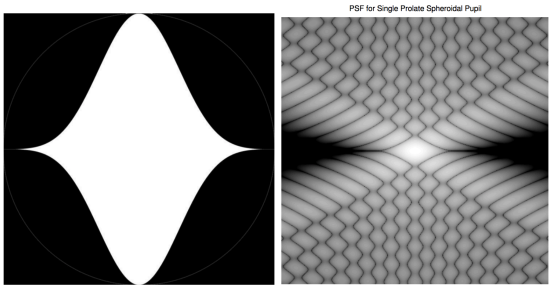

FIGURE 2.3: *Left* Design of the single Spergel-Kasdin prolate-spheroidal mask. *Right* Resulting PSF. (Kasdin et al., 2004)

2.1.3 Pupil Plane Amplitude Coronagraph

A pupil plane amplitude coronagraph is composed of one amplitude mask at the pupil plane that generally aims to create a dark hole in a downstream image plane. In order to increase the search area, specific designs have been introduced. *Shaped pupil coronagraphs* (Kasdin et al., 2004) are apodized pupils, optimized for high-contrast imaging, which create a dark hole, by shaping the point spread function. The optimization is usually performed by maximizing the throughput, with constrains on contrast and inner working angle. These masks feature a binary amplitude apodization, easing the manufacture with respect to smooth apodizers, where the transmission should smoothly vary in amplitude to the required accuracy. Fig. 2.3 shows the design of a single Spergel-Kasdin prolate-spheroidal mask, with a throughput of 43% and an inner working angle of 4 λ/D. However, the dark zone is quite narrow, requiring many rotations for complete discovery.

2.1.4 Pupil Plane Phase Coronagraph

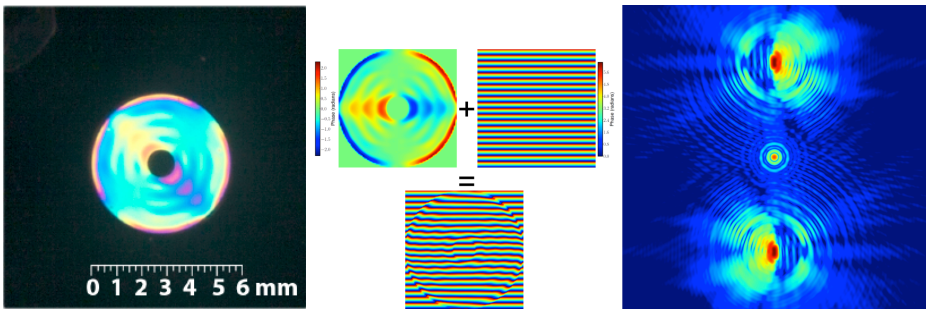

FIGURE 2.4: *Left*: The vAPP is obtained by superimposing three layers of liquid crystal. *Center*: The vAPP phase pattern. *Right*: The vAPP final image, with the characteristic three PSFs: two coronagraphic ones with 180° suppression zone and one leakage term between them (M. Kenworthy, pers. comm.).

A pupil plane phase coronagraph is an optical device that modulates the phase of the incoming light at the pupil plane.

The *Apodizing Phase Plate* (Kenworthy et al., 2007) is a pupil plane phase coronagraph, consisting of an anti-symmetric phase pattern, that redistributes the light in the image plane, creating a dark hole of 180° clear space. The phase pattern responsible for the locally improved contrast can be produced by modifying the

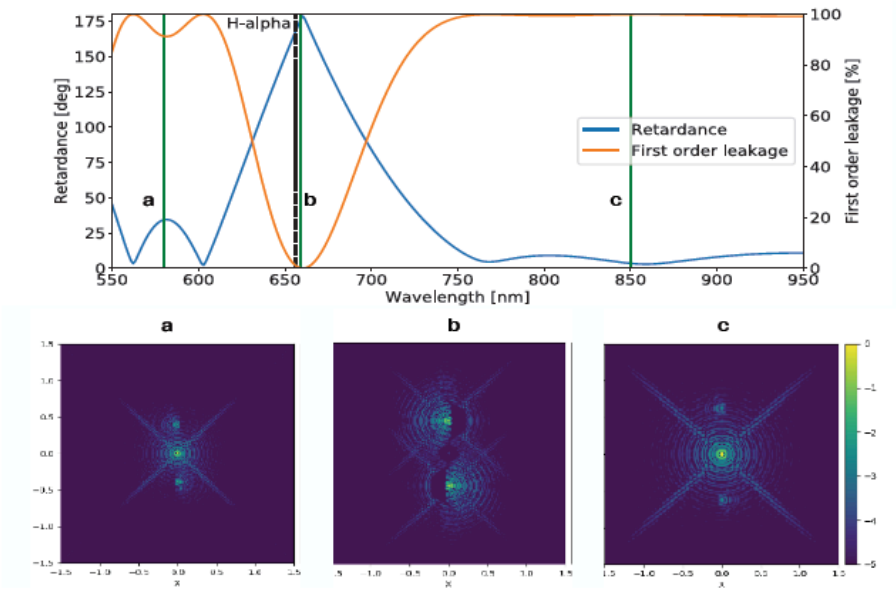

FIGURE 2.5: *Top*: Simulated wavelength selective gvAPP (Doelman et al., 2017): the blue line is the retardance and the orange line is the leakage term. In this simulation, the gvAPP has been optimised to have a 180° retardance in a 10nm band around *Hα* (656.28nm) and 0 elsewhere. *Bottom*: The corresponding gvAPP PSFs for the three wavelengths defined on the top figure (green lines). Around the optimised wavelength, the coronagraphic PSF is very clear, while for the other two the leakage term is dominant. (Hornburg et al., 2014, Doelman et al., 2017)

thickness of a high refractive index material. However, this configuration is very chromatic (the thickness is proportional to the wavelength). In order to make it achromatic, the phase pattern is better created by a birefringent medium, through vectorial phase, imposed by half-wave retarders (for which the fast axis orientation is variable). These half-wave plates can be produced by self-aligning multi-twist liquid crystal retarder (see Fig. 2.4, left), by piling multiple layers in which the desired pattern is inscribed. The effect of the half-wave retarder on the polarization states is to flip them: left-handed circular polarization state becomes right and viceversa. The induced phase is then equal to twice the axis orientation, but with opposite sign: $\phi_R = -\phi_L$. Since the phase pattern is antisymmetric, the vector phase is also antisymmetric and so are the two PSFs (from the two polarization states). This has an important consequence from an exoplanet detection point of view: the left- and right-handed circular polarization PSFs are complementary, because they clear out opposite side in the image plane, allowing to have a complete 360° coverage space by combining them. However, for unpolarized light, the two PSFs have to be spatially separated on the detector: a quarter-wave plate and a Wollaston prism can be used. This configuration, called *vector APP* (vAPP) is rather complex and it presents a leakage term due to the non perfect retardance of the phase pattern. The solution is to use polarization grating directly on the APP, *grating-vector APP* (gvAPP), to ensure the circular polarization splitting (see Fig. 2.5). The polarization grating is a phase ramp in geometric phase that applies opposite tilts to the two PSFs, while the leakage term is passed undisturbed. The result is an image with 3 PSFs (see Fig. 2.4, right): two contain a dark hole of 180°, in this example between 2 and $7\lambda/D$, the third

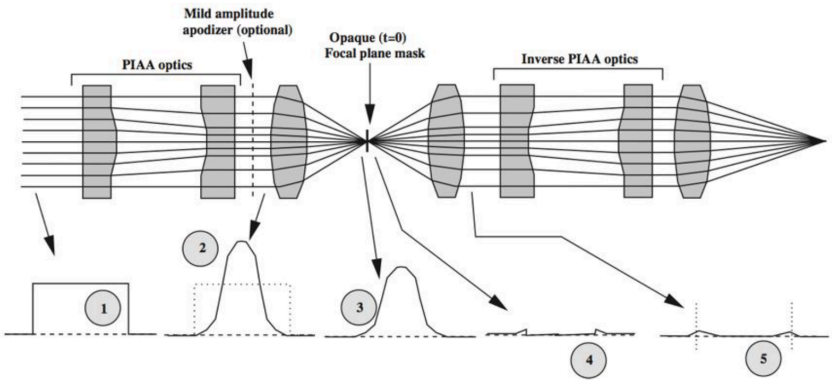

FIGURE 2.6: Architecture of the phase-induced amplitude apodization coronagraph (PIAAC, Guyon et al., 2010).

one is a "leakage term PSF", located between the other two. The two coronagraphic PSFs can be combined to obtain a 360° clear discovery space, while the leakage term can be used as photometric and astrometric reference.
Being a pupil plane coronagraph, the gvAPP can be optimised for complex pupils, with central obstruction and secondary support structures. It is insensitive to tip-tilt errors and, thanks to the liquid crystal technology, extreme patterns can be written from UV to mid-IR, with high-contrast performance and a small IWA. The final encircled energy of the gvAPP is typically around $50 - 60\%$ (although it depends on the chosen geometry of the dark hole), divided into 50% for each coronagraphic PSF.

The *Phase-Induced amplitude Apodization Coronagraph* (Guyon, 2005, Guyon et al., 2010) uses complex aspheric mirrors to apodize the wavefront for high contrast imaging. The light is reshaped into an apodized beam with no loss in throughput or angular resolution. At the back of the coronagraph, a set of inverse optics are necessary to cancel field aberrations, created by the first set of optics, and enlarge the field of view of the coronagraph (see Fig. 2.6).
This technique is promising because of the high throughput, the small inner working angle (IWA, $2\lambda/D$ for a 10^{-10} contrast), the full 360° discovery space and its very low chromaticity, obtained with reflective optics. However, the aspheric mirrors are difficult to manufacture, and the limited number of frequencies that can be optimized during fabrication can damage the apodisation.

2.2 Adaptive Optics

In a perfect case, without aberrations, the image of a point source through a telescope is a diffraction pattern (called Point Spread Function, PSF). The half-width of this PSF represents the smallest angular distance that can be resolved between two sources. Also called Resolving Power, it corresponds to $1.22\lambda/D$, where λ is the observing wavelength and D is the telescope diameter. For larger telescopes, this angular distance decreases, allowing to observe sources closer to the star.

However, in a long exposure, the Earth's atmosphere turbulence makes this point a fuzzy blob (see Fig. 2.7, right); and in a short exposure, the atmosphere creates speckles (see Fig. 2.7, left), which mimic the signal of an exoplanet. These speckles can also derive from imperfect optics. Adaptive optics is a technique used to correct the blurring and motion of the PSF, created by the atmosphere (see Fig. 2.8). It is

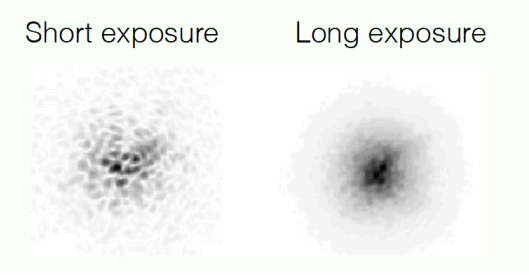

FIGURE 2.7: Short vs long exposure observation of a point source.

a closed loop system: first, the optical distortions produced by the turbulence are measured, with a wavefront sensor, typically one thousand times per second, using a bright source (usually a star). The information is then used to determine the shape of the deformable mirror (DM) to compensate for this atmospheric effect, through thousands of actuators. The number of actuators is linked to the frequencies of aberrations the DM is capable to correct.

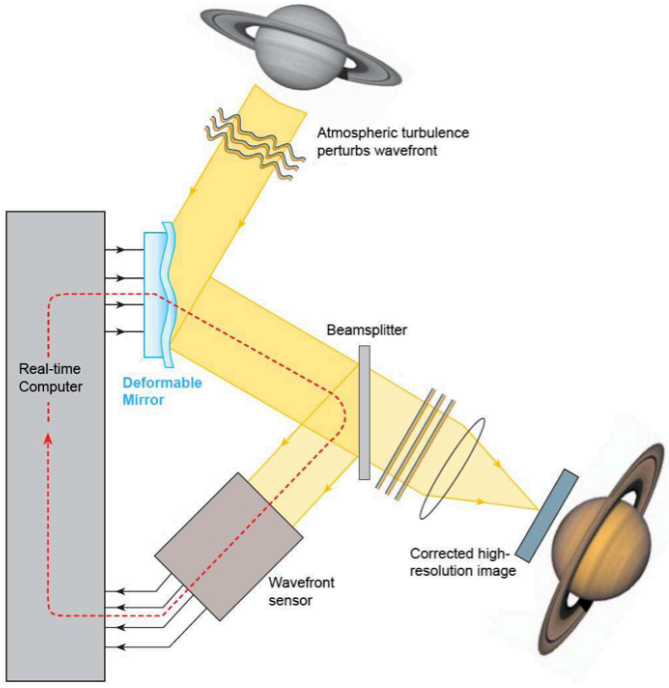

FIGURE 2.8: Adaptive optics working principle (Davies et al., 2012, Credits: S. Hippler).

A useful measure of the capabilities of the AO is the *Strehl ratio*: it is defined as the ratio between the intensity peak of the aberrated image and the maximum intensity of an "ideal" image, where "ideal" means that the optical system is only limited by the diffraction associated with the system's aperture. It measures the quality of the image: varying from 0 to 1, a perfectly unaberrated optical system will have a Strehl ratio of 1.
AO systems have seen a huge development over the last decades. One of the first system specifically designed for high-contrast imaging is the PALM-3000 for the 5-m telescope at Palomar Observatory (Dekany et al., 2011). With its 3000 actuators, the system can reach a K-band Strehl ratio as high as 84% in 1.0 arcsecond visible

seeing (Roberts et al., 2012). In the last decade, three new systems have had their first light: GPI at Gemini South (Gemini Planet Finder, Macintosh et al., 2014), SCExAO at Subaru (Subaru Coronagraphic Extreme Adaptive Optics, Jovanovic et al., 2015) and SPHERE at the VLT (Spectro-Polarimetric High-contrast Exoplanet Research, Beuzit et al., 2019).

2.3 Observing Techniques

Unfortunately, hardware techniques are not sufficient to completely remove the speckles during observations. In order to disentangle the signal of a possible companion from these speckles, specific observing techniques are necessary. These techniques are implemented at the instrument level, focusing on how the images are obtained.

2.3.1 Angular Differential Imaging (ADI)

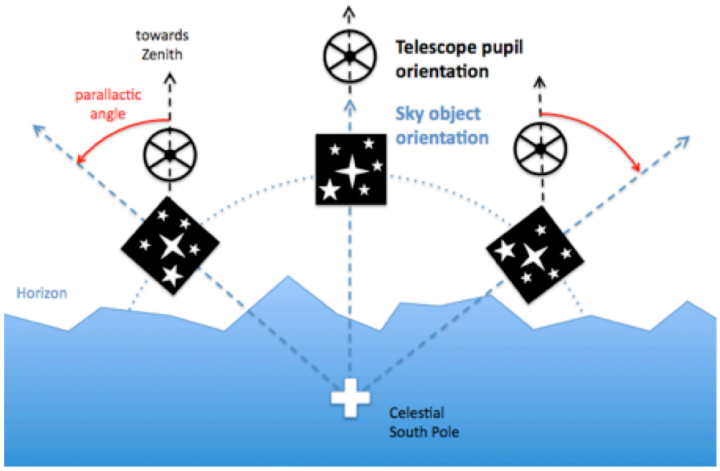

FIGURE 2.9: Angular Differential Imaging technique. Credit: C. Thalmann

In the angular differential imaging (ADI, Marois et al., 2006) observing strategy, the telescope pupil is kept fixed with respect to the detector (pupil-stabilized mode) and the images rotate with time, while the diffraction pattern and the quasi-static speckles remain at a fixed position (see Fig. 2.9). The result is that off-axis companions rotate around the star with a circular trajectory (see Fig. 2.11), as a function of the parallacting angle. This diversity can be used to disentangle astrophysical sources from the speckles.
This technique is widely used in high-contrast imaging, because of its versatility (it works with almost every type of companions). However, it presents some disadvantages: on one side the speckles evolve with time; on the other side, the companion should have a sufficiently large parallactic angle variation in order to move by more than $1\lambda/D$ in the field, and enable detection.

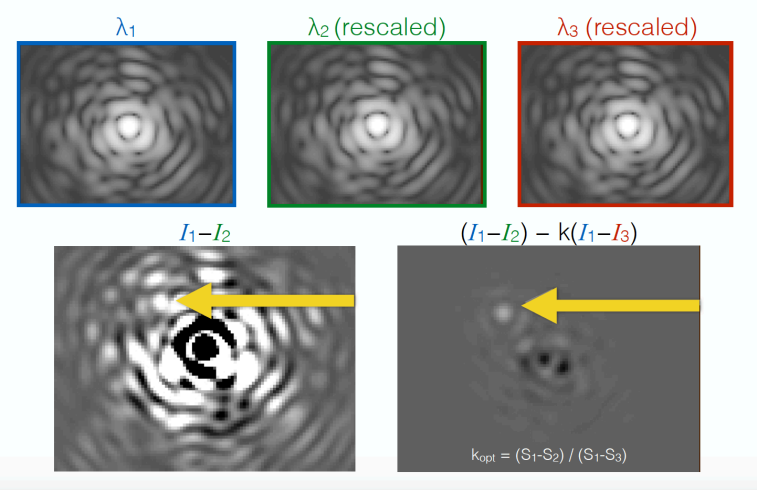

FIGURE 2.10: Spectral Differential Imaging technique. (Marois et al., 2000)

2.3.2 Spectral Differential Imaging (SDI)

The spectral differential imaging (SDI, Smith, 1987, Marois et al., 2000) technique exploits the different wavelength dependence of the speckles and the exoplanet. The images are obtained at two different wavelengths: one inside an absorption band for the planet, and one outside (where the planet is bright). Since the speckle pattern is theoretically identical after rescaling the images with respect to the wavelength, the exoplanet is preserved, after subtraction of the rescaled images(see Fig. 2.10).
Multi-channel SDI (mSDI), or Spectroscopic SDI (SSDI), is an evolution of SDI: in this case, multi-channel images are recorded. The speckle pattern scales with the wavelength (the pattern moves radially out from the center of the image), while the exoplanet stays fixed. By comparing the images at different wavelengths, the exoplanet can be detected. With this technique, the planet does not need a specific feature in the spectrum to be detected.

2.3.3 Reference-star Differential Imaging (RDI)

In the reference star differential imaging (RDI, Lafrenière et al., 2009) technique, a reference star, similar to the science target star, is observed. The two PSFs, reference and science target, are then subtracted, after rescaling of the reference star flux to the target flux. While the resulting images are less prone to systematic biases than in ADI and SDI, and provide a larger discovering space (especially at small separations), this technique presents three strong drawbacks: the first concerns the reference star, which should have the same magnitude, color, and position as the science target star. The second is linked to the PSF rescaling of the reference star: it is essential to obtain the right flux, without creating artifacts. The third problem is linked to the speckles of the atmosphere and the telescope: between the observations on the reference and the target star, the atmospheric conditions and aberrations due to the telescope can change, which can make the subtraction more difficult. Furthermore, the time spent observing the reference star is lost, since no planetary photon is collected during this time.

2.3.4 Polarimetric Differential Imaging (PDI)

The polarimetric differential imaging (PDI, Kuhn et al., 2001) technique exploits the partial polarisation of the reflected light of the planet, with respect to the unpolarized light of the star. If on one side the speckle subtraction is very good, on the other side, this technique requires specific hardware, not always present in all telescopes. Moreover, it presents a low sensitivity due to low level of partial polarization.

2.4 Post-processing

The post-processing techniques intervene after the observations are performed: these methods allow to further decrease the speckles pattern and increase the companion signal, by creating and subtracting the best possible reference PSF. Depending on the observing technique, the PSF subtraction is different.

2.4.1 Median subtraction

A first simple method is the **median** subtraction (Marois et al., 2006): in the ADI observing technique, the planet rotation in the frames will prevent it from appearing in the median image. The median image of the observations can then be used as a first approximation of the starlight and speckles pattern, which is subtracted from each individual frame. The cube is then derotated and mean combined to produce the final image (see Fig. 2.11).

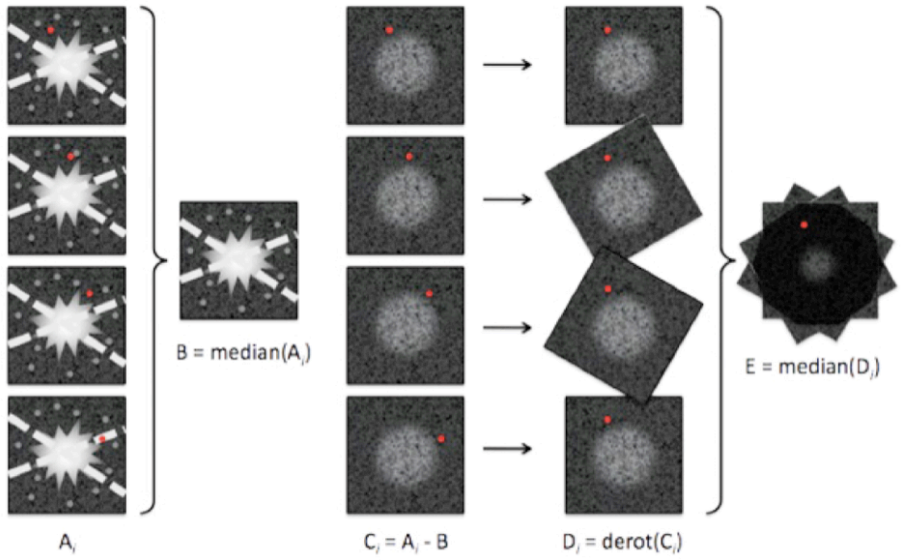

FIGURE 2.11: Median subtraction applied to Angular Differential Imaging technique. Credit: C. Thalmann

2.4.2 Locally Optimized Combination of Images (LOCI) technique

The locally optimized combination of images (LOCI, Lafrenière et al., 2007) techniques create a reference PSF as a linear combination of reference images, where the residual noise is minimized in subregions.

2.4.3 Principal Component Analysis (PCA)

Principal component analysis (PCA, Soummer et al., 2012, Amara et al., 2012) based algorithms reconstruct a reference PSF as the projection of the image onto a low-rank subspace (the principal components). With a sufficiently low number of principal components, the companion signal is not reconstructed and it can be retrieved after PSF subtraction.

2.5 First results and limitations

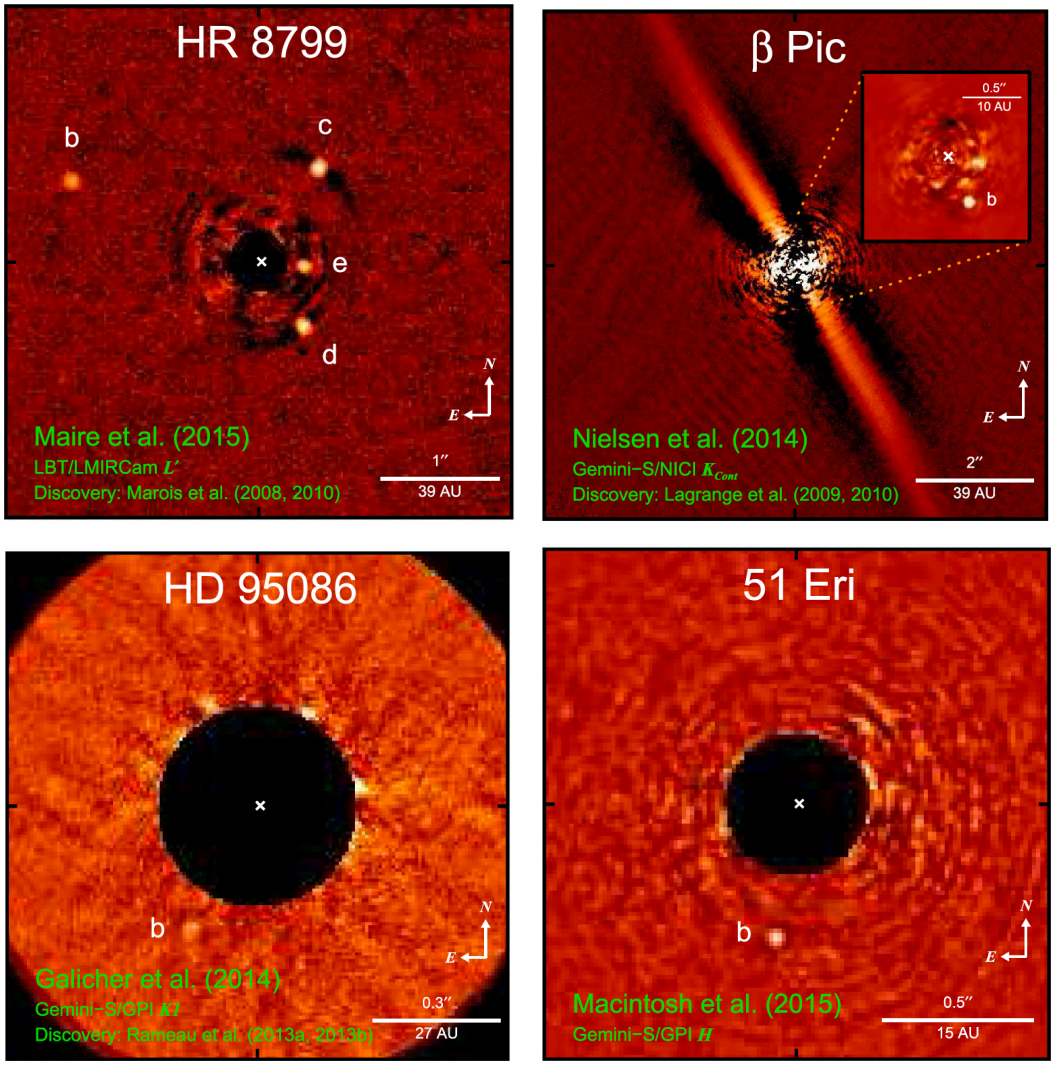

FIGURE 2.12: Gallery of imaged planets at small separations ($<$ $100AU$). From top left to bottom right: HR8799 (Marois et al., 2008), β Pictoris (Lagrange et al., 2009), HD95086 (Rameau et al., 2013), and 51 Eridani (Macintosh et al., 2015). Images from Bowler, 2016.

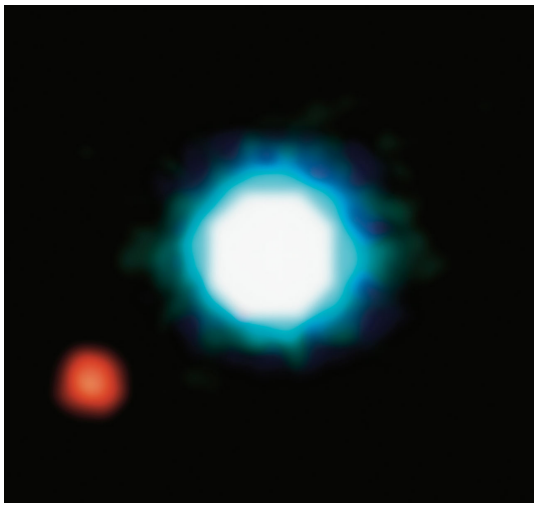

FIGURE 2.13: First imaged exoplanet, thanks to AO techniques (Chauvin et al., 2004): a giant planet (5 Jupiter masses, 55 AU) orbiting the brown dwarf 2M1207. The photo is based on three near-infrared exposures (in the H, K and L wavebands) with the NACO adaptive-optics facility at the 8.2-m VLT Yepun telescope at the ESO Paranal Observatory.

The direct detection method has not been as prolific as indirect methods, being a fairly new method for exoplanet imaging, and especially because of an increased dependence on hardware performance. While the first planetary-mass companion was detected only in 2004, around a brown dwarf (see Fig. 2.13), several determining discoveries have been made by this technique. The first planetary system, composed of four giant planets, was imaged around HR 8799 (Marois et al., 2008, see Fig. 2.12, top left), using the Gemini and the W. M. Keck observatory on Hawaii's Mauna Kea, exploiting the ADI technique (see Sect. 2.3.1). Only one year after, a giant planet was discovered orbiting around β Pictoris (Lagrange et al., 2009, see Fig. 2.12, top right), an A-type star best known for its circumstellar disk. Ten years later, a second planet was identified (Lagrange et al., 2019). HD 95086 b was confirmed in 2013 (Rameau et al., 2013, see Fig. 2.12, bottom left), with infrared observations, using the NACO instrument on the VLT: a $5M_J$ exoplanet orbiting a young A-class pre-main-sequence star, at a distance of about 60 AU. The first exoplanet detected by the Gemini Planet Imager (GPI), installed on the Gemini South Telescope in Chile, is 51 Eridani b, imaged in 2014 (Macintosh et al., 2015, see Fig. 2.12, bottom right). It is a Jupiter-like planet, with mass between 3 and $11M_J$, and distance of $\sim 11AU$. The first exoplanet detected by the instrument SPHERE (Spectro-Polarimetric High-Contrast Exoplanet Research, Beuzit, 2013) is a super Jupiter orbiting the star HIP 65426 (Chauvin et al., 2017, see Fig. 2.14, left and center), a young star without a debris disk. It was one of the first planets imaged by the JWST (Carter et al., 2022). The first confirmed image of a newborn planet was released in 2018 (Keppler et al., 2018, see Fig. 2.14, left): the young planet PSD 70 b, forming in the protoplanetary disk around its star.
Direct detection (with spectroscopy) is essential to determine planet parameters, as temperature, chemical composition and structure of a possible atmosphere, presence of clouds. These are crucial elements to constrain planet formation and evolution models. The sin i ambiguity of the radial velocity measurements can be removed by direct detection, which can not only constrain the mass of the planet, but also determine if planetary systems present a single orbital plane for all planets (as our

solar system). Young and active stars can only be efficiently studied by these techniques, which can lead to large progress in planet evolution models. The study of the luminosity and the spectrum of planets at different ages can also add important information to these models and the search for life (through atmosphere and weather analysis). The direct detection is the only method capable of efficiently surveying the regions farther away from the star. These aspects make the direct and indirect (especially radial velocity) methods complementary: indirect methods privilege closer and older (and so colder) planets, while direct methods are better suited for farther and younger (so hotter) planets.
As discussed before, direct detection has major limitations, linked to the brightness difference and angular separation between planet and star, and a combination of hardware and software techniques is used to increase sensitivity. As for indirect methods, it is important to confirm that the object is indeed gravitationally linked to the star and not a background object (as happened to the HD 131399 Ab, firstly detected as a planet, and then proven to be a background star, Nielsen et al., 2017). It is important to verify that the movement of the planet (right ascension, and declination) is consistent with the star: this can be obtained by repeating the observations multiple times at different epochs, to take advantage of the movement of the star-planet system with respect to the background objects.

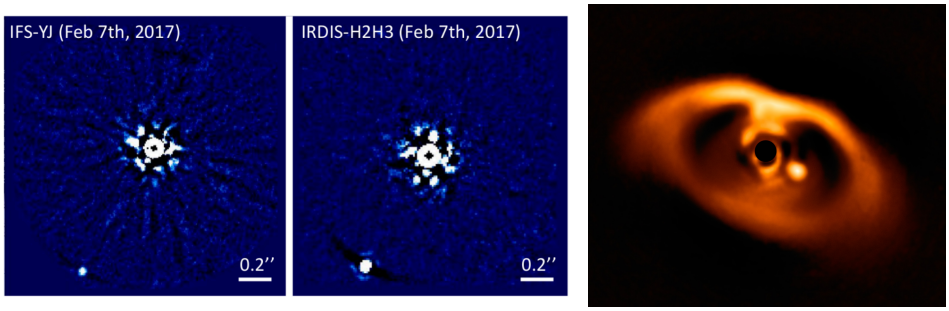

FIGURE 2.14: Planets imaged with the instrument SPHERE, on the VLT: HIP 65426 b (left and center, Chauvin et al., 2017), and PDS 70 b (right, Keppler et al., 2018).

Major improvements will come from the new ground and space-based large telescopes (ELT, TMT, GMT, JWST), for which the development of better adaptive optics systems, more efficient coronagraphic techniques, and advanced postprocessing algorithms will unleash their full potential. The Mid-infrared Extremely Large Telescope (ELT) Imager and Spectrograph (METIS, Brandl et al., 2008, Brandl et al., 2018, see Chapt. 4) is the perfect example of a combination of these techniques (large telescope, high contrast imaging, high resolution spectroscopy, adaptive optics) in the mid-infrared regime.

2.6 The mid-infrared regime

The mid-IR regime is very well suited for exoplanets detection and characterization. In the mid-IR regime, the brightness difference between the exoplanet and the host star is largely attenuated with respect to the optical wavelengths (see Fig. 2.15, and Fig. 2.16). A clear example is the detection of a planetary mass companion to HD95086 (Rameau et al., 2013), evident in L band, but at first undetected in H and Ks (Meshkat et al., 2013). This is even more important for circumstellar disks, where the opacity of the dust grains strongly affects shorter wavelengths (Quanz et al., 2015).

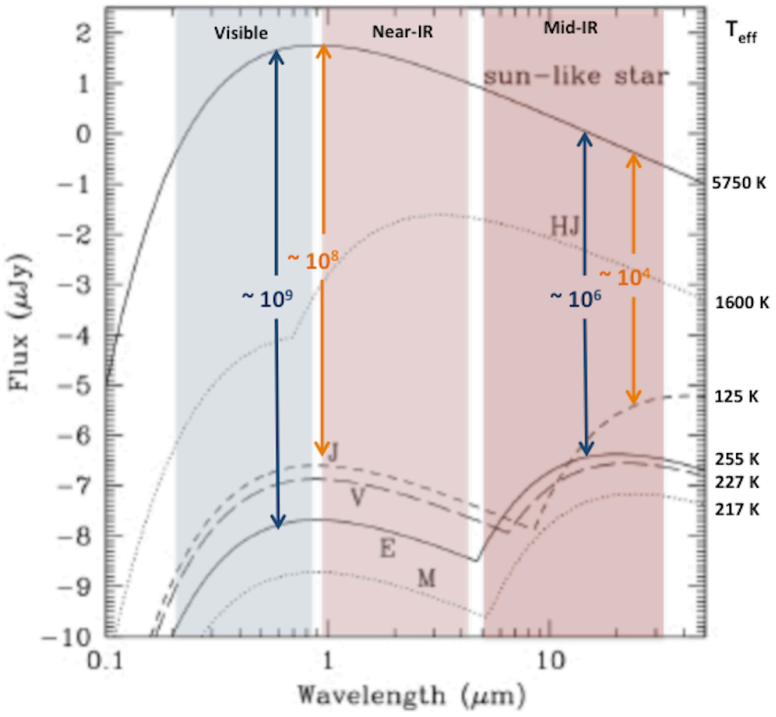

FIGURE 2.15: The visible and infrared portion of the black body spectrum of the Sun, few planets of the Solar System, and one hot Jupiter (with $T_{eff} = 1600K$ and albedo $A = 0.05$). The effective temperatures are shown. The contrast defined as F_s/F_p, where F_s is the flux of the star and F_p is the flux of the planet, is shown for the Earth ($\sim 10^9$ in the visible, and $\sim 10^6$ in the mid-IR), Jupiter ($\sim 10^8$ in the visible, and $\sim 10^4$ in the mid-IR), and hot Jupiter ($\sim 10^4$ in the near-IR). Credits: Seager et al., 2010.

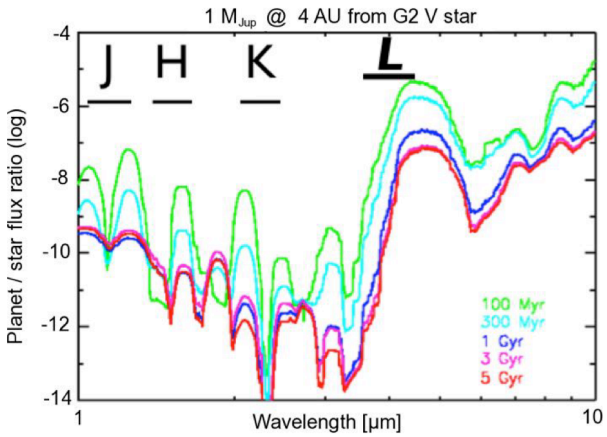

FIGURE 2.16: Expected planet/star flux ratio for non-irradiated Jupiter-mass planets at various ages (Burrows et al., 2004), and assuming a Sun-like host star.

From the instrument point of view, the AO systems provide higher Strehl ratios in the infrared compared to optical and NIR (Strehl ratio $\propto \lambda^{6/5}$, resulting in 95% in L band for modern AO systems).

The gas in the protoplanetary disks is responsible for the dynamics of dust particles and planets migration inside the disk and supplies the ingredients for giant planets formation. By analysing it, expecially in the region between 1 and 10 AU, where most planets form, we can have a better understanding of the planetary formation processes and their diversity. The mid-IR regime is excellent to study the warm gas in the inner disk (as the CO rovibrational emission at $4.7\mu m$) and, thanks to the high spectral resolution, it is possible to resolve line profiles and analyse gas kinematics down to 0.1 AU, as well as water and organics (CH_4 at $7.7\mu m$, C_2H_2 at $13.7\mu m$, HCN at $14\mu m$). The combination of high spectral and spatial resolution, together with photometry in other wavelengths, allow spectral imaging of the spatial distribution of disk material and kinematics of warm proto-planetary gas. Observing and analysing the warm CO gas in the disk may allow to understand if a gap in the disk is due to a forming planet (the gas signature will be offset from the local disk velocity by $5 - 10km/s$, due to the planet's own motion around the star), or to photo-evaporation of gas or even grain growth, resulting in lower opacity. Analysing the cometary ice volatiles in the L-M band ($3 - 5\mu m$) may help in constraining the composition of the formation disk of the Sun, just before the formation of planets. Simultaneously, low resolution N band ($8 - 13\mu m$) spectroscopy allows measurements of solid, non-volatile components (silicates): the co-existance of amorphous and cristalline phase in cometary dust suggests that the cristalline silicates may have been processed in hot environment, close to the Sun, before being inserted into cometary nuclei, implying an efficient radial mixing of the material in the proto-planetary disk.
However, the IR regime has a strong drawback: high background emission. To limit the background emission from the telescope and its optics, it is important to reduce the warm components in the beam. In order to have a better measurement of the background emission, chopping between source and "sky" is a well-known technique. It is also possible to increase the sensitivity of a background-limited instrument, by increasing the observation time (at first order, SNR$\propto\sqrt{t}$).

Part II

Design

Chapter 3

Design of vortex phase masks (VC) for L, M, N bands

The direct detection of exoplanets requires a high level of light suppression, to reduce the light of the star, without affecting the companion. Coronagraphs can achieve high contrast, by blocking the starlight. Between the various devices presented in Chapter 2, we will focus on the vortex coronagraph. It introduces a phase-shift to the on-axis starlight, rejecting it outside the geometric image of the pupil. This chapter is based on previous work published in Carlomagno et al., 2014.

3.1 Description

The Vortex coronagraph (VC) consists of a focal plane phase mask (the vortex phase mask) and a pupil plane amplitude mask (the Lyot stop). The focal mask imposes a phase ramp to the on-axis starlight, rejecting it, by destructive interference, outside the geometric image of the pupil. This diffracted light is then blocked through a binary amplitude mask, the Lyot Stop, in the following pupil plane. This phase shift can be created by a vectorial optical vortex, which applies continuous opposite phase screws to the two orthogonal circular polarization states. The circular polarizations will experience a phase ramp $e^{i\phi} = e^{\pm il\theta}$, where l is the topological charge, the number of times the phase ϕ accumulates 2π along a closed path surrounding the phase singularity [1], and θ is the focal plane azimuthal coordinate. For a charge 2 coronagraph, the wave will undergo a $2 \times 2\pi$ phase shift within one revolution around the optical axis (see Fig. 3.1, left).

This phase shift is imposed by using a halfwave plate (HWP), constructed out of birefringent material, by changing the orientation of its fast axis. Subwavelength gratings (SG), micro-optical structures with period $\Lambda < \lambda/n$, can create achromatic birefringence: by optimizing the grating parameters (geometry and material), the chromatic birefringence $\Delta n(\lambda)$ can be tuned to be closely proportional to the wavelength over a wide spectral band. The phase retardance $\Delta\Phi_{TE-TM}(\lambda)$ introduced by subwavelength gratings between the two polarization components (TE, transverse electric, parallel to the grating grooves, and TM, transverse magnetic, orthogonal to the grating grooves) relates to the chromatic birefringence as follows

$$\Delta\Phi_{TE-TM}(\lambda) = \frac{2\pi}{\lambda} h \Delta n(\lambda), \tag{3.1}$$

where h is the optical path through the birifringent subwavelength grating. So, with $\Delta n \propto \lambda$, $\Delta\Phi_{TE-TM}$ becomes constant.

[1] It represent the height of the phase ramp, after a 2π rotation.

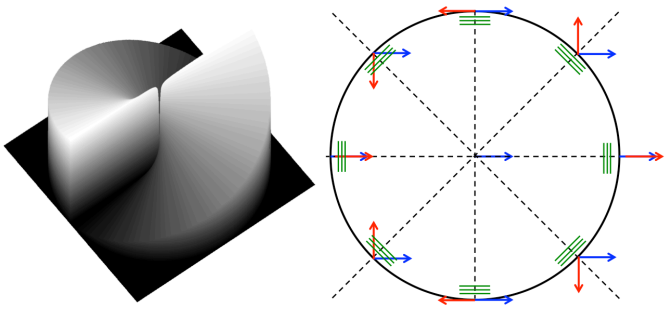

FIGURE 3.1: *Left*: Illustration of the $2 \times 2\pi$ phase ramp created by a charge-2 vortex. *Right*: Spatial variation of the optical axis orientation of a vector vortex phase mask coronagraph of topological charge 2 (VC2), obtained with a rotationally symmetric HWP. An incoming horizontal polarization (blue arrow) is transformed by the vector vortex so that it spins around its center twice as fast as the azimuthal coordinate θ (red arrows), defining the orientation of the SG (green lines), always perpendicular to the optical axis (dashed lines).

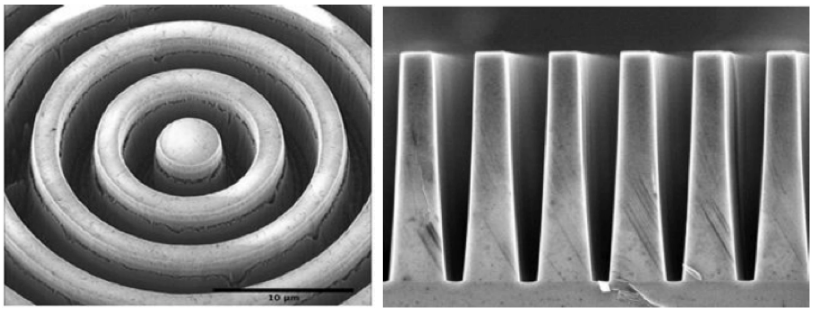

FIGURE 3.2: SEM pictures of an L-band AGPM fabricated at the Ångström Laboratory using reactive ion etching and nanoimprint lithography.

The Annular Groove Phase Mask (AGPM, see Fig. 3.2) is a charge-2 vector vortex coronagraph based on a SG, etched into a diamond substrate, with an anti-reflective 2D grating on the back of the mask (to reduce the multiple reflections inside the substrate, see Sect. 3.2.1.2). Its throughput is close to 100%, with the sources of throughput loss coming from the mask substrate, and the reflections loss in the annular grating side. The inner working angle (IWA) can be down to $1\lambda/D$ and it creates a clear 360° discovery space.

3.2 Design of mid-infrared AGPMs

3.2.1 RCWA

The optimization of the design of the AGPM uses an algorithm based on the *Rigorous Coupled Wave Analysis* (RCWA, Moharam et al., 1982), coded in MATLAB®(Mawet et al., 2005b). The RCWA solves Maxwell's equations, assuming infinite grating and parallel grating lines. The principal optimization parameters of the subwavelength grating profile are the filling factor F and the depth h (see Fig. 3.3, left).

Thanks to its great optical, mechanical, thermal and chemical characteristics, synthetic diamond turns out to be a very well suited material to manufacture such

AGPMs, based on an advanced micro-fabrication technique using nano-imprint lithography and reactive ion etching (Forsberg et al., 2013, Forsberg et al., 2014). Due to fabrication issues, the walls of the etched grooves are not perfectly vertical, showing a slope $\alpha \sim 3°$ in the present case (see Fig. 3.3).

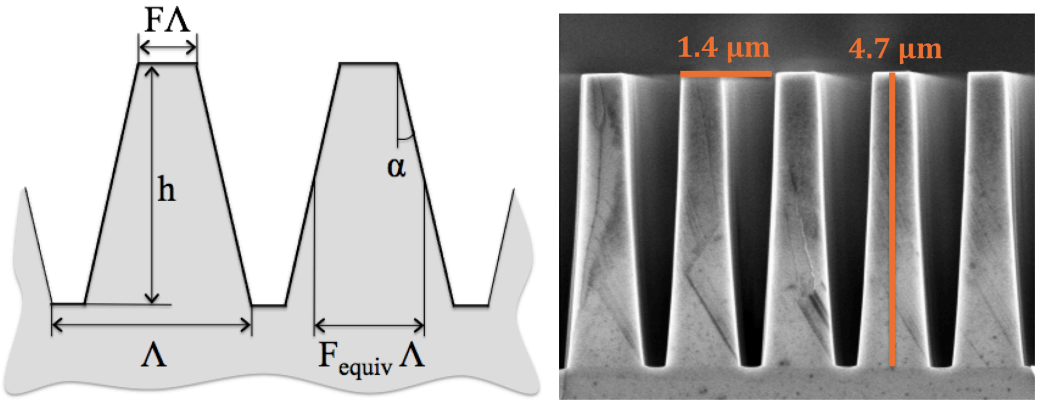

FIGURE 3.3: **Left**: Schematic diagram of a trapezoidal grating. The filling factor F is such that $F\Lambda$ corresponds to the line width on top of the walls. **Right**: Cross sectional view of a diamond AGPM dedicated to the L band. The grating sidewalls have an angle $\alpha \sim 3°$ and an average width $F_{\text{equiv}}\Lambda \sim 0.5\mu m$.

The period Λ of the subwavelength grating is kept constant during the optimization. Its value is determined by the subwavelength limit:

$$\Lambda < \frac{\lambda_{\min}}{n(\lambda_{\min})} \tag{3.2}$$

where $\lambda_{\min}$ is the shortest wavelength of the considered band (with a $100nm$ security margin), and $n(\lambda_{\min})$ is the refractive index of the substrate (diamond in our case) calculated at this wavelength. The refractive index was computed considering polynomial regressions and Sellmeier equations. The final values of the refractive index and the period are shown in Tab. 3.1, for several considered bands.

TABLE 3.1: Calculated diamond refractive indices and subwavelength grating periods, for several considered mid-IR spectral windows.

Band	Bandwidth [μm]	$\lambda_{\min}[\mu m]$	$n(\lambda_{\min})$	Period Λ [μm]
L	3.5 – 4.1	3.4	2.3814	1.42
M	4.6 – 5	4.5	2.3810	1.89
lower N	8 – 11.3	7.9	2.3806	3.32
upper N	11 – 13.2	10.9	2.3805	4.58

3.2.1.1 Null depth definition

Theoretically, a vortex coronagraph should provide a perfect on-axis light cancellation, but imperfections in the vortex phase mask prevent it. The metric used for the optimization is the *null depth* $N(\lambda)$, defined as the contrast, integrated over the

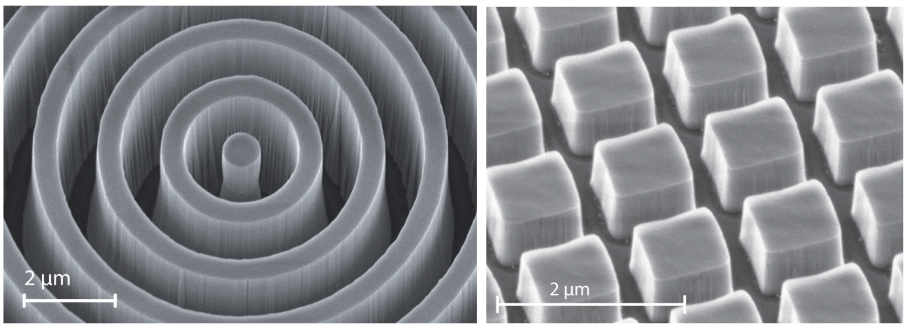

FIGURE 3.4: SEM pictures of an L-band AGPM fabricated at the Ångström Laboratory using reactive ion etching and nanoimprint lithography. **Left**: Annular grooves etched on the frontside of the component. **Right**: Antireflective structure etched on the backside.

whole point spread function (PSF) (Mawet et al., 2005a)[2]:

$$N_{\text{theo}}(\lambda) = \frac{I_{\text{coro}}(\lambda)}{I_{\text{off}}(\lambda)} = \frac{[1-\sqrt{q(\lambda)}]^2 + \epsilon(\lambda)^2\sqrt{q(\lambda)}}{[1+\sqrt{q(\lambda)}]^2} \tag{3.3}$$

where I_{coro} is the signal intensity when the input beam is centered on the mask, while I_{off} is the signal intensity when the input beam is far from the mask center, $\epsilon(\lambda)$ is the phase error with respect to π, and $q(\lambda)$ is the flux ratio between the polarization components transverse electric (TE) and transverse magnetic (TM) after propagation through the mask, respectively. It is in this equation that all geometrical parameters (filling factor F, depth h and sidewall angle α) are taken into account, via $\epsilon(\lambda)$ and $q(\lambda)$.

The optimization process follows a precise procedure. First, the RCWA algorithm provides a two-dimensional map of the mean theoretical null depth as a function of the optimization parameters (filling factor F and depth h), then the same algorithm is used for a more precise optimization around the optimal parameters obtained after the first step. The results of the optimization will be presented in Sect. 3.2.2.

3.2.1.2 Influence of the ghost

The optimized parameters and null depths obtained from RCWA simulations assume that only the zeroth order of the subwavelength grating is transmitted. In practice, the presence of a ghost signal has been confirmed by laboratory measurements. It is the result of multiple reflections within the substrate. The AGPM pattern etched on the frontside of the substrate (Fig. 3.4, left) partially reduces the reflections, acting as an antireflective layer, to some extent. Most of the ghost signal is actually caused by the reflection on the flat interface, on the other side of the substrate. Therefore, an anti-reflective grating (ARG) needs to be etched on the backside of the component (Fig. 3.4, right) to avoid these reflections. Typically, a binary square-shaped structure, whose parameters are optimized through RCWA, is used for the antireflection. For diamond in L band, the raw backside reflection is 17%, while the ARG reduces it to $1-2\%$ (Forsberg et al., 2013).

[2]This null depth is equal to the peak-to-peak attenuation if the coronagraph is only limited by chromatism (in which case the coronagraph PSF is just a scaled-down version of the original PSF).

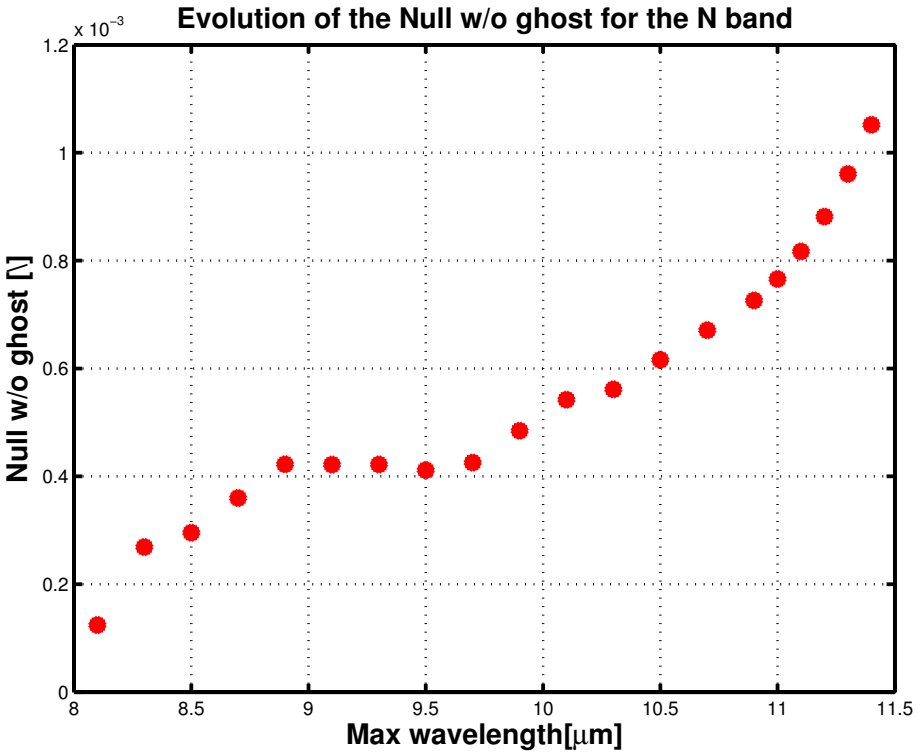

FIGURE 3.5: Definition of the lower N band spectral window. Optimized mean null depth for a minimal wavelength of $8\mu m$, as a function of the maximal wavelength. The desired mean null depth 10^{-3} is obtained for the bandwidth $8 - 11.3\mu m$.

The total null depth is then the sum of two components:

$$N_{\text{total}}(\lambda) = N_{\text{theo}}(\lambda) + N_{\text{ghost}}(\lambda) \tag{3.4}$$

where

$$N_{\text{ghost}}(\lambda) = \frac{I_{\text{ghost}}(\lambda)}{I_{\text{off}}(\lambda)} \, . \tag{3.5}$$

The expected performance for the total null depth (considering the ghost) is improved by the use of the ARG (see Sect. 3.2.2).
The first AGPMs were optimized to cover mid-IR bands (L, M, and N), because, on one hand the grating parameters are proportional to the wavelength (it is then easier to manufacture mid-IR gratings with respect to the VIS); on the other hand, this regime is particularly suitable for exoplanet detection (see Sect. 2.6).

Because the N band is very wide ($8 - 13.2\mu m$), it is difficult to cover it with a single component. Therefore, it has generally been divided into two sub-bands (lower N band, N1, and upper N band, N2), on which the AGPM design was optimized. The N2 band was originally defined to suit the VISIR mid infrared camera of the VLT: $11 - 13.2\mu m$. One of these is now installed on VISIR and shows promising performance (Delacroix et al., 2012). Since then, another definition of the N2 band was used specifically for the NEAR experiment (Wagner et al., 2021) on the VISIR camera, leading to an AGPM optimization on the $10 - 12.5\mu m$ range. Concerning the N1 band, we followed a different path. A constraint was imposed on the mean

null depth, which should be smaller than 10^{-3}. We could then calculate the maximal width of the spectral band, that we have arbitrarily started at $8\mu m$, to define the lower N band: $8 - 11.3\mu m$ (see Fig. 3.5).

3.2.2 Optimal AGPM parameters and null depth at L, M and N bands

The results of our RCWA simulations are presented in Tab. 3.2, with the optimized filling factor F, grating depth h, and mean null depth N over the whole bandwidth.

The AGPM mean null depth (over each spectral band) is shown in Fig. 3.6 (left), as a function of the profile parameters F and h. The dark blue region in the center of the figure corresponds to the optimal parameters region, providing the best contrast expressed here on a logarithmic scale. In Fig. 3.6 (right), we see that the theoretical optimal mean null depth N is comprised between 10^{-4} and 10^{-3}. When the ghost is taken into account, the somewhat degraded null depth value is still close to 10^{-3}, showing the excellent performance of the ARG.

TABLE 3.2: Optimized filling factor F, grating depth h, and mean null depth N w/o ghost, for several considered mid-IR spectral windows.

Band	Bandwidth	F	$h[\mu m]$	N
L	3.5 – 4.1	0.45	5.22	4.1×10^{-4}
M	4.6 – 5	0.41	6.07	3.4×10^{-4}
N1	8 – 11.3	0.49	15.77	10^{-3}
N2	11 – 13.2	0.45	16.55	4.1×10^{-4}

3.2.2.1 Optimal AGPM parameters and null depth at L+M bands

It is possible to apply the optimization procedure to a combination of bands, when the phase mask has to cover more than one band at the same time. We tried to optimize the AGPM parameters for L and M bands together. Tab. 3.3 presents the optimized parameters and Fig. 3.7 shows that the theoretical optimal mean null depth N is just below 10^{-3}. This design is at the edge of what it is manufacturable, because, as Fig. 3.7 shows, with a sidewall angle α of 3°, the optmimum combination of filling factor F and depth d is close to an impossible geometrical solution (the upper right corner corresponds to the merging of the sidewalls).

TABLE 3.3: Optimized filling factor F, grating depth h, and mean null depth N, for L+M spectral bands.

Band	Bandwidth	F	$h[\mu m]$	N
L + M	3.5 – 4.1 + 4.6 – 5	0.49	7.17	7.9×10^{-4}

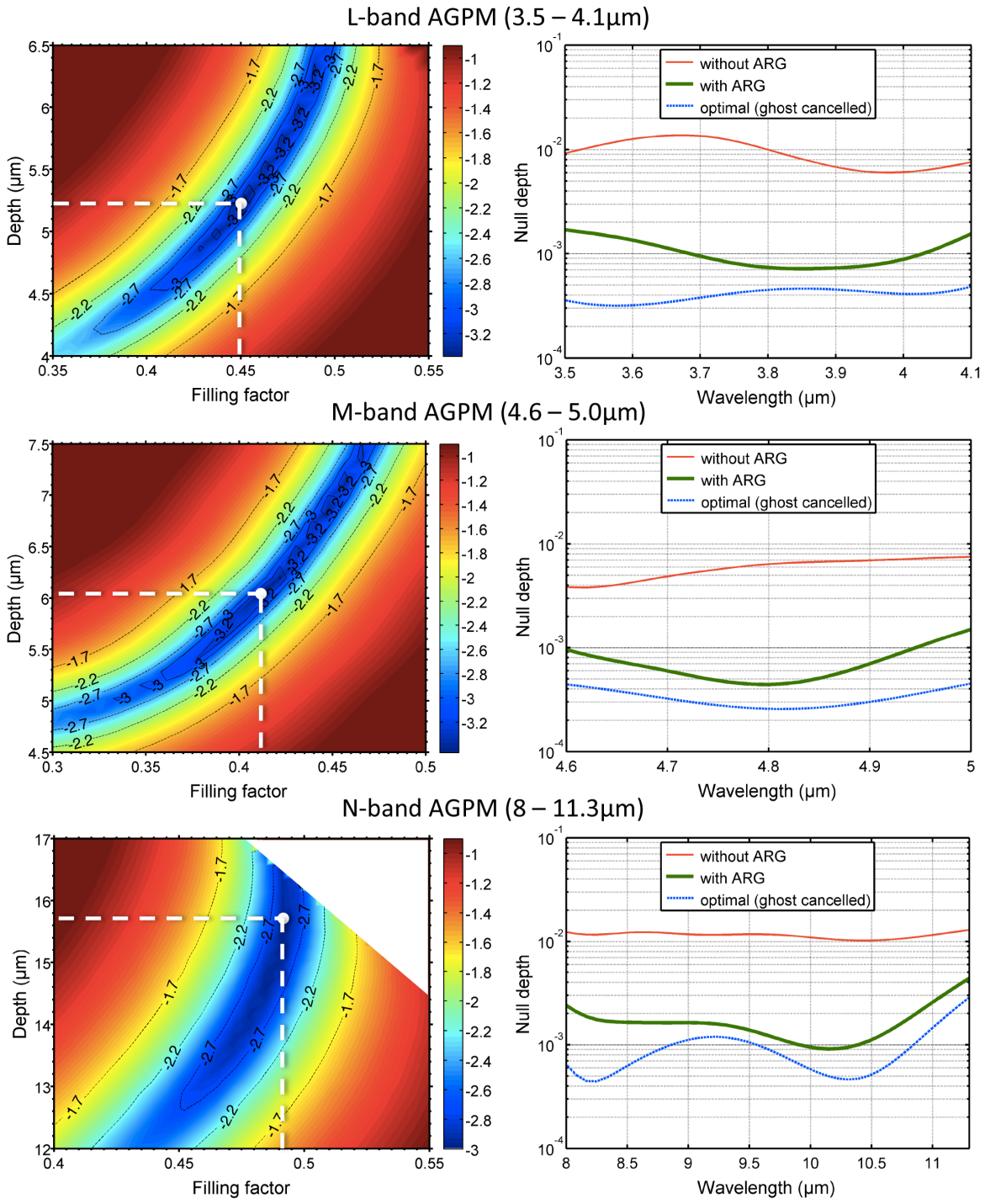

FIGURE 3.6: RCWA multiparametric simulations for the L, M and N1 bands. **Left**: Mean null depth map, function of depth and filling factor, showing the optimal design values. For the N band, the upper right corner does not correspond to a possible geometrical solution, because of the merging of the sidewalls. **Right**: Computed coronagraphic performance of the AGPM, showing the benefits of etching an ARG on the backside of the component.

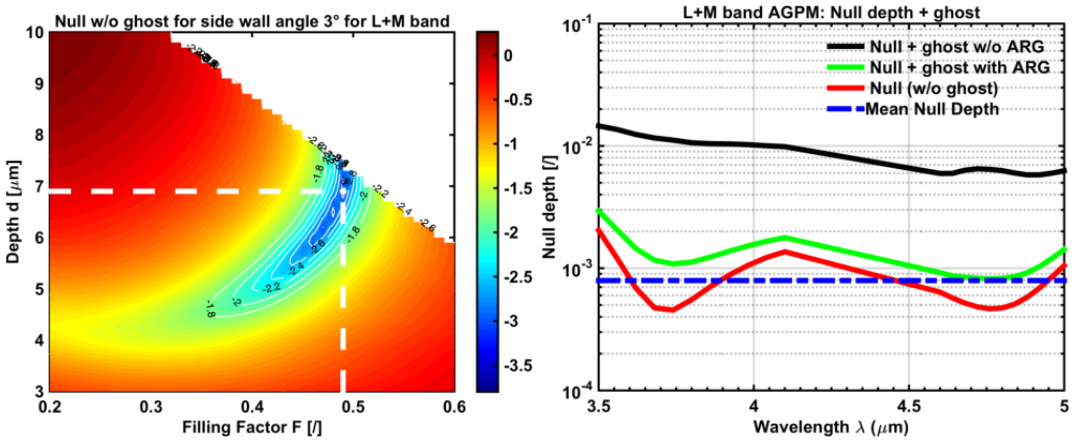

FIGURE 3.7: RCWA multiparametric simulations for the L + M band. **Left**: Mean null depth map, as a function of depth and filling factor, showing the optimal design values. **Right**: Computed coronagraphic performance of the AGPM, showing the benefits of etching an ARG on the backside of the component.

Chapter 4

The METIS coronagraphic modes

The METIS instrument on the ELT will provide significant improvement in high contrast imaging, by relying on one side on the 39-m diameter of the telescope, and on the other on the high capability of stellar suppression of the combination of adaptive optics and coronagraphy. In this chapter, we will focus on the description of the instrument, with an emphasis on the coronagraphic modes. This chapter is based on previous work published in Carlomagno et al., 2020.

4.1 The ELT/METIS instrument

METIS (Brandl et al., 2008, Brandl et al., 2018) is one of the first-light instruments of the ELT. It consists of two diffraction-limited imagers covering the mid-infrared wavelength range featuring high-contrast imaging (HCI) and medium-resolution long slit spectroscopy, and of an integral field spectrograph. With its mid-infrared capabilities, METIS will provide a unique view on the Universe, with science cases ranging from our Solar system to high-redshift galaxies, and including the study of planetary formation and planetary systems as a prime scientific goal.

To enable HCI, METIS will implement two state-of-the-art coronagraphic concepts: a focal plane coronagraph, the *vortex coronagraph* (VC), and a pupil plane coronagraph, the *apodizing phase plate* (APP). These coronagraphic concepts are complementary in terms of discovery space and sensitivity to instrumental errors. They will be used for different science cases and/or under different environmental conditions.

Over the years, the METIS instrument has experienced several evolutions. The configuration presented here is the one of the Preliminary Design Review (PDR), from May 2019. Some details have been modified since the PDR (detailed design of ELT pupil, pupil stop and apodization, one single AGPM for N band, more realistic SCAO simulations with wind load and other effects, ...), however the results presented here remain largely valid and relevant.

4.2 Instrumental concept

Before entering the METIS cryostat, the light collected by the ELT primary mirror is reflected by a series of five additional mirrors including the ELT-M4 deformable mirror, as well as a tip-tilt mirror (ELT-M5). After bouncing off the final mirror of the ELT optical train (M6), the light then enters the METIS cryostat, which ensures low background emission for all further optical components, and includes four main subsystems (see Fig. 4.1):

- The common fore-optics (CFO), which formats the beam for injection into the scientific cameras, and includes important functionalities such as atmospheric

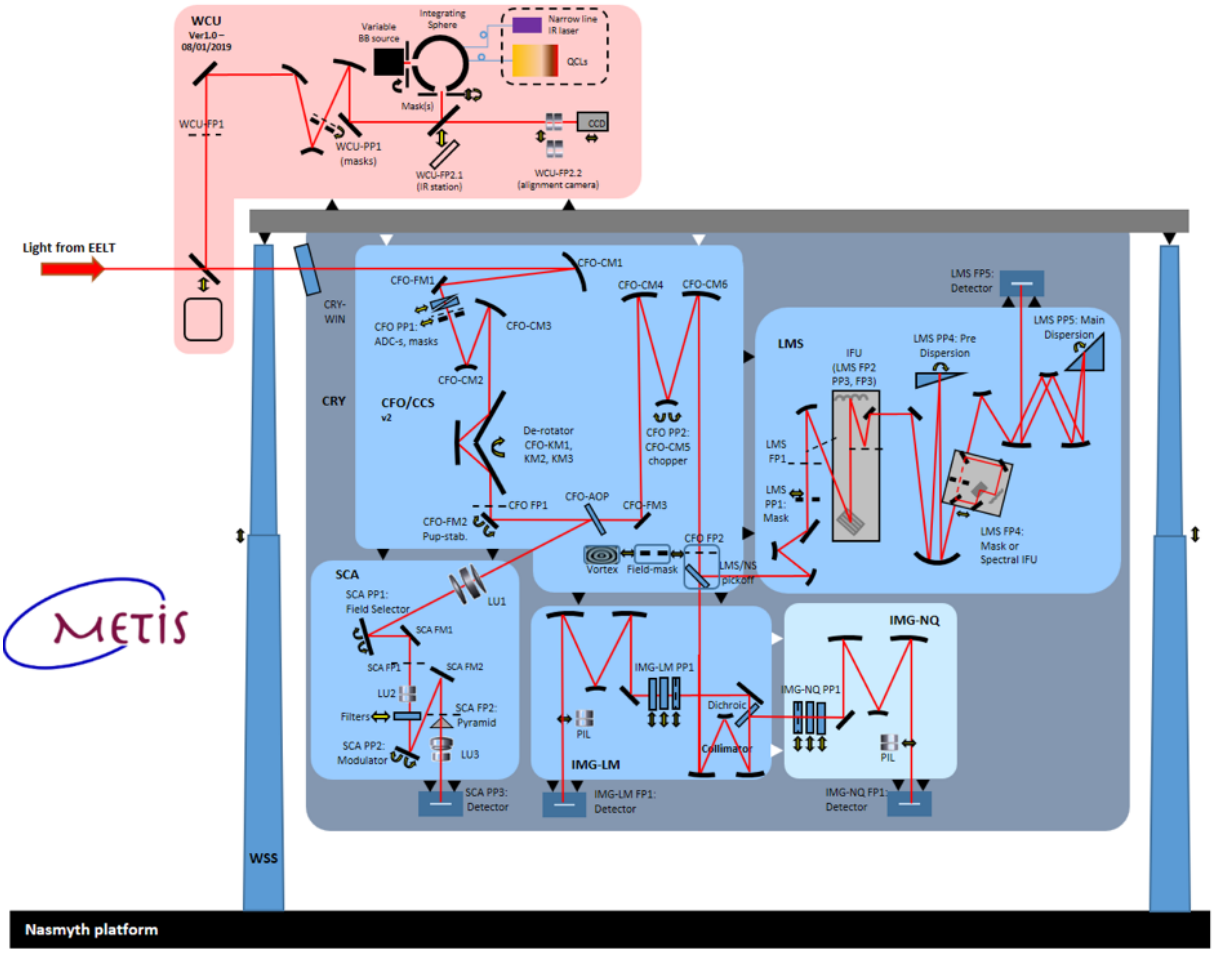

FIGURE 4.1: Optical overview of the METIS instrument at PDR.

dispersion compensation, derotation, pupil stabilization, chopping, and coronagraphy;

- A single-conjugated adaptive optics (SCAO) system, which implements an infrared pyramid wavefront sensor, and controls the shape of the ELT-M4 deformable mirror;
- A pair of diffraction-limited imaging cameras in L/M and N bands with $10'' \times 10''$ field of view (referred to as IMG-LM and IMG-N, respectively), including coronagraphy at L, M, and N bands, and medium-resolution ($R \sim 5000$) long slit spectroscopy;
- An integral-field high-resolution ($R \sim 100,000$) spectrograph, referred to as LMS, operating at L/M band (2.9–5.3 μm) with $0''5 \times 1''$ field of view and including coronagraphic capabilities.

METIS also comprises a warm calibration unit (WCU), which provides calibration sources for all observing modes.

4.3 Implementation of high-contrast imaging

Inside METIS, the CFO sub-system provides a series of addressable pupil planes and focal planes to implement coronagraphic capabilities, as illustrated in Fig. 4.2. In

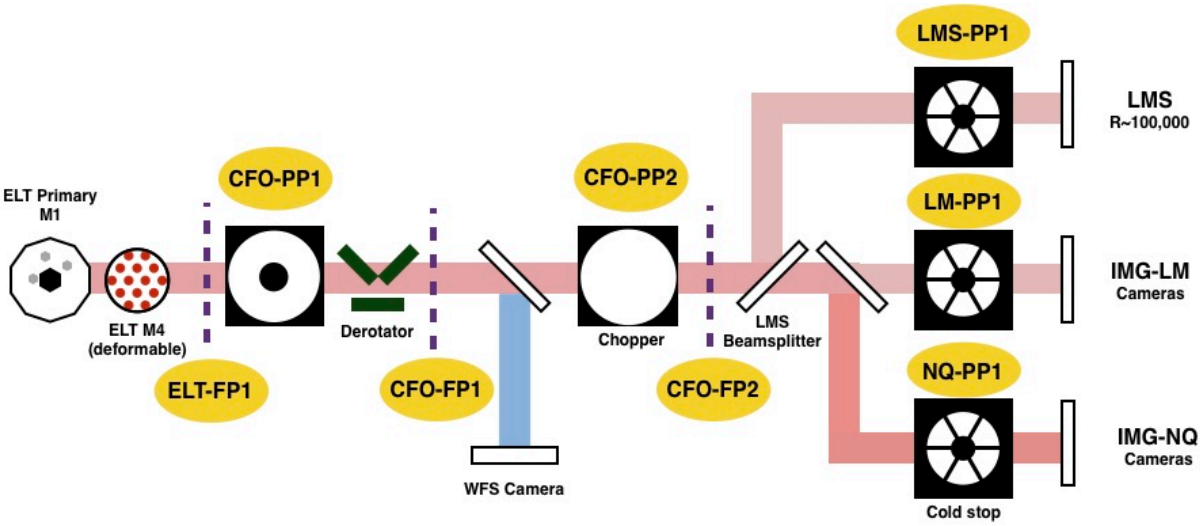

FIGURE 4.2: Schematic layout of the relevant optical components for HCI in METIS.

particular, the CFO-PP1 pupil plane and the CFO-FP2 focal plane will be the host of wheel mechanisms that can insert coronagraphic components into the beam. This is also the case of the first pupil plane located inside the imager and spectrograph sub-systems (LM-PP1 and NQ-PP1, called IMG-PP1 in the rest of the manuscript, and LMS-PP1). This combination of two pupil planes with one focal plane in between enables the implementation of the RAVC (see Sect. 4.5.2), while the gvAPP only requires one pupil plane and will be implemented directly into the IMG-LM and LMS sub-systems. Enabling HCI relies however not only on coronagraphic components, but also on a series of functionalities that are provided by the various METIS sub-systems. The most important features of METIS for HCI are detailed here, following the path of light through the instrument.

CFO-PP1 is located upstream of any derotation or pupil stabilization mirror. Because the image of the ELT pupil will not be stable there, and will be rotating during the observations, this pupil plane can only implement rotationally symmetric masks, which is the case of the greyscale apodizer used for the RAVC concept. More advanced apodizer designs taking into account spider arms cannot be implemented there, nor the APP, whose design is also tuned to the exact shape of the ELT pupil. No undersized cold stop will be implemented in CFO-PP1 for the coronagraphic modes, in order to transmit the full image of the ELT-M1 pupil. Because the image of ELT-M1 will drift with respect to the position of CFO-PP1 during observations, the greyscale apodizer will be slightly oversized. In addition to hosting the greyscale apodizer, CFO-PP1 will also host two fixed atmospheric dispersion compensators (ADC), which will be optimized for two specific airmasses (corresponding to zenith angles of 25 and 41 degrees). These ADCs can be used together with the greyscale apodizer thanks to a double mechanism at CFO-PP1, with the ADCs being slightly upstream of the location of the pupil image.

Following CFO-PP1, a K-mirror will be used to derotate the beam. The derotator can be used either to stabilize the field or the pupil. The latter option will be used for the HCI observing modes, in order to exploit angular differential imaging techniques. The next focal plane (CFO-FP1) will not be populated by any optical component, except for a nearby pupil stabilization mirror that will be used to compensate for residual drifts of the pupil image due to the ELT pupil motion and to the

imperfect derotation, and to freeze the position of the ELT-M1 pupil in the downstream optical train with an accuracy of 1% of the projected M1 diameter. This pupil stabilization mirror will be fed by measurements from the SCAO pyramid wavefront sensor, which will measure the position of the ELT-M1 pupil in real time. The SCAO sub-system will pick up the near-infrared part of the beam using a dichroics downstream of the pupil stabilization mirror, which reflects the H and K band signal towards SCAO and transmits the longer wavelengths to the science cameras. The next pupil plane (CFO-PP2) will be hosting the cold chopping mirror, while CFO-FP2 provides the mechanism to insert both the vortex phase mask and/or the LMS pickoff mirror into the beam. The gvAPPs and Lyot stops will be located in IMG-PP1 and LMS-PP1, where the stabilisation of the ELT-M1 pupil image will allow efficient use of these masks. The L and M-band vortex phase masks and the image slicer in the LMS will be aligned on the same optical axis to maximize the discovery space around the vortex when used in combination with the LMS. When combined with the gvAPP, the image slicer of the LMS will be fed with one of the two dark holes created by the gvAPP.

4.4 HCI performance requirements

The development of the METIS instrument is guided by a set of top-level requirements defined by ESO. Because it specifically aims for high-contrast imaging, METIS has a formal requirement on the HCI performance. This requirement is expressed as the 5σ sensitivity in terms of contrast that needs to be reached after post-processing of a 1-h observing sequence on a relatively bright star ($L \leqslant 6$). The requirement, defined at L band, is to reach a post-processed 5σ sensitivity of 3×10^{-5} in terms of contrast at $5\lambda/D$ (i.e., 0"1), with a goal of 10^{-6} at $2\lambda/D$ (i.e., 0"04). In order to verify that this requirement can be fulfilled with the proposed instrumental concept, end-to-end simulations need to be performed, as described in the rest of this manuscript.

Before embarking in end-to-end simulations, it is useful to break down this requirement. There are several sources of errors that contribute to the overall HCI performance. The most fundamental limits are photon noise from residual stellar light and thermal background emission, and speckle noise associated with residual turbulence after SCAO closed-loop control. These contributions are detailed in Sect. 5.1. In addition, several sources of instrumental errors also affect the HCI performance budget, as described in Chapt. 6. While these effects are studied one by one, in practice they add up and interfere to create the final HCI performance. Considering the number of effects to take into account, and the fact that they do not simply add up quadratically (they can in some case constructively interfere), we will try to limit the influence of each individual contributor to 1/10th of the performance requirement, i.e., 3×10^{-6} at 0"1. This will be referred as our "goal".

4.5 METIS Coronagraphic Modes

4.5.1 Classical Vortex Coronagraph (CVC)

The METIS instrument will be equipped with an AGPM for the 4 bands, L, M, N1, and N2 (to cover the total N band). Concerning the Lyot stop, the central obstruction will be oversized to 33% of the external pupil diameter to reduce the total stellar leakage to about 3%, while keeping a high throughput of about 90% (computed with respect to the circularized ELT input pupil). The Lyot stop outer diameter is

fixed to 98% of the external pupil diameter, and the Lyot stop spider width to 3%, see Tab. 4.1.

4.5.2 Ring Apodized Vortex Coronagraph (RAVC)

The Ring Apodized Vortex Coronagraph (RAVC, Mawet et al., 2013a) combines a vortex coronagraph (focal plane and pupil plane) with an amplitude ring apodizer in the first pupil plane. It is then a three-stage optical system. The aim is to compensate for the presence of the huge central obstruction in the telescope pupil, by modulating the entrance pupil with a concentric apodizer (with chosen dimensions and transmittances), to perfectly cancel the on-axis sources at the Lyot stop level.

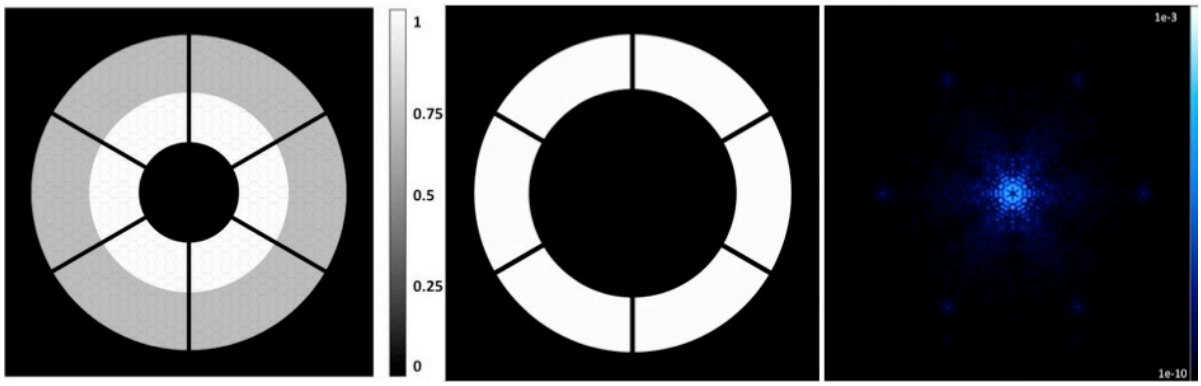

FIGURE 4.3: Input pupil (circularized version of the ELT pupil) with the greyscale apodizer, Lyot stop, and associated PSF for the charge-2 RAVC (field of view of 100 λ/D). The cancellation is not perfect because of the spider arms, for which the RAVC is not optimized.

The presence of a central obstruction induces residual light inside the Lyot stop, because of the intrinsic properties of vortex coronagraphs of moving light in and out of circular apertures. Adding a pupil ring apodizer, with radius r_1 and amplitude transmission coefficient t_1 for $r_1 < r < R$ and $t_0 = 1$ for $r_0 < r < r_1$, the pupil field after the vortex mask and the Lyot stop becomes (from Mawet et al., 2013a):

$$E_L(r) = \begin{cases} 0 & r < r_0 \\ -\left(\frac{r_0}{r}\right)^2 & r_0 < r < r_1 \\ (1-t_1)\left(\frac{r_1}{r}\right)^2 - \left(\frac{r_0}{r}\right)^2 & r_1 < r < R \end{cases} \tag{4.1}$$

It is then possible to completely cancel the light within $r_1 < r < R$ by varying the apodizer parameters, t_1 and r_1, which leads to an expression for the amplitude transmission:

$$t_1 = 1 - \left(\frac{r_0}{r_1}\right)^2 \tag{4.2}$$

The second parameter, the radius r_1, is optimized by maximizing the throughput T, defined as the ratio between the energy going through the ring and the energy normally transmitted by the centrally obscured telescope aperture:

$$T = \frac{t_1^2\left(1 - \left(\frac{r_1}{R}\right)^2\right)}{1 - \left(\frac{r_0}{R}\right)^2} \tag{4.3}$$

The final optimal parameters are defined as:

$$\begin{cases} t_{1,opt} = 1 - \frac{1}{4}\left(R_0^2 + R_0\sqrt{R_0^2+8}\right) \\ R_{1,opt} = \frac{R_0}{\sqrt{1-t1,opt}} \end{cases} \tag{4.4}$$

where $R_0 = r_0/R$ and $R_1 = r_1/R$ are the relative radii. Note that the RAVC configuration depends only on the central obstruction radius: the bigger this radius, the thinner the apodizer with a lower transmission.
For the circularized ELT/METIS pupil (with a central obstruction of 30%), we have (see Fig. 4.3):

$$R_0 = 0.30 \quad \rightarrow \quad \begin{cases} t_{1,opt} = 0.76 \\ R_{1,opt} = 0.62 \end{cases} \tag{4.5}$$

Figure 4.3 shows the final PSF for the RAVC concept: the perfect cancellation is not obtained because of the spiders (that are not considered in the RAVC optimization) and, to a smaller extent, the gaps between segments. The overall throughput of the RAVC for the METIS instrument is of 34% after the Lyot stop, and a total stellar leakage of about 0.2% in presence of spider arms (with the Lyot stop outer diameter at 98% of the external pupil diameter, and the Lyot stop spider width to 3%, see Tab. 4.1). For FDR, the final design of the apodizer will be numerically re-optimized to minimize the stellar leakage considering the exact ELT pupil.

TABLE 4.1: Lyot stop dimensions for CVC and RAVC.

Coronagraphic mode	Inner diameter [% of the external pupil diameter]	Outer diameter [% of the external pupil diameter]	Spiders [% of the external pupil diameter]
CVC	33	98	3
RAVC	65	98	3

Part III

End-to-end simulations

Chapter 5

Simulation tools

The high contrast imaging performance of the METIS instrument has been analysed with end-to-end simulations. The simulation tools are presented in this chapter: the adaptive optics simulations, the optical propagation, and the post-processing. The final result is given by contrast curves, which are used to analyse the different coronagraphic modes and instrumental effects. This chapter is based on previous work published in Carlomagno et al., 2020.

5.1 The METIS HCI end-to-end simulator

Obtaining a realistic estimation of the METIS HCI performance requires to perform end-to-end simulations, which must include three main steps:

1. perform AO simulations to provide residual phase screens;
2. propagate the residual phase screens through the instrument;
3. produce a mock HCI data set, in pupil stabilized mode, and analyse it to evaluate the associated performance, by applying a classic ADI-based post-processing methods to the image cube.

These three steps are detailed in the following sections.

5.1.1 Adaptive optics simulations

The quality of the adaptive optics correction provided by the SCAO module inside METIS will set the fundamental limits to its HCI performance. In the context of HCI observations, the SCAO module of METIS will generally be fed with bright, on-axis natural guide stars. Because HCI is at the heart of the METIS science cases, the SCAO system has been designed to provide the best possible performance for such guide stars. It is based on an infrared Pyramid wavefront sensor (PyWFS, Ragazzoni, 1996), which will feed a low-noise, high-speed, infrared electron-avalanche photo-diode array. The PyWFS is expected to provide better Strehl ratio than a standard Shack-Hartmann WFS (Hippler et al., 2019), but also a better sensitivity to low order modes.

METIS will use ELT-M4 and M5 to implement the AO correction. Assuming a median seeing of 0"65 and a stellar magnitude $K = 5$, the SCAO system is expected to deliver high Strehl ratio: above 90% at L band, and around 99% at N band (Hippler et al., 2019). The COMputing Platform for Adaptive opticS System (COMPASS, Gratadour et al., 2014) has been used for the present study to perform SCAO simulations. COMPASS is a (partly) open-source end-to-end adaptive optics simulation platform built on a GPU architecture to enable long ELT-scale simulations within a reasonable computation time. At MPIA, a NVIDIA Tesla K40M general purpose

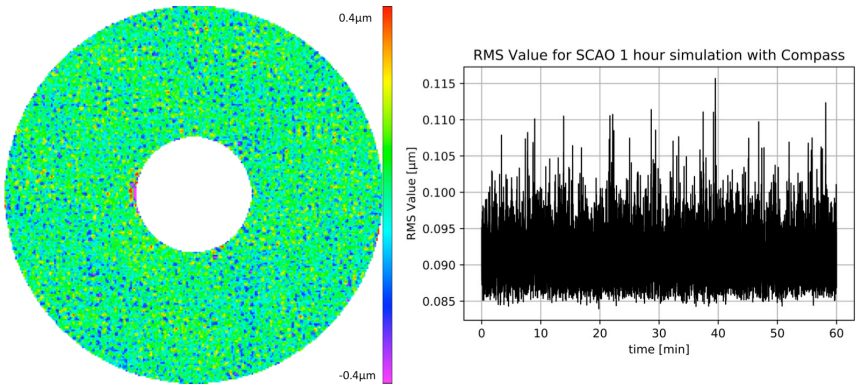

FIGURE 5.1: *Left*: AO residual phase screen. *Right*: RMS value for the SCAO simulation.

GPU has been installed, which makes it possible to simulate 10-min AO sequences with an image sampling of 592 pixels square in about 10 hours. The simulation parameters are summarized in Tab. 5.1. For the wavefront reconstruction, COMPASS uses a modal approach, the control matrix is computed via a least-square approach (truncated SVD where 79 modes are filtered-out when building the command matrix). For the simulations described here (used for the PDR design, in May 2019), a simple proportional-integral (PI) controller was used.

TABLE 5.1: SCAO baseline parameters used to run long-simulations with COMPASS.

Parameter	**Value**
Pupil diameter	37 m
Central obstruction	11.1 m
Spiders	none
Segmentation	none
Target star magnitude	5 (K-band)
Zenith angle	30°
Fried parameter @ 500nm	0.157 m
Outer scale	20m
Atmospheric layers	35
Wind direction	random for each layer
Coherence time @ 500nm	5.35 ms
Sensing wavelength	2.2 μm (K-band)
Number of subapertures along diameter	74
PyWFS modulation circle	$4\lambda/D$, sampled in 24 points
Wavefront sensor throughput	0.327
WF slope calculation	Vérinaud, 2004
Controller	Integrator
HODM ELT/M4 type	piezo-stack array (Gaussian influence functions)
TTDM ELT/M5	yes
Loop frequency	1000 Hz
Total frame delay	2
Loop gain	0.4
Sampling	592 pixels across aperture (= 6.25 cm/pixel)

TABLE 5.2: Main parameters for the optical propagation simulations.

Band	L & M	N
Wavelengths	3.8 & 4.8 μm	8.7 & 11.5 μm
Grid size	1024×1024 px	1024×1024 px
Pixel size	5.21 mas	10.78 mas [1]

For the purpose of the HCI performance tests, a series of 10-min AO sequences, as well as a 1-h long AO sequence have been produced. For each simulation sequence, first the simulation is run for 1s without recording the residual phase in order to make sure the AO loop is closed before recording the residual phase screens (1 phase screen every 100ms). Besides atmospheric turbulence, no other temporally variable effects, such as vibrations, varying NCPAs or observing conditions, have been added. Note that the wind direction is assumed to be random in all atmospheric layers. This is an optimistic assumption, which reduces the strength of the wind-driven halo in AO-corrected images. Correlation between wind direction in various layers has not been studied in this manuscript (a more realistic wind profile was implemented after PDR).

All simulations are performed on a circularized version of the ELT pupil, corresponding to the all-glass pupil of $\sim$ 37 m diameter. Spider arms were not included in the SCAO simulations in order to remove any residual piston effect between the six ELT petals. This effect will be studied separately in Sect. 6.2.5. A representative phase screen, as well as the evolution of the standard deviation of the residual phase across the pupil, are displayed in Fig. 5.1.

5.1.2 Optical propagation

The optical propagation inside the instrument is performed using a custom python package referred to as HEEPS, which relies on the PROPER (Krist, 2007) optical propagation library. The PROPER library contains routines of optical propagation in the near-field and far-field conditions, using Fourier transform algorithms (Fresnel approximation). The propagating wavefront is described by its amplitude and its phase. A perfectly collimated beam will present a planar surface for the constant phase, while passing through a lens will modify it into a curve. In order to avoid aliasing problems due to the representation of this curved phase surface into a planar sampled grid, the phase is actually considered as a phase error relative to a sphere with known radius of curvature.

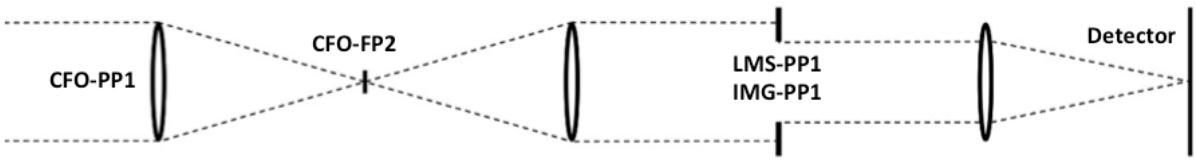

FIGURE 5.2: Simplified scheme of the METIS high-contrast imaging instrumental setup, used in the simulations.

[1] This pixelsize corresponds to the AQUARIUS detector, which was the baseline at the PDR. It has been replaced by the GEOSNAP detector.

The implemented propagation layout is very simple, as it includes only the pupil planes and focal planes where HCI elements are placed inside METIS (see Fig. 5.2). The input pupil of the coronagraph, defined by the ELT-M1 mirror, is re-imaged at the CFO-PP1 pupil plane, where a ring apodizer can be inserted. CFO-FP2 is the focal plane where the vortex phase masks can be inserted. The Lyot stops and APPs are included inside the imager and spectrograph, at pupil planes referred to as LMS-PP1, IMG-LM-PP1, and IMG-N-PP1. The two pupil planes inside the imagers will be referred to as IMG-PP1 for convenience, although they are physically distinct. Finally, the coronagraphic image is formed onto the detector, the second focal plane included in the simulations. The main simulation parameters are listed in Tab. 5.2. Here, we will mostly focus on L-band simulations, because they are more affected by instrumental errors. We also include simulations in the M and N bands to illustrate how the thermal background limits the sensitivity at longer wavelengths.

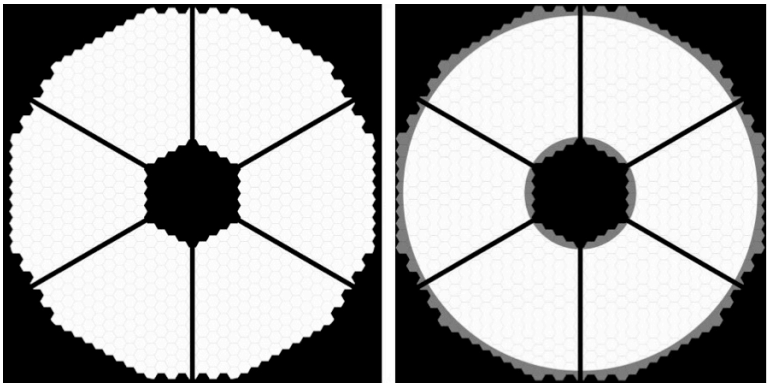

FIGURE 5.3: *Left*: Geometrical description of ELT-M1, including spider arms. *Right*: Inscribed circular (all-glass) pupil used for the performance analysis.

The ELT primary mirror (M1) contains 798 quasi-hexagonal segments, 1.45 m from side to side, with 4 mm gaps between them (see Fig. 5.3, left). Six 60 cm-wide spider arms divide the pupil into six sectors, or *petals*. The pupil used for the simulations is the circular pupil inscribed in the ELT pupil (aka the all-glass pupil), with an external diameter of 37 m and an internal one of 11.1 m (30% central obstruction).

The optical propagation simulation produces noiseless coronagraphic PSFs for each residual AO screen, creating a cube of 36000 coronagraphic PSFs for a 1h sequence sampled every 100ms. In Chapt. 6, instrumental errors within the optical propagation prescription, such as pointing errors, pupil alignment errors, or differential piston between the ELT-M1 petals are added. All simulations are performed at a single wavelength, but will be considered as representative of broadband observations. This inherently neglects all chromatic errors, and in particular the effect of atmospheric dispersion in the Earth atmosphere. The simulations are therefore more representative of narrow-band observations, even though it can be assumed here that such performance can be preserved in the broadband METIS filters defined in Tab. 5.3.

HEEPS

HEEPS is written in the open-source Python language. The architecture is illustrated in Fig. 5.4.

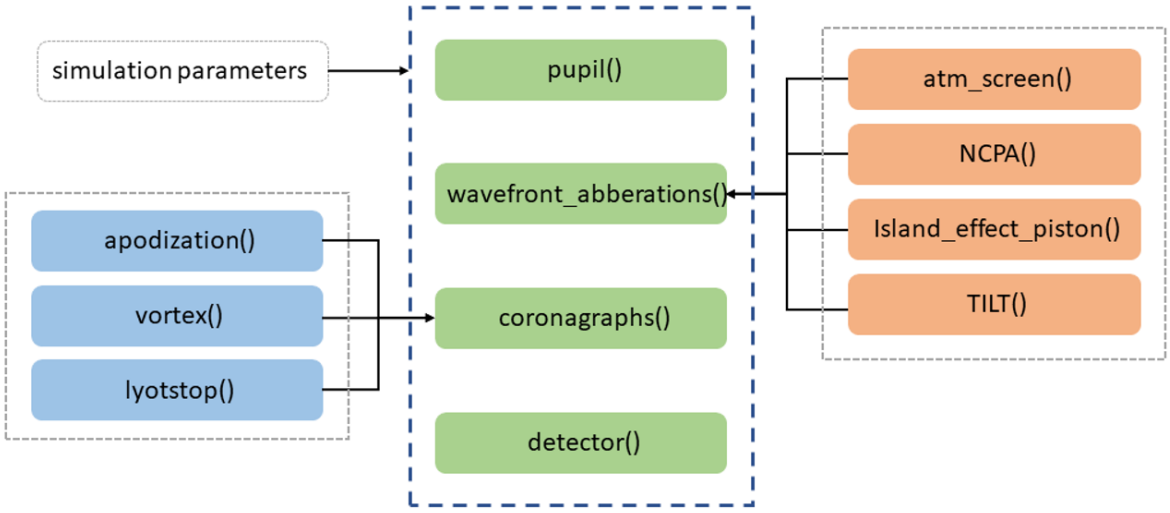

FIGURE 5.4: Architecture of the HEEPS package.

The simulation parameters (as the width and the position of the spiders or the wavelength of the simulation) are loaded through the file *simulation_config.py* and they can be updated while running the simulation. This file also creates the directories *temp_files* and *output_files*, where the calibration files and the results are stored, and the directory *input_files*, where the fits files (as the pupil or the APP apodizer), downloaded by the file *simulation_config.py*, are stored.
The HEEPS package simulates the end-to-end optical propagation, following Fig. 5.2. The *pupil()* module creates the pupil of the telescope, by importing a grey scale hexagonal pupil (see Fig. 5.3). Misaligned segments can be defined here (9 options are possible, following the number and the distribution of the misaligned segments). The *wavefront_abberations()* module modifies the wavefronts, by applying the input aberrations, as the atmospheric residuals (via the *atmosphere* module), the NCPA (via the *NCPA_application* module), the differential piston (Island Effect, via the *island_effect_piston* module) to the 6 petals, and the pointing tilt.
Through the *apodization* function, the *coronagraph()* module allows to apply apodizers (phase or amplitude) to the first pupil plane (and define its misalignment, if needed), while the function *lyotstop* can specify an apodizer (phase or amplitude) of the second pupil plane (as for the *LPM* coronagraphic option, see Sect. 8.2.3), together with its misalignment.
The *coronagraphs()* module applies the coronagraph to the wavefront. Several options are possible:

- LS: Lyot Stop. Mostly in combination with other coronagraphs, this option creates an amplitude stop at the second pupil plane (via the function *lyotstop*). Its default characteristics are the ones for the charge 2 vortex coronagraph.
- CVC: Classical Vortex Coronagraph. This option introduces a vortex phase mask at the first focal plane (via the function *vortex*), followed by its Lyot stop. The default charge is 2, however higher charges can be implemented.

- RAVC: Ring Apodized Vortex Coronagraph. This option creates an apodized vortex coronagraph; by default, it is a charge 2 coronagraph. It first applies the apodization mask at the first pupil plane (via the function *apodization*), then it creates a charge 2 vortex phase mask, with an optimized Lyot stop (its characteristics are implemented by default for a charge 2 vortex coronagraph).
- PAVC: Polynomial Apodized Vortex Coronagraph. This option creates an apodized vortex coronagraph, with a slightly different apodization function with respect to the RAVC (see Sect. 8.2.2). As for the latter, the vortex and the Lyot stop are created accordingly. The default options are two: a charge 4 and a charge 6 vortex coronagraphs.
- DV: Double Vortex. This option applies a double charge 2 vortex coronagraph (Mawet et al., 2011).
- Apodizer. This option applies a pupil apodization to the first pupil plane (via the function *apodization*).

The *detector()* module propagates the beam up to the detector plane (second focal plane), saving the PSF in a fits file.
The RAVC apodization is computed mathematically (see Sect. 4.5.2), while for the PAVC, the APP and the LPM, a fits file is uploaded with the relative apodization, which was previously optimized.
In order to simulate the full SCAO sequence (a few thousands phase screens), multiple CPUs can be used via the multiprocessing Python library.

5.1.3 Mock observations and post-processing

In order to turn the noiseless coronagraphic PSFs into a realistic observing sequence, the main observing parameters need to be defined. We assume a standard HCI observing sequence with a bright, early-type star ($K = 5$, $L = 5$) observed for one hour around meridian crossing, and culminating at a minimal zenithal distance of 20°. This observing sequence provides a total rotation of the parallactic angle of about 35°, and would correspond more or less to the case of 51 Eri observed from the ELT site. Note that the variation of airmass during the observation is not captured in the AO simulation. This is not expected to be a strong contributor to the HCI performance, as the zenith angle varies only by one degree during the whole observing sequence. At N band, a very bright star similar to Alpha Centauri ($N = -1.6$) is assumed, while keeping the rest of the observation parameters.

TABLE 5.3: Filter definition, total stellar flux for $L = M = N = 5$, and background flux per pixel (source: METIS simulator, SimMETIS, version 02, `metis.strw.leidenuniv.nl/simmetis`).

	Filter	Wavelength [μm]	50% width [μm]	Stellar flux [e$^-$/sec]	Background flux [e$^-$/sec/px]
L band	HCI-L long	3.82	0.27	9.00×10^8	8.88×10^4
M band	CO ref	4.80	0.22	2.45×10^8	6.71×10^5
N band	N1	8.65	1.17	2.98×10^8	9.63×10^7
N band	N2	11.25	2.34	2.82×10^8	2.14×10^8

Once the observing sequence is defined, producing a realistic mock observation requires to scale the noiseless coronagraphic PSFs produced above to the actual stellar flux in photo-electrons, to add the emission from the thermal infrared background, and to include the effect of the main noise sources. It is then converted into ADU, taking into account the inputs from the METIS simulator (R. van Boekel, pers. comm., see Tab. 5.3) and assuming a target star of magnitude $L = M = 5$, or $N = -1.6$. The background is then added, and finally random shot noise is generated, independently on each pixel. Classical ADI processing (see Sect. 2.3.1, Marois et al., 2006) is used to process the mock data cubes, using the open source package VIP (Gomez Gonzalez et al., 2017). The main metric used in this thesis to evaluate METIS HCI performance is the post-processed 5σ contrast (Mawet et al., 2014). The noise level in the final image is computed at a given angular separation from the star as the standard deviation of the aperture fluxes measured in as many independent resolution elements as can be defined at that separation. In order to evaluate the sensitivity limit of the instrument in terms of contrast, this noise level must then be compared to the non-coronagraphic signal of the host star, taking into account the throughput of the post-processing algorithm. This throughput is evaluated by injecting fake companions at various positions into the raw data and by applying the same post-processing algorithm to measure the amount of signal preserved in the final post-processed image. The formula defining the 5σ contrast is the following:

$$c = \frac{5N}{\tau S} \tag{5.1}$$

where N is the noise, S the non-coronagraphic stellar signal measured in an aperture of size equal to one resolution element (λ/D), and τ the algorithm throughput. Note that the factor 5 is associated with a fixed false alarm probability (3×10^{-7}) for purely Gaussian noise. The small number of samples at short angular separations modifies the relation between false alarm probability and noise level (Mawet et al., 2014). In order to keep the same false alarm probability at all separations, this requires to modify the definition of contrast, taking into account a t-Student distribution instead of a standard Gaussian distribution. A two-sample t-test is used to see whether the intensity of a given resolution element is statistically different from the flux of similar λ/D circular apertures at the same radius r from the star. This penalty associated to small sample statistics is taken into account in all contrast curves presented in this thesis.

A second contrast-related metric useful to evaluate the HCI performance is the raw contrast, which is defined, at any given separation, as the ratio between the intensity of the considered PSF (be it coronagraphic or not) and the peak of the off-axis PSF with the same METIS configuration (Lyot stop, apodizer, etc). It indicates the mean level of residual starlight at a given separation. Raw constrast can readily be assessed by plotting the PSF profile of interest in a figure where the direct PSF profile culminates at 1 on the optical axis. This metrics does not tell what is the faintest source that can be detected, as it is not a direct indicator of noise level. Yet, raw contrast can be useful to assess a coronagraph's capability to cancel stellar light. In the case of the APP, this estimation is done on the clean half of the field-of-view.

5.2 SCAO simulation setup

5.2.1 Duration and sampling of the AO sequence

Before presenting the nominal HCI performance, it is important to study how the duration and time sampling of the AO residual phase screen sequence affects the estimated performance, in order to come up with a baseline set of AO simulation parameters that provide robust performance estimation within a reasonable computation time. All simulations performed in this section are done for a RAVC operating at L band, because it is supposed to be the best performing HCI mode, on which the influence of the AO sequence can most readily be assessed. To reduce computation time, the field-of-view is generally cropped to a radius of about 0"6, which produces individual frames of about 240×240 pixels based on the sampling of 5.21 mas/pixel for the LM-band images detector. Background noise or photon noise are not included here to highlight the effect of pure speckle noise. As shown later in figures 6.2, 6.3, 6.4, and 6.5, the background noise creates a plateau at larger angular separations, drowning the coronagraphic signal. On the contrary, since the degradation at smaller angular separation is less significant, including the background and photon noise would prevent from discriminating the effects that have more detrimental consequence on the contrast.
Ideally, it would be logical to use a 1-h SCAO simulation, to match the typical duration of an ADI observing sequence, with a sampling down to a few tens of msec to properly capture the evolution of atmospheric turbulence in the thermal infrared, where the atmospheric coherence time τ_0 ranges from a few tens of msec to a few hundred of msec depending on weather conditions and wavelength. A 10-msec sampling would however result in 360,000 phase screens for each individual end-to-end simulation, which is not acceptable in terms of computation time. In order to perform a parametric study of the SCAO and of the instrumental noise sources within a reasonable time, the computation time associated with one single end-to-end simulation has to be reduced. The influence of the duration and sampling of SCAO simulations on the ADI contrast curves is therefore investigated.

5.2.1.1 Duration

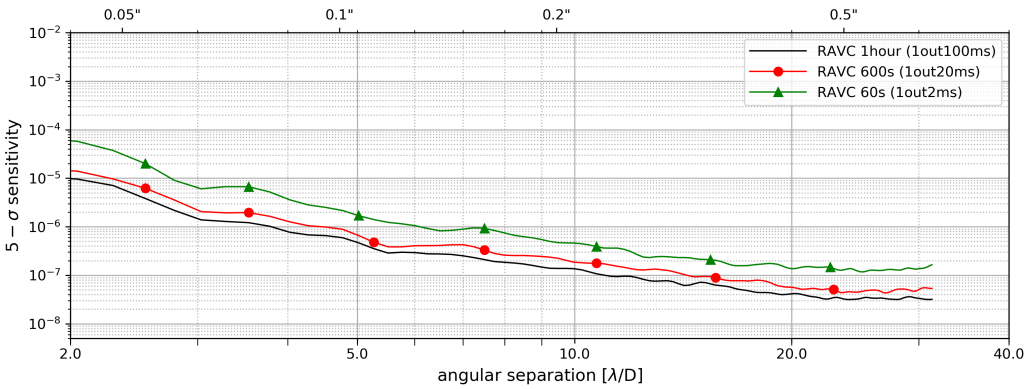

FIGURE 5.5: Comparison of contrast curves obtained for the RAVC at L band with three SCAO sequences of different duration and sampling: 1 h with 100 msec sampling (black), 10 min with 20 msec sampling (red), and 1 min with 2 msec sampling (green).

Assuming a 1-h long simulation as a baseline, the best sampling that can be used while maintaining a reasonable CPU time and a reasonable RAM usage is about 100 msec, which gives a total of 36,000 phase screens. The computation time is then around one day for the SCAO simulation on the MPIA GPU server, about 10 h for the optical propagation on a multi-core CPU server, and a couple of hours for the contrast curve computation. The RAM usage for the optical propagation and contrast curve computation can be kept below the 128 Gb available on the CPU server.

In order to investigate the effect of the SCAO sequence duration, two other sequences are produced, respectively 1-min and 10-min long, with a similar number of phase screens. For that, a sampling of 2 msec in the first case, and 20 msec in the second case, are used, which results in 30,000 phase screens in both cases. In terms of optical propagation and contrast curve computation, the advantage is negligible, since only the number of phase screens has an impact on them (from 36,000 to 30,000 phase screens). In order to simulate a 1-h long ADI sequence based on these two shorter SCAO sequences, they are artificially stretched in time, so that the time between samples becomes 120 msec instead of 2 or 20 msec. All three sequences are then post-processed with the same classical ADI algorithm to produce contrast curves. This is illustrated in Fig. 5.5, where one can note that using the 10-min sequence results in a degradation of the contrast by less than a factor 2. Conversely, going to a 1-min sequence results in a very significant degradation of the contrast, by a factor around 5. Stretching a SCAO sequence does not preserve the timescale of correlation between successive phase screens (or equivalently, the shape of the temporal PSD), and so also between the associated coronagraphic PSFs, degrading the contrast as the SCAO sequence is shortened. It is well known that the performance of ADI post-processing techniques largely depends on the level of temporal correlation between individual PSFs.
The conclusion of this comparison is that, while 1-h long sequences should ideally be used to assess HCI performance, using 10-min sequences can also be tolerated in cases where the computation time for the SCAO simulation becomes prohibitively large. In particular, testing various SCAO configurations/parameters with 1-h long sequences is impractical, and will generally be restricted to 10-min long sequences.

5.2.1.2 Sampling

Reducing the number of phase screens decreases the computation time for the optical propagation and contrast curve calculation. For that, the two longest SCAO simulations are chosen, respectively spanning 10 min with a sampling of 20 msec, and spanning 1 h with a sampling of 100 msec. In Fig. 5.6, one can see how the final post-processed contrast is affected when down-sampling these series of phase screens in the time domain. From the 10-min simulation (top), it can be observed that down-sampling to one phase screen every 100 msec still produces an acceptable result in terms of contrast level (degradation by less than a factor 2). This seems to be in line with a coherence time of up to about 100 msec at L band. The 1-h simulation (bottom) confirms that a coarser sampling than 100 msec starts to take a significant toll on the estimated performance, although one can note that the 300 msec sampling on the 1-h sequence provides a final contrast similar to the 10-min sequence with 20 msec sampling, due to the improved contrast obtained by going from a 10-min to a 1-h sequence. The degradation in performance associated with a down-sampling from 100 msec to 300 msec is still generally not larger than a factor 2, which is considered acceptable.

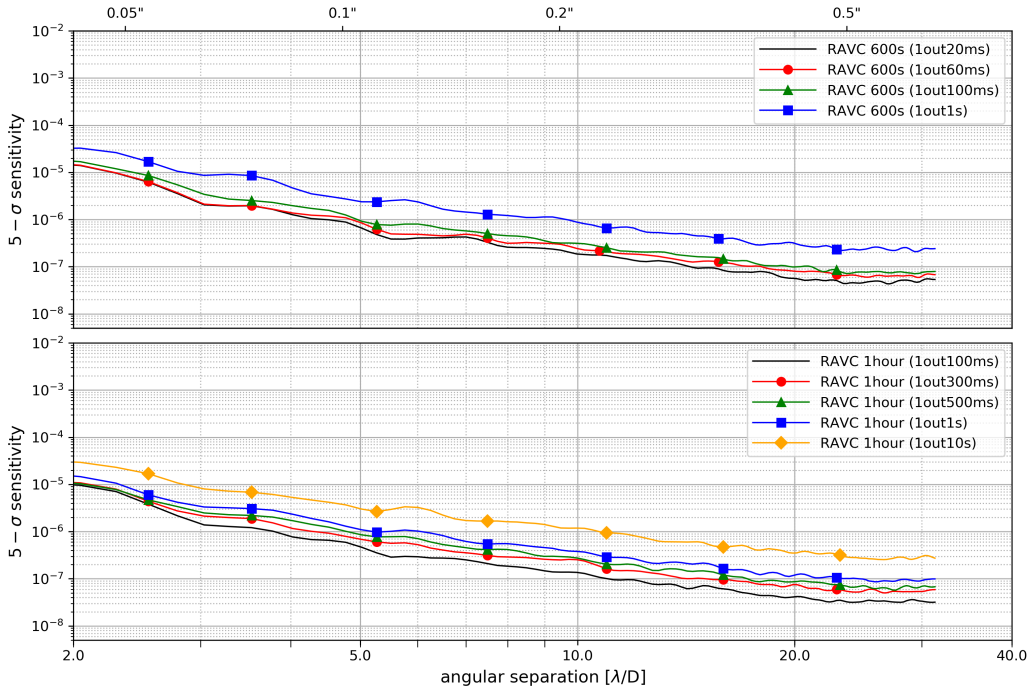

FIGURE 5.6: Comparison of contrast curves obtained with the RAVC at L band with various sampling times for two SCAO sequences, respectively 10-min long (top) and 1-h long (bottom).

In conclusion, in order to reduce the required computation time, either a 1-h long sequence with 300 msec sampling (12,000 phase screens, 4hours for the optical propagation and a couple of hours for the contrast curve calculation), or a 10-min long sequence with 100 msec sampling (6,000 phase screens, 1hour for the optical propagation and half an hour for the contrast curve calculation) will be used. The former will only be used to study instrumental effects that do not require to produce new SCAO simulations (i.e., effects associated with the coronagraphs), while the latter will be used to explore the influence of SCAO performance (the computation time goes from a day for the 1-hour sequence to few hours for the 10-min one).

Chapter 6

METIS performance

The end-to-end performance simulations of the METIS instrument are presented in this chapter. Firstly, a nominal performance is established, by considering only the SCAO residual phase screens and the thermal background noise, and considering the instrument otherwise perfect. We then use this nominal performance as reference to compare instrumental and environmental effects applied to the instrument, as pointing jitter or non-common path aberrations. This chapter is based on previous work published in Carlomagno et al., 2020.

6.1 Nominal HCI performance in presence of AO residuals

6.1.1 L-band performance

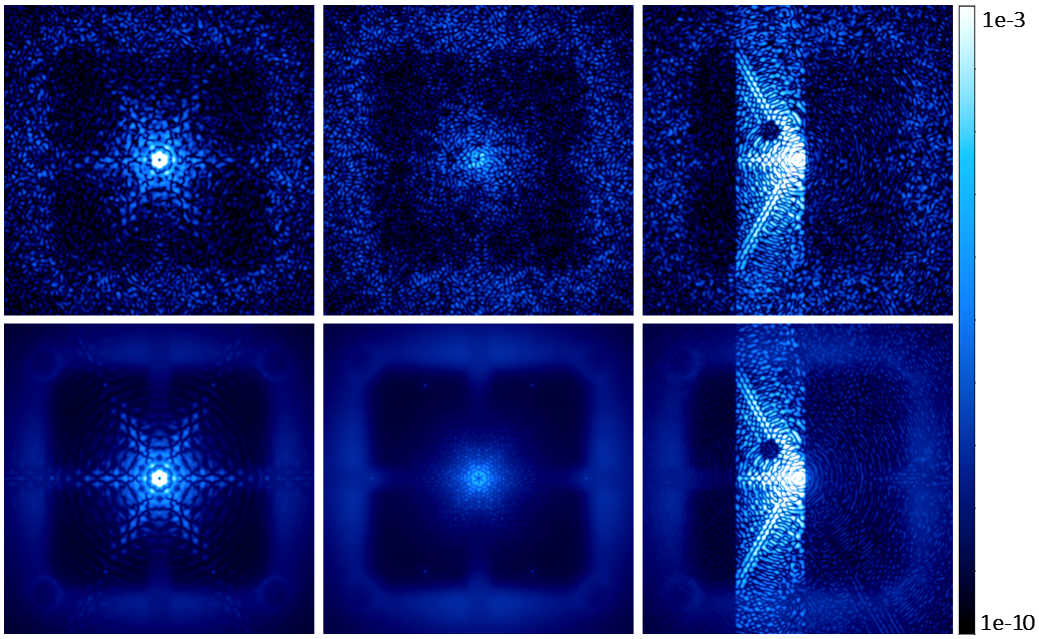

FIGURE 6.1: *Top.* Representative instantaneous (300 msec exposure time) PSFs at L band, using a single SCAO residual phase screen, obtained in the case of CVC (left), RAVC (center), and APP (right). *Bottom.* Same for long-exposure (1 hour exposure time) PSFs. All images have been cropped to a field-of-view of $100\lambda/D$, i.e., 2"1 at L band.

Using the 1-h SCAO sequence with 300-msec sampling, a first set of simulations is performed at L band (central wavelength of 3.8 μm) for the three main coronagraphic concepts considered for METIS: the CVC, the RAVC, and the APP (using

the PDR version of the APP design). In Fig. 6.1, one can see the representative instantaneous PSFs for the three coronagraphic concepts, as well as the long-term PSF, averaged over the full 1-h sequence. This figure clearly highlights the well-corrected region corresponding to the spatial frequencies that can be controlled by the ELT deformable mirror (about $80\lambda/D$ across). It also highlights the amount of starlight remaining in the science focal plane, ranging from full stellar light in the case of the APP, to very low starlight for the RAVC. The mean total stellar leakage for the CVC and RAVC in presence of AO residuals are respectively around 8% and 3%. These figures are due to the combination of diffraction in the telescope and atmospheric turbulence. In the absence of any perturbation, the total stellar leakage for these two configurations, due exclusively to diffraction effects associated to the shape of the input pupil (and to the Lyot stop design), would amount to 3% (CVC) and 0.2% (RAVC). The level of residual starlight should also be compared with other fundamental contributors to the total stellar leakage, such as the chromaticity of the vortex phase mask (total leakage around 0.1%), the influence of atmospheric dispersion (total leakage below 1% on HCI-compliant filters), or the influence of partially resolved stellar surfaces (total leakage of 4% for α Cen A, one of the worst cases for METIS HCI). The results presented here are valid for sufficiently low air masses–or equivalently for sufficiently narrow filters (bandwidth generally smaller than 10%)–, and for sufficiently compact stars (angular diameter smaller than 4 mas at L band), in which cases the effect of atmospheric dispersion and of partly resolved stellar surfaces is reduced below the level of stellar leakage associated to pure atmospheric turbulence.

The raw PSF profiles (a.k.a. *raw contrast*) and the 5σ sensitivity limits in terms of flux ratio after ADI post-processing (a.k.a. *contrast curves*) are displayed in Fig. 6.2. In the case of the APP, the raw and post-processed contrasts were computed by combining the dark holes associated to the two coronagraphic PSFs of the grating-vector APP. This leaves in principle a bright stripe of speckles in between the two dark holes. Here, this bright stripe was artificially dimmed to facilitate the contrast computation. The contrast curves for the APP are thus somewhat optimistic, especially at the shortest separations where the bright stripe has the largest relative influence. It can be noted that the RAVC, CVC, and APP meet the goal of 3×10^{-6} contrast at $5\lambda/D$.

The non-coronagraphic mode was not included in these curves, because very detrimental effects could not be taken into account in the simulations. These effects, as straylight and detector saturation effects, significantly limit the discovery space at small angular separations from bright stars in the non-coronagraphic case.

It is noteworthy that the sensitivity limits become dominated by thermal background noise beyond about 0"3 (or even 0"2 for the RAVC), for the stellar magnitude $L = 5$ considered here. Further simulations show that, for $L = 8$, the transition between the speckle-dominated and the background-dominated regimes shifts to about 0"1 (i.e., $5\lambda/D$). Using a coronagraph for fainter targets becomes less and less useful. The APP sensitivity takes into account the fact that the planetary signal is divided into two conjugated PSFs by the phase plate, and that its Strehl ratio is reduced by the redistribution of the light required to create a dark hole. The background-limited sensitivity of the APP is therefore similar to the RAVC's. The CVC provides the best sensitivity limits in the background-limited regime (very close to the non-coronagraphic sensitivity limit), thanks to its high throughput.

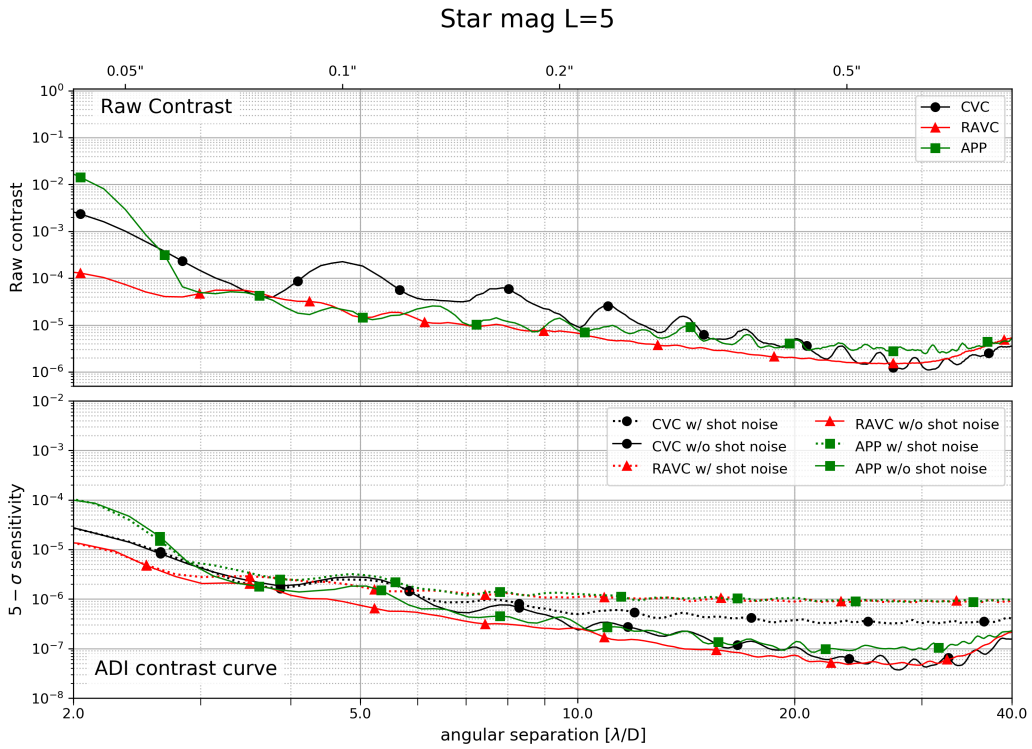

FIGURE 6.2: Raw contrast (top) and ADI contrast curve (bottom) for RAVC, CVC, and APP observing modes at L band. In the bottom plot, the solid curves include only the contribution of speckle noise, while the dashed curves include the effect of the thermal background (shot noise) for a star of magnitude $L = 5$.

6.1.2 M-band performance

The same analysis as in L band is carried out at M band in Fig. 6.3. The raw contrast shows a significant improvement compared to L band, because all phase errors have a smaller effect at longer wavelengths. The ADI contrast curves computed in the absence of thermal background and photon noise improve accordingly. However, in presence of thermal background and photon noise, the performance is largely decreased, due to the higher background level at M band. This also means that the RAVC becomes less useful at this wavelength, and will only be used for stars significantly brighter than $M = 5$.

6.1.3 N-band performance

Because of the large thermal background, coronagraphy at N band will only be useful for the brightest stars. Here, it is presented only the case of α Cen A, with magnitudes $K = -1.5$, $N = -1.6$. For the sake of simplicity, the same set of SCAO residual phase screens as described in Sect. 5.2 are kept, recognizing that photon noise is not dominant for stellar magnitudes $K \leqslant 5$, so that one cannot expect a significant improvement in terms of SCAO residuals compared to the case presented in Sect. 5.2. We also kept the same trajectory in the sky as in the previous section, although it is recognized that a 1-h observing sequence on α Cen would actually lead to a parallactic angle variation of only about 23° (instead of 40°).

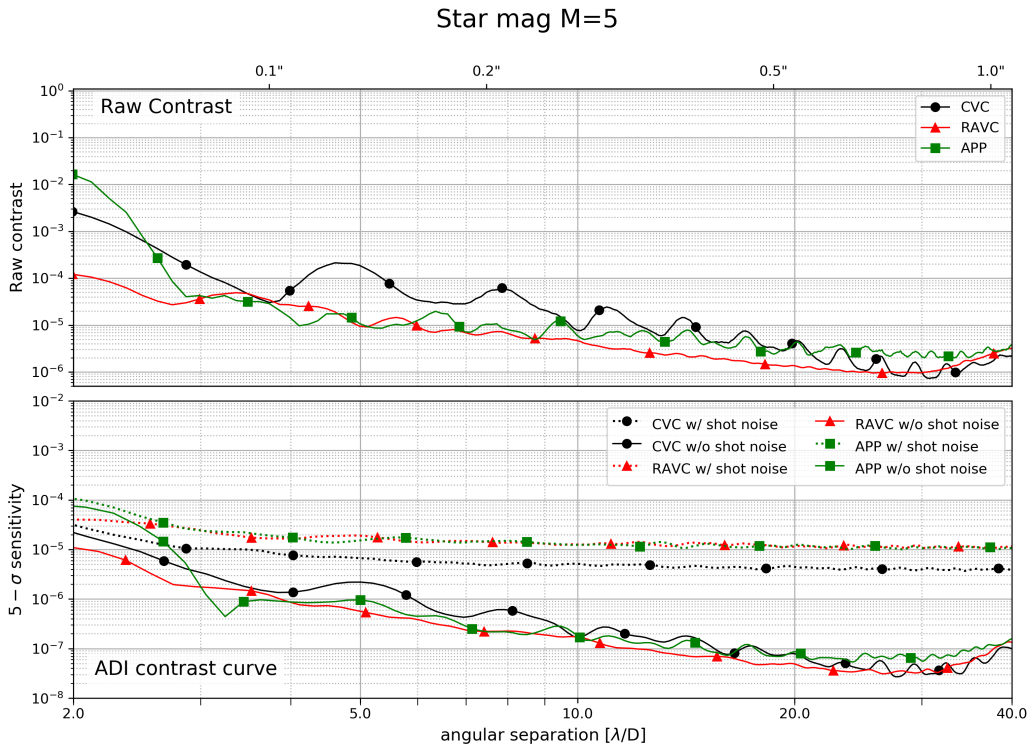

FIGURE 6.3: Same as Fig. 6.2 for M band, in the case of a star of magnitude $M = 5$.

The sensitivity limits at 8.7 μm (aka N1 band) and 11.5 μm (aka N2 band) are displayed for α Cen A in Figs. 6.4 and 6.5. They show that, even for one of the brightest stars in the sky, the performance is background limited for angular separations larger than about 0"5. Because the RAVC largely decreases the total throughput, this mode is not considered at N band. Indeed, additional simulations show that, even for a bright star like α Cen, the RAVC would improve HCI performance only within about 0"1. A simple CVC is preferred at N band to provide the highest possible throughput, while still reducing the total amount of stellar light from the host star by a factor $\sim$30, and the peak intensity in any pixel by a factor slightly larger than 100.

6.2 Influence of individual contributions

Most of the instrumental and environmental parameters of the SCAO system have a direct influence on HCI performance. Some important effects at SCAO level are described in the following sub-sections, such as residual pointing jitter (Sect. 6.2.4), and petal piston (Sect. 6.2.5).

Here, and for the rest of this thesis, L-band simulations at 3.8 μm are considered as baseline to explore the influence of instrumental and environmental error sources and quantify their effect on HCI performance. The reason for using the L band is that on one hand, the contrast requirement for METIS is defined at L band, and on the other hand, instrumental effects are supposed to have the highest relative influence at the shortest wavelengths. We will focus on the RAVC mode, which shows the best performance in the speckle-dominated regime, and is also therefore

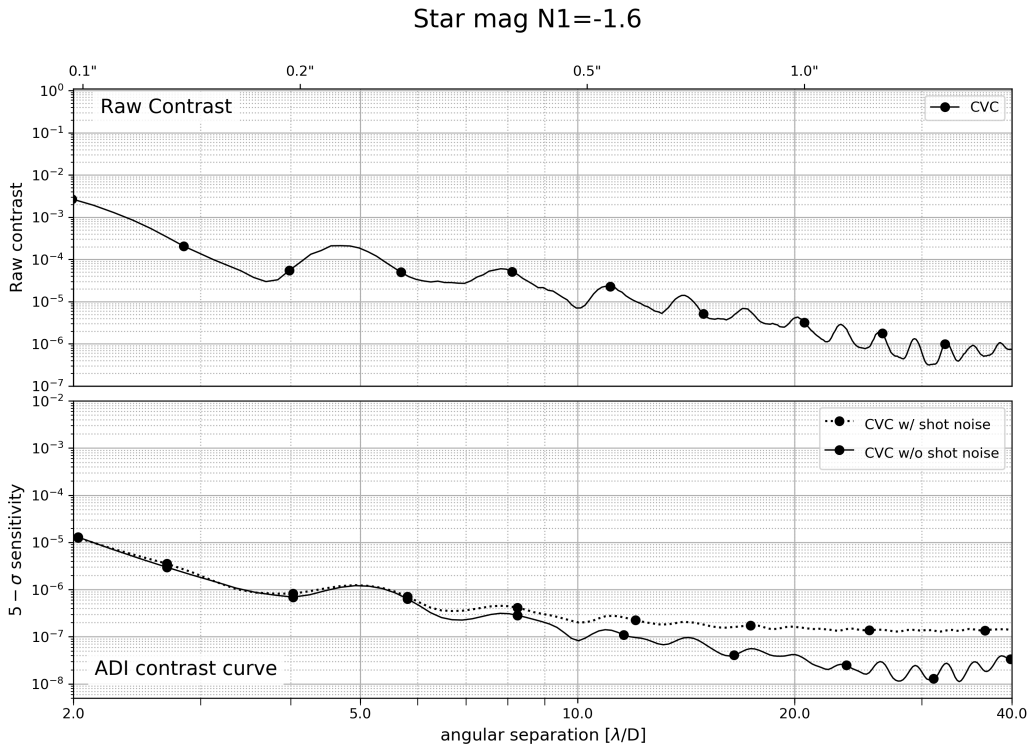

FIGURE 6.4: Same as Fig. 6.2 for N1 band (around 8.7 μm), in the case of a star of magnitude $N = -1.6$.

expected to show the strongest (relative) dependence on instrumental errors. All contrast curves from now on do not include the influence of the thermal background, as the speckle-limited contrast is considered important here. Adding the effect of thermal background would only conceal the effects that we aim to evaluate. When discussing the performance of HCI modes, one should have in mind that a large part of the search region will actually be background-dominated for most stars. The need for reaching very deep contrasts in these regions will be weighted accordingly.

6.2.1 Strength of atmospheric turbulence

One of the main parameters influencing the SCAO performance is the strength of atmospheric turbulence. Here, the influence of the Fried parameter r_0, or equivalently of the seeing, is presented. Fig. 6.6 presents the ADI post-processed contrast for a series of 10-min COMPASS simulations obtained under various seeing conditions ranging from excellent (0"45) to poor (0"95). While seeing has a significant influence on HCI performance, one can see that performance at small separations is weakly affected. Even the worst seeing explored here does not break the self-defined requirement of 3×10^{-6} at $5\lambda/D$. This suggests that, provided that the SCAO loop remains robust under such conditions (which seems to be the case based on the COMPASS simulations), HCI observations could in principle be carried out most of the time with METIS at the ELT.

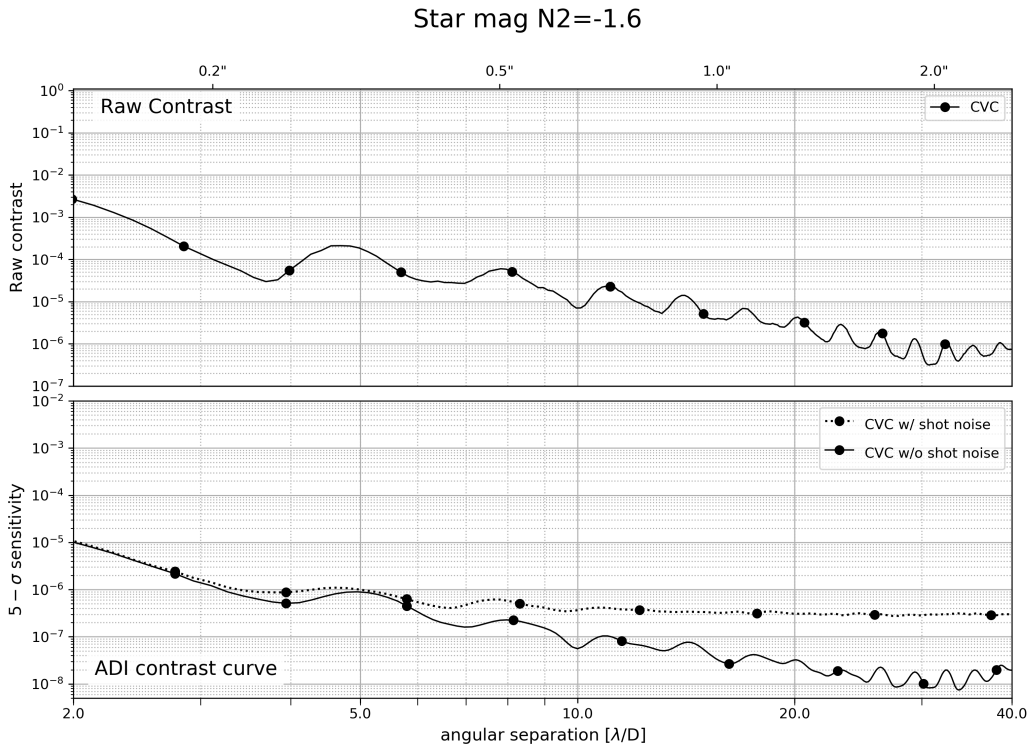

FIGURE 6.5: Same as Fig. 6.2 for N2 band (around 11.5 μm), in the case of a star of magnitude $N = -1.6$.

6.2.2 Pupil shape (misaligned segments)

The ELT pupil is not coronagraphy-friendly, due to the presence of a big central obstruction, secondary support structures, and segments. All these features have a large impact on HCI performance, all the more that the image of the ELT pupil is not stabilized in position and rotation at CFO-PP1, where the effects of diffraction could have been handled by advanced apodizer designs. Both APP and RAVC have been optimized to mitigate the effect of the 30% central obstruction, but the spiders still represent an important source of spurious diffracted light. This is particularly true for the vortex coronagraph, because the ring apodizer is located ahead of the derotator, so that it cannot be optimized to handle starlight diffracted by spider arms. Conversely, the APP has been optimized to take into account the effect of the spiders, because it is positioned after the derotator, in a pupil plane where the image of the ELT pupil is stabilized. The spiders have two effects: on one hand, they lead to additional diffracted stellar light inside the Lyot stop, and on the other hand, their own thermal emission increases the background emission if not properly masked by the cold Lyot stop. Thanks to the stabilization of the ELT pupil inside METIS, the image of the spiders can be masked at the Lyot stop / APP level with a reasonable level of oversizing: for 60-cm spiders in the ELT pupil plane (1.6% of the input pupil diameter), the spider width in the Lyot stop / APP plane amounts to about 3% of the pupil diameter (i.e., about 110 cm in the ELT pupil), taking also into account the effects of pupil blurring and shear.

Besides spiders, mirror segmentation can also lead to performance degradation. Segmentation itself creates spurious replica of the ELT PSF within the coronagraphic

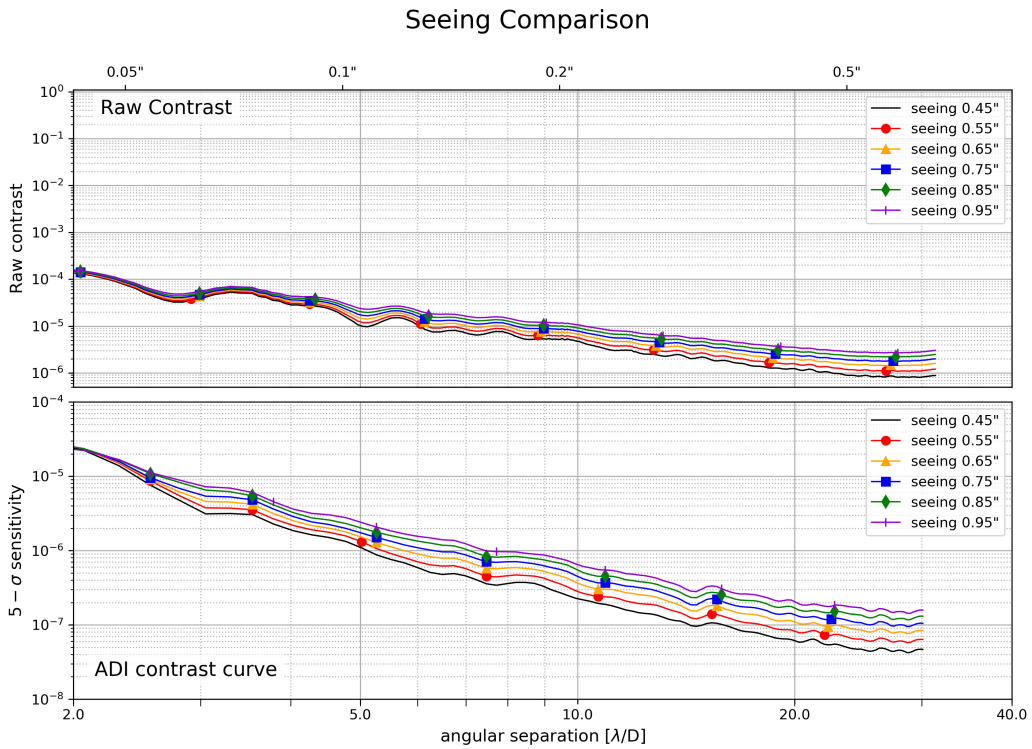

FIGURE 6.6: Raw contrast (top) and ADI post-processed contrast (bottom) for the RAVC at L band for various seeing conditions, considering only the contribution of AO residuals speckle noise (no photon noise considered here and in the next following figures).

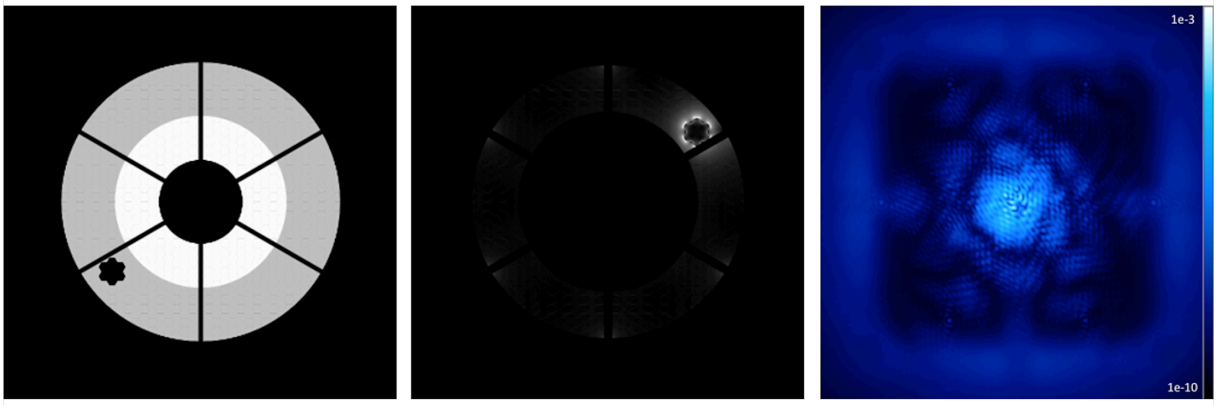

FIGURE 6.7: *Left*. Input pupil with 7 misaligned segments in flower configuration. *Middle.* Corresponding distribution of light in the Lyot stop plane for the RAVC. *Right.* Averaged noiseless coronagraphic PSF, in presence of atmospheric turbulence.

images. These aliases however appear at spatial frequencies higher than the frequencies that can be corrected by the M4 deformable mirror. They will therefore be located in a region where HCI performance is severely reduced, and are thus not considered as a critical issue here. The real problem with mirror segmentation

is that, during night-time operations, several mirror segments could be misaligned due to maintenance. The average number of misaligned segments will be no more than seven during the ELT lifetime. The most probable spatial distribution of missing segments is a flower pattern (i.e., seven neighboring segments, see Fig. 6.7, left) due to a failure within a segment concentrator. Because these misaligned segments may change from night to night, it is impossible to optimize the coronagraphs to compensate for them.

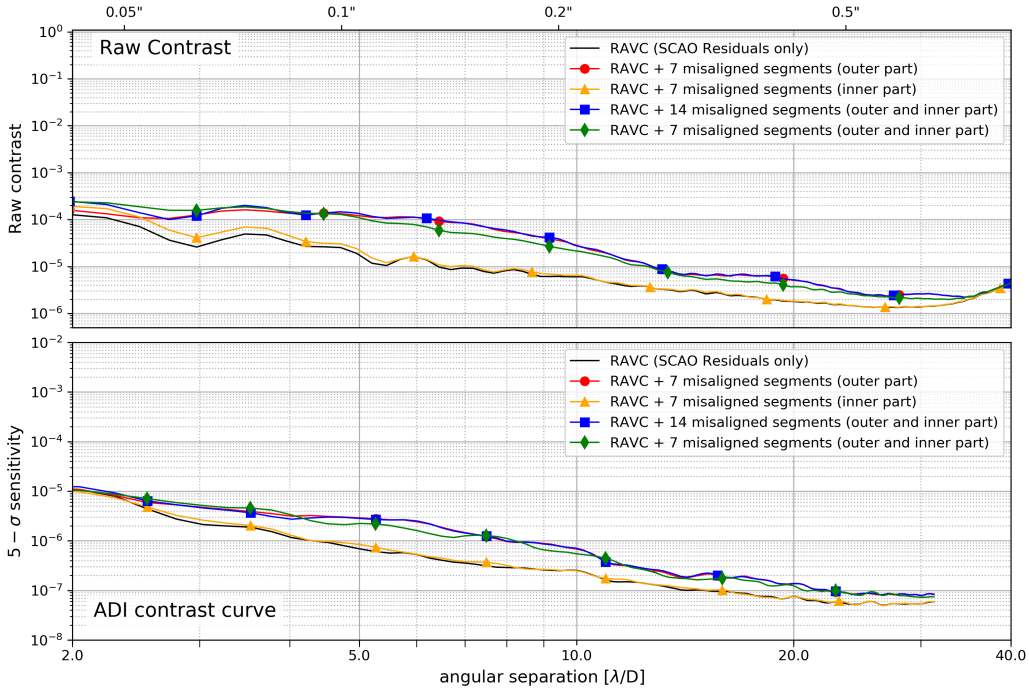

FIGURE 6.8: Raw contrast (top) and ADI post-processed contrast (bottom) for the RAVC at L band in presence of residual atmospheric turbulence for various configurations of misaligned segments in the ELT pupil, considering only the contribution of AO residuals speckle noise.

Assuming that the misaligned segments will be looking at an empty sky region, their net effect is to create a "hole" in the starlight intensity distribution in the input pupil. This hole will create additional diffracted starlight inside the coronagraph, leading to additional stellar leakage in the coronagraphic PSF (see Fig. 6.7).

Fig. 6.8 shows the contrast curves in presence of one or two sets of seven misaligned segments, arranged in a flower pattern. In this configuration, the effect of misaligned segments starts to show at angular separations larger than about $3\lambda/D$. At $5\lambda/D$, where the contrast requirement is defined, the ADI contrast is degraded by a factor around 5, in the case where one set of misaligned segments is located in the outer part of the pupil defined by the Lyot stop of the RAVC. While the ADI contrast performance is still compliant with the requirement (3×10^{-6}), it would clearly be preferable to operate the METIS HCI modes in the absence of misaligned segments. One can see that the presence of misaligned segments in the inner part of the pupil (blocked by the RAVC Lyot stop) does not significantly impact the RAVC performance.

6.2.3 Pupil stability

Thanks to the pupil stabilization mechanism, the ELT pupil will be stabilized inside METIS with a relative accuracy of about 1%. This stabilization however occurs downstream of CFO-PP1, where the ring apodizer will be installed. This means that the ring apodizer will be seen as drifting on top of the image of the ELT pupil, with an expected PtV amplitude of about 2.5%. Here, the effect of this drift, illustrated in Fig. 6.9, on the METIS HCI performance is investigated. The residual drift of the ELT pupil image downstream of the pupil stabilization mirror will be compensated by oversizing/undersizing the Lyot stop appropriately, and will therefore not contribute significantly to the stellar leakage level (but will reduce the overall throughput). Based on the expected stability of the ELT pupil with respect to METIS, the central obstruction in the Lyot stop has been further oversized by about 3%.

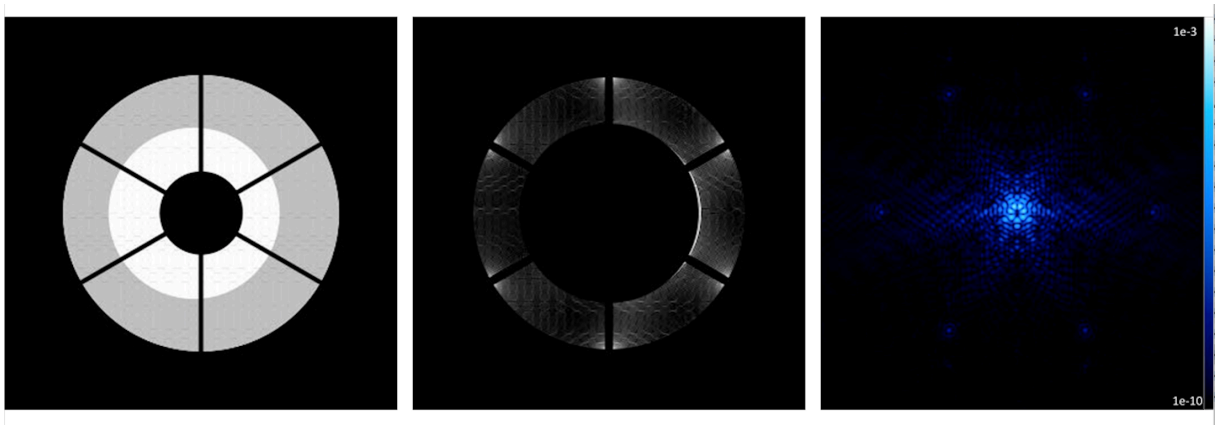

FIGURE 6.9: Effect of the ring apodizer misalignment on the RAVC behaviour. The misalignment has been exaggerated to 5% here for the sake of illustration. Illustration of the apodizer misalignment (left), intensity distribution at the Lyot plane, just after the Lyot stop (center), and associated coronagraphic PSF (right).

The effect of the misalignment of the ring apodizer with respect to the input pupil and Lyot stop is illustrated in Fig. 6.9. The additional amount of stellar leakage in the focal plane remains relatively low, as long as the footprint of the transition between the two zones in the apodizer remains hidden behind the central obscuration of the Lyot stop. To simulate the effect of drifts in the ELT pupil position during an HCI observing sequence, drifts with PtV amplitudes ranging from 1% to 5% of the M1 projected diameter have been injected in the optical propagation of the phase screens (see Fig. 6.10). In the simulations, the apodizer moves with respect to the ELT-M1 pupil image along the x axis, with a timescale equal to the duration of the ADI sequence. While the effect of this drift on the amount of stellar leakage is low, the effect on the ADI post-processed contrast is significant because of the deformations of the coronagraphic PSF associated to the changing intensity distribution in the input pupil. By assuming that the drift happens on the same timescale as the ADI observing sequence, a worst case scenario is here presented, as the variations in coronagraphic PSF shape will not average out sufficiently well on typically observing sequences using classical ADI processing. Under this hypothesis, a drift of 1% PtV would already be detrimental to the HCI performance at the shortest angular separations (see Fig. 6.10). Yet, we can tolerate a drift of the ELT pupil of up

to 3% PtV with respect to the CFO-PP1 pupil inside METIS before reaching the requirement in terms of post-processed contrast. This is compatible with the expected stability of the ELT pupil at the level of CFO-PP1.

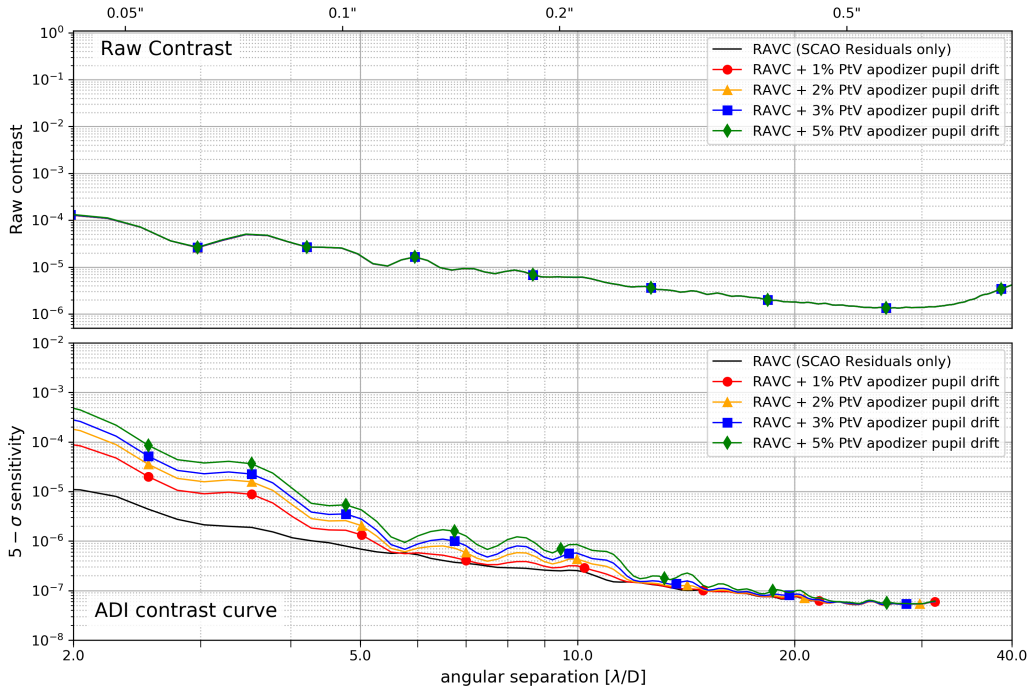

FIGURE 6.10: Raw contrast (top) and ADI post-processed contrast (bottom) for HCI performance for the RAVC at L band in presence of various PtV amplitudes of low-frequency drift in the alignment of the ring apodizer compared to the ELT pupil, considering only the contribution of AO residuals speckle noise.

Any pupil drift happening at higher temporal frequencies, including pupil jitter due to vibration, would have a smaller influence on the HCI performance than the low-frequency drift simulated here, because it would partly average out in ADI post-processing. The amplitude of pupil jitter is expected to be smaller than 1%, anyway, and will therefore not contribute significantly to the HCI performance budget.

It must be noted that, whatever their amplitude, drifts of the ELT pupil with respect to METIS are an effect on which there is almost no control. In case ELT pupil drifts turn out to be larger than anticipated, it could be possible to use more advanced post-processing techniques to (partly) mitigate this effect. For instance, ADI post-processing algorithms based on principal component analysis (Soummer et al., 2012, Amara et al., 2012) have been used, and it is possible to gain up to a factor two in terms of post-processed sensitivity at $5\lambda/D$, which would permit to work with pupil drifts larger than 5% PtV.

6.2.4 Pointing errors

Focal-plane phase mask coronagraphs, like the vortex coronagraph, are known to be particularly sensitive to low order aberrations, and to tip-tilt errors in particular (Mawet et al., 2010). Tip-tilt errors create additional leakage of stellar light through

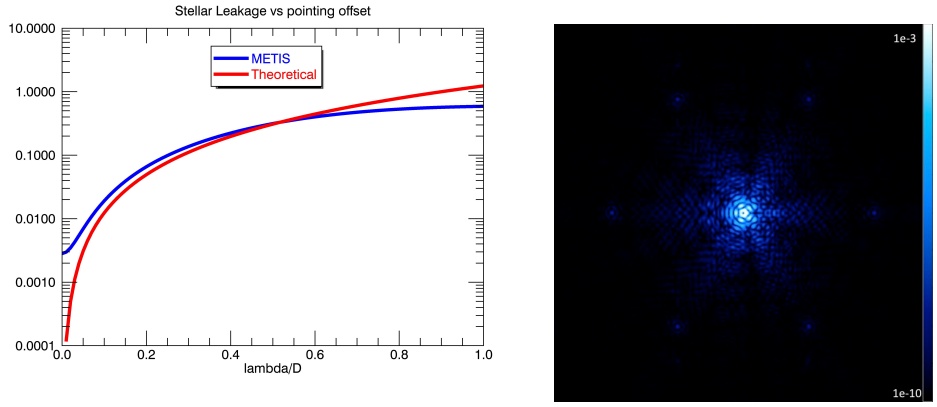

FIGURE 6.11: *Left.* Stellar leakage vs pointing offset for the RAVC on the ELT pupil, compared to the theoretical relationship for a CVC operating on a non-obstructed, circular pupil. *Right.* Coronagraphic PSF for a 1 mas pointing offset.

the Lyot stop, thereby reducing the achievable contrast. For a simple charge-2 vortex coronagraph, there is a square relationship between pointing error θ (expressed in units of λ/D) and stellar leakage η (Huby et al., 2015):

$$\eta = \frac{\pi^2}{8}\theta^2 \,. \tag{6.1}$$

In the case of the RAVC on the ELT pupil, an analytical relationship cannot be found, but simulations show that the dependency still mostly follows a square relationship close to the optical axis, as illustrated in Fig. 6.11, left.

Pointing errors can be divided into two main parts: high-frequency pointing jitter (typically > 1 Hz), and low-frequency pointing drifts (typically < 1 Hz). In the former case, random deviations from perfect alignment of the star with the center of the vortex phase mask create rapid fluctuations of the stellar leakage, which also enhance speckle noise and starlight-related photon noise. When telescope vibrations are not taken into account, SCAO simulations contain a very small amount of pointing jitter (around 0.1 mas). Taking into account telescope vibrations could increase this jitter beyond 1 mas RMS. To explore the influence of pointing jitter, additional high-frequency random jitter has been added to the SCAO phase screens, with four different levels: 0.5 mas, 1 mas, 2 mas, and 5 mas RMS, using the 1-h sequence sampled at 300 msec. Fig. 6.12 shows that the influence of high-frequency pointing jitter shows up mostly at short angular separations.

While the influence of high-frequency pointing jitter largely averages out during post-processing, slow pointing drifts (see Fig. 6.13) are expected to have a very large impact on post-processed contrast. Slow pointing drifts are not expected to be due to SCAO itself, as it will provide excellent stability of the set point, but rather due to the non-common path between SCAO and the coronagraph, including the effect of differential atmospheric refraction between K band (where SCAO operates) and longer wavelengths (where coronagraphic observations are performed).

Quasi-static pointing errors can even lead to systematic biases in the final, post-processed images, e.g., by making one side of the image brighter than the other (see Fig. 6.11, right). Such errors can be associated with mechanical drifts in the coronagraphic components (e.g., vortex phase mask), or to imperfect prediction of

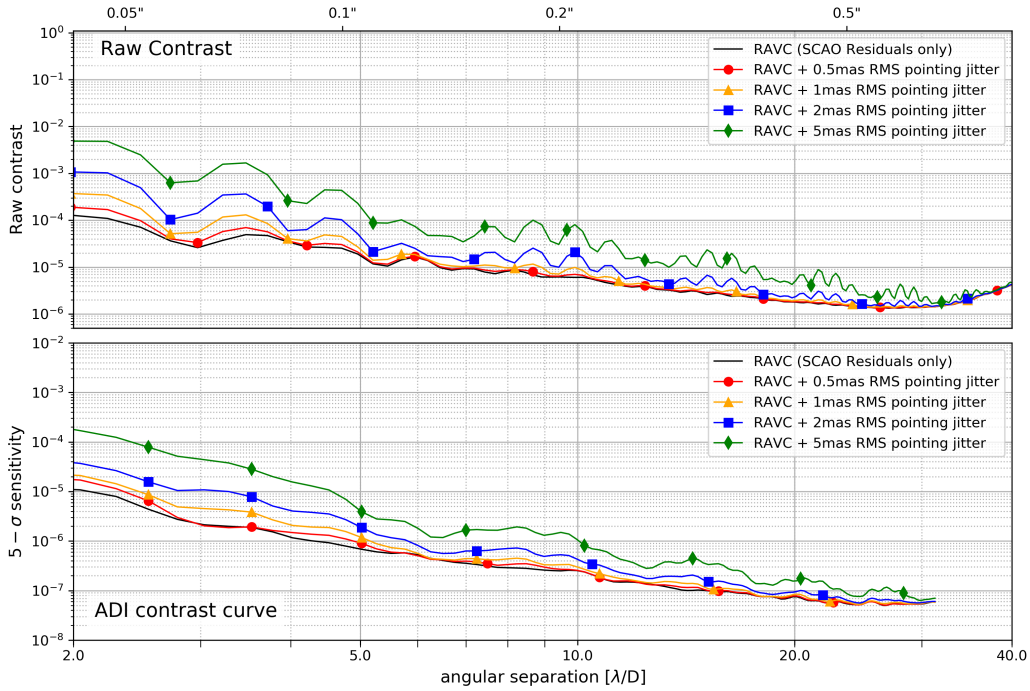

FIGURE 6.12: Raw contrast (top) and ADI post-processed contrast (bottom) for HCI performance for the RAVC at L band in presence of pointing jitter, considering only the contribution of AO residuals speckle noise.

the effect of atmospheric refraction on the PSF position at the vortex phase mask location. This is the reason why common-path pointing control will be implemented in METIS, using the QACITS algorithm (Huby et al., 2015). This algorithm derives the centering error by analyzing the shape of the coronagraphic PSF on the science camera.

To investigate the influence of non-common path pointing errors, low-frequency pointing drifts have been added to the SCAO phase screens with a timescale equal to the full observing sequence, and with PtV amplitudes ranging from 0.2 to 2 mas. The star was set to move along the x axis during the AO sequence. As in the case of pupil drifts, this represents a worst-case scenario, because the timescale of the offset perfectly matches the timescale of the ADI sequence. It is implicitly assumed here that the pointing control algorithm (QACITS) does not produce any significant bias on the centering of the star, which should be the case for a good alignment between the input pupil and the Lyot stop (Huby et al., 2017).

Low-frequency pointing drifts have a huge impact on the final sensitivity (see Fig. 6.13): a PtV amplitude of 0.4 mas would already marginally break the requirement of 3×10^{-6} at $5\lambda/D$. This corresponds to $0.02\lambda/D$ PtV at L band. Previous experience with QACITS at Keck/NIRC2 (Huby et al., 2017) shows that the closed-loop pointing stability using feedback from the science camera can go down to about $0.01\lambda/D$ RMS (i.e., $\sim$ $0.025\lambda/D$ PtV) using a simple integrator with a control frequency around 0.1 Hz. While this is slightly larger than the requirement to keep the METIS performance compliant with the self-defined requirement, it must be noted that speckles associated to temporal frequencies higher than 0.001 Hz will

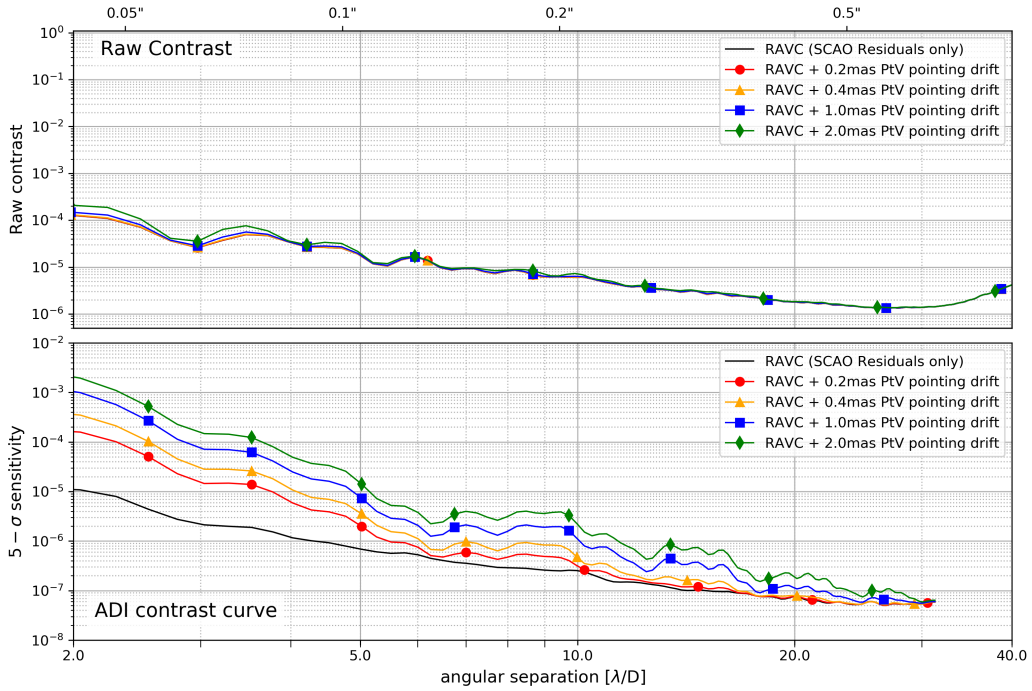

FIGURE 6.13: Raw contrast (top) and ADI post-processed contrast (bottom) for HCI performance for the RAVC at L band in presence of various PtV amplitudes of low-frequency pointing drift, considering only the contribution of AO residuals speckle noise.

average out to some level during the ADI post-processing, and that the contribution of frequencies below 0.001 Hz to the total RMS pointing error should be significantly smaller than $0.01\lambda/D$ thanks to the integral control.

6.2.5 Petal piston

As for most ground-based telescopes, the ELT pupil is divided into a number of separated regions (referred to as petals) by the support structure of the secondary mirror (spider arms). The presence of spiders has recently been shown to be at the origin of the "low wind effect", which creates additional aberrations at low spatial frequencies that are not well detected by standard Shack-Hartmann wavefront sensors (Milli et al., 2018). Even worse, the discontinuity of the pupil can lead to an artificial buildup of piston error between petals in closed-loop AO operations. Fortunately, the pyramid wavefront sensor used in METIS is more sensitive to this petal piston mode, and specific strategies will be implemented to mitigate this effect (Hutterer et al., 2018b).

In order to evaluate the effect of petal piston on the coronagraphic performance, differential piston between petals has been introduced in the SCAO phase screens, with various amplitudes (10, 20, 50, and 100 nm). A first test introduced static petal piston, which demonstrated small effect on the contrast curves, because the ADI post-processing is able to average its effect on the sequence. We then only consider the case of variable petal piston, assuming a sinusoidal behaviour for all petals. To avoid coherent effects between petals, the phase of the sinusoid is chosen different

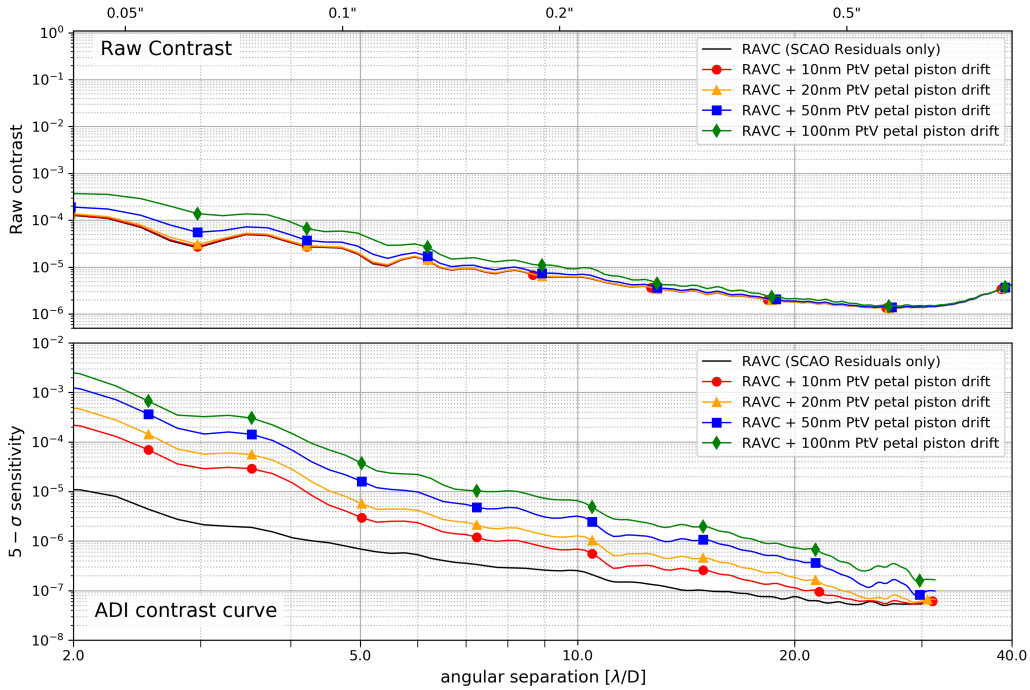

FIGURE 6.14: Raw contrast (top) and ADI post-processed contrast (bottom) for HCI performance in presence of variable piston between the six ELT petals, for the case of petal piston drift, with a drift timescale of 1 h, considering only the contribution of AO residuals speckle noise.

for the piston in all petals, and its amplitude is slightly varied from one petal to the other. Two different timescales were chosen to inject petal piston on the 1-h SCAO sequence, with periods of approximately 1s (Fig. 6.15) and 1 h (Fig. 6.14). As already seen in the case of pointing errors, a high-frequency time evolution is largely averaged out by the ADI post-processing, while a slow drift has a very detrimental effect on the final contrast. Simulations indicate that a high-frequency jitter of up to 100 nm PtV is acceptable, while low-frequency drifts should be limited to about 10 nm PtV. Preliminary simulations of advanced wavefront reconstruction with the Pyramid WFS suggest that a drift of around 20 nm PtV is within reach (Hutterer et al., 2018a). Although this would break the self-imposed requirement, it can be noted that this amount of drift would still leave a large margin with respect to the top-level requirement of 3×10^{-5} at $5\lambda/D$. Once again, a large part of the petal piston in the SCAO residuals will appear at temporal frequencies that are at least partly averaged out by ADI - the whole 20nm PtV does not show as a 1h-long sinusoid.

6.2.6 Non-common path aberrations

NCPA (beyond pure pointing errors, described in Sect. 6.2.4) are known to be a major contributor to HCI performance budgets, and are supposed to be the limiting factor to the performance of many state-of-the-art instruments. In order to mitigate

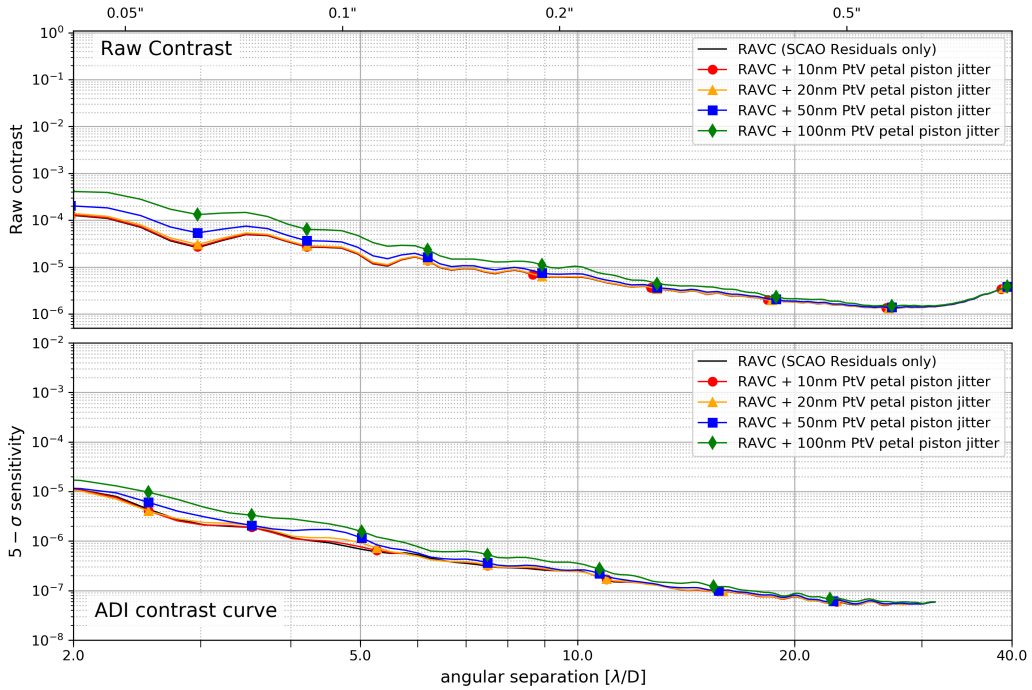

FIGURE 6.15: Raw contrast (top) and ADI post-processed contrast (bottom) for HCI performance in presence of variable piston between the six ELT petals, for the case of piston jitter at 1 Hz, considering only the contribution of AO residuals speckle noise.

the effect of NCPA on the METIS HCI performance, a common-path wavefront sensing/correction technique, referred to as PSI (Codona et al., 2013) will be used. With this algorithm, NCPA are sensed in real time using the data from the IMG camera and the telemetry from the PyWFS, and fed back to the SCAO system for correction through WFS slope modifications. In this situation, the NCPA measured by PSI are transferred to the SCAO, which then operates around a non-zero wavefront error. This may lead to a decrease in wavefront control performance for the SCAO. Here, it is assumed that this decrease in performance can be efficiently mitigated, be it by software or hardware (e.g., addition of a compensating phase plate in the SCAO optical train), and only the direct consequences of NCPA on the coronagraphic performance are studied. In order to simulate the influence of NCPA, we used a series of Monte Carlo simulations of the wavefront aberrations between the tip of the pyramid inside SCAO and the IMG-PP1 pupil plane, where the Lyot stops and APP are placed inside the IMG camera. These simulations take into account the PDR-level knowledge of the METIS optical train. An example of such an NCPA phase map is show in Fig 6.16, and will be used in the rest of this section.

The presence of static NCPA at the level of the coronagraph is expected, because PSI will only correct low-order wavefront aberrations. Here, it is assumed that PSI will typically be able to measure and correct for spatial frequencies up to 10 cycles per pupil, although this figure will depend on the fine tuning of the algorithm. Fig. 6.17 shows the influence of static NCPA after filtering the low spatial frequencies out of the NCPA map shown in Fig. 6.16. We also show the case where low

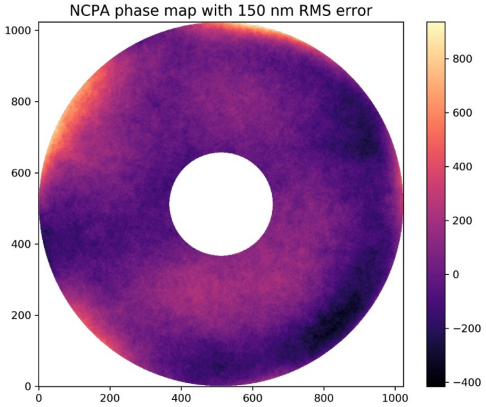

FIGURE 6.16: Representative NCPA phase map between the SCAO PYR and IMG-PP1, where the Lyot stops and APP are located.

spatial frequencies have not been filtered out, which would correspond to a case where the PSI correction would fail. In order to simulate various amounts of static NCPA, the NCPA map was rescaled to various RMS wavefront errors, ranging from 100 to 200 nm (the latter being significantly beyond what is expected for METIS). This figure shows that, even though they create a purely static contribution to the coronagraphic PSF, static NCPA would have a significant influence on the HCI performance if they were not corrected by a common-path wavefront sensing method like PSI. In order to provide a post-processed contrast smaller than the self-defined requirement, the static NCPA level would need to be smaller than 150 nm RMS, which is within reach based on the METIS preliminary design. Yet, in order to reduce the huge effect of NCPA on raw contrast, and to improve the performance in terms of post-processed contrast, a common-path wavefront sensing technique like PSI would definitely be useful. Once the low-order modes are removed by PSI, the contribution of medium- to high-order NCPA to the HCI performance becomes completely negligible (even in terms of raw contrast) at the angular separation where the contrast requirement is defined.

Based on the previous discussion, and assuming that PSI drives the low-order wavefront aberrations to a flat wavefront on average (no significant bias in the correction), it can be stated that static NCPA will be mostly benign to the METIS HCI performance. Dynamic (aka quasi-static) NCPA are more worrisome than static NCPA, and are expected to largely affect HCI performance. While the METIS design should in principle minimise NCPA variations thanks to the gravity-invariant, temperature-controlled, and mostly non-moving optical train (except for the chopper and the SCAO field selector and modulator), it can still be expected that NCPA will vary to some level during the observations, e.g., because of chromatic variations in the footprint of the beam on the optics.

Fig. 6.18 illustrates the simulated HCI performance in presence of NCPA variations during the entire ADI sequence. In order to create these NCPA variations, the input NCPA map was rescaled with a sinusoidally varying factor that makes the rms wavefront error in the rescaled map go from zero up to the value quoted in the legend of Fig. 6.18, assuming a period of 1 h for the sinusoid (worst case scenario).[1] It is assumed here that PSI does a good job cancelling the static, low spatial frequency part of the NCPA map, and that higher spatial frequencies have a negligible effect

[1]The mean PtV amplitude over time for the wavefront error measured at each individual pixel of the pupil is a factor $\sqrt{2}$ smaller than the values quoted in the legend.

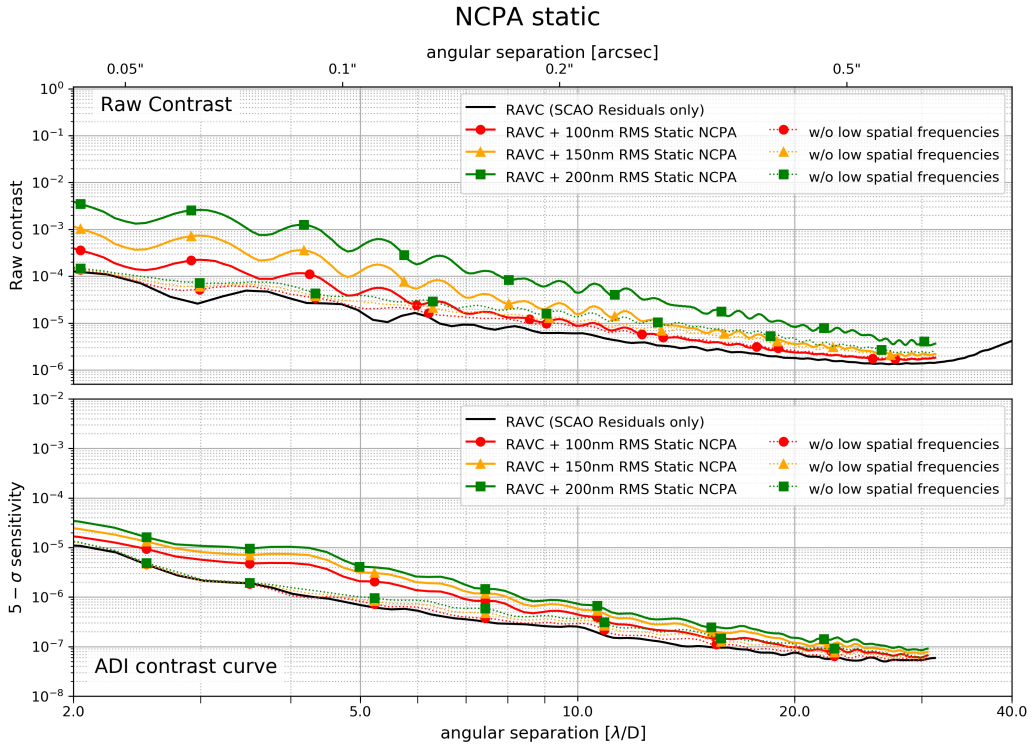

FIGURE 6.17: Raw contrast (top) and ADI post-processed contrast (bottom) for HCI performance in presence of various levels of static NCPA on the HCI side (the dashed curves correspond to the same NCPA maps as the solid curves, from which the low-order modes up to 10 cycles per pupil have been removed.), considering only the contribution of AO residuals speckle noise.

on the HCI performance as described above, so that the variable NCPA simulations can be performed around a zero-mean NCPA map. The raw contrast shows a better behaviour than the ADI 5σ contrast: on one side the ADI contrast is a 5σ, which means that it can be up to 5 times higher than the raw contrast; on the other side we could have a mean contrast of 1×10^{-4} at a given separation, with locally brighter (few times 10^{-4}) speckles during part of the ADI sequence, that the classical ADI cannot correct, because of this timescale. In order to preserve the self-defined contrast requirement of 3×10^{-6} at $5\lambda/D$, dynamic NCPA should have an amplitude smaller than about 15 nm PtV. This could turn out to be a challenging specification to meet, be it by design or by usage of PSI closed-loop control. The overall contrast requirement (3×10^{-5} at 0"1) would still be met with NCPA variations significantly larger than the worst case simulated here (40 nm PtV). We conclude that the goal NCPA stability should be 15 nm PtV over an hour but, recognizing that quasi-static NCPA will be one of the most challenging contributors to address in the contrast budget, NCPA variations up to 20 nm PtV can be tolerated. Although it is too early to assess whether PSI on METIS will achieve this correction accuracy, preliminary simulations suggest that this is within reach, especially for the long timescale considered here. In addition to exploring NCPA variations happening on the timescale of the ADI sequence, more rapid NCPA fluctuations have been studied. For instance, using a sinusoidal NCPA variation with a period 10 times smaller than the duration

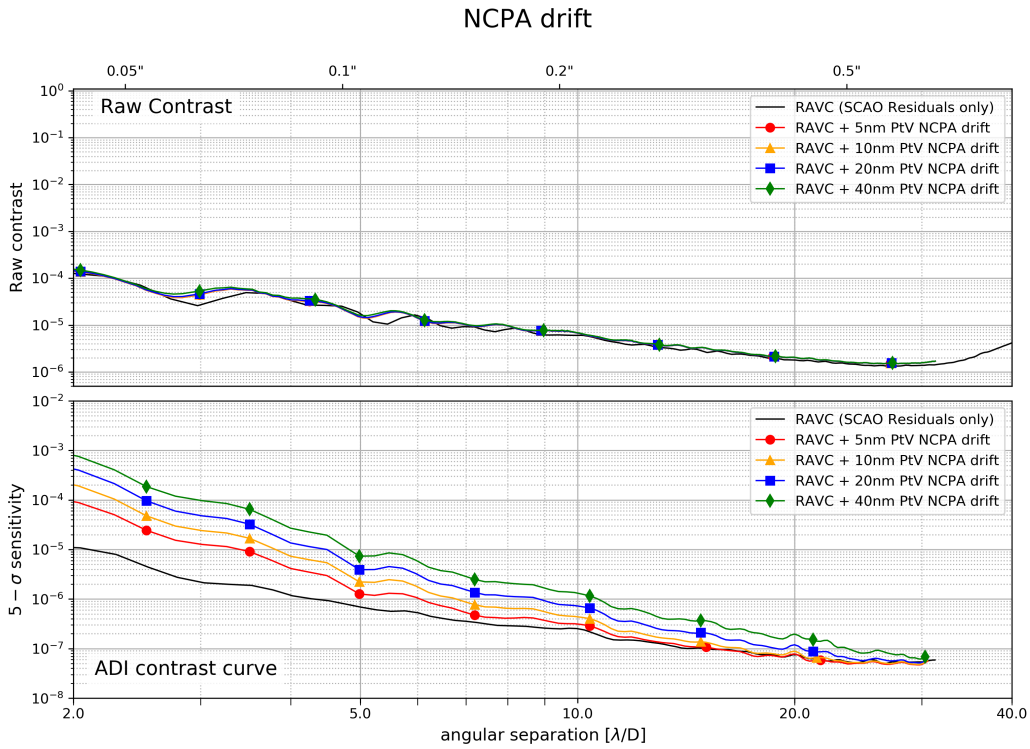

FIGURE 6.18: Raw contrast (top) and ADI post-processed contrast (bottom) for HCI performance in presence of various levels of NCPA drifts, with a timescale equal to the duration of the ADI sequence, considering only the contribution of AO residuals speckle noise.

of the ADI sequence, the resulting ADI post-processed contrast improves by a factor around 2. This is another demonstration that the worst case scenario for noise source is slow variations on the timescale of the ADI sequence. This also means that the control bandwidth of PSI can be relatively low, down to about 0.01 Hz if needed, which should allow very high signal-to-noise ratio to be built up on the NCPA measurement.

6.3 Combination of effects

Tab. 6.1 summarises the results of this analysis, by showing the level of each effect that would lead to an ADI contrast 10 times below the top-level contrast requirement of 3×10^{-5} at $5\lambda/D$. The last column of the table presents the current best guess of the level of each of these effects in METIS.

To conclude, we now present a preliminary estimation of how the contrast will be impacted by a combination of all these effects, using the best guess for their nominal value. We assume for these simulations a pupil with seven misaligned segments under a nominal seeing of 0"65, with 2 mas RMS pointing jitter, 0.4 mas PtV of slow pointing drifts, 20 nm PtV of NCPA drifts, and 2% PtV pupil drift. Because petal piston is mostly associated to low spatial frequencies, it will also be sensed by PSI, and is therefore counted inside the NCPA drift budget. In this simulation, all drifts are assumed to happen at the worst possible timescale, i.e., similar to the duration of the ADI sequence.

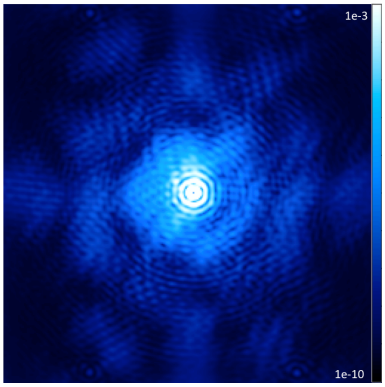

FIGURE 6.19: RAVC PSF resulting from a combination of errors: 7 misaligned segments, 2 mas RMS pointing jitter, 0.4 mas PtV pointing drift, 2% PtV pupil drift, and 20 nm PtV petal piston drift and NCPA drift.

TABLE 6.1: Tolerable values for noise sources in L-band RAVC observations, in order to reach a post-processed contrast ten times smaller than the top-level requirement. The last column gives the best guess on the actual value for each effect.

	units	requirement/10	expected
seeing	arcsecond	>0"95	0"65
pointing jitter	mas RMS	2	< 2
pointing drift	mas PtV	0.4	~ 0.4
static NCPA (total)	nm RMS	150	0 (low orders)
dynamic NCPA	nm PtV	15	20
low-frequency petal piston	nm PtV	10	20
misaligned segments	N/A	7	0 or 7
input pupil stability	PtV	3%	2%

The coronagraphic PSF associated to this simulation is illustrated in Fig. 6.19, while the contrast performance is shown in Fig. 6.20. These simulations show that the combination of all these effects leads to a final post-processed contrast that is still compatible with the top-level requirement, although the margin is very small. This performance simulation takes into account a set of seven misaligned segments. Considering only the case where all mirror segments are properly aligned would provide some margin with respect to the requirement.

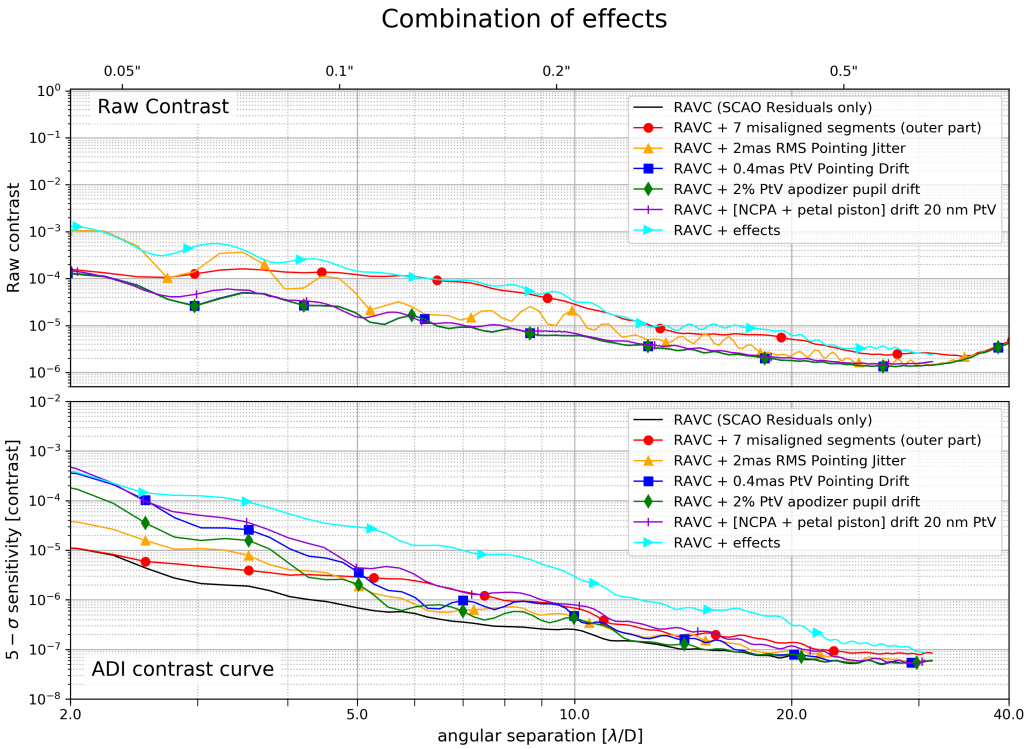

FIGURE 6.20: Raw contrast (top) and ADI post-processed contrast (bottom) HCI performance in presence of a combination of effects: 7 missing segments, 2 mas RMS pointing jitter, 0.4 mas PtV pointing drift, 2% PtV pupil drift, and a combination of NCPA and petal piston drift with 20 nm PtV amplitude.

Chapter 7

Scientific capabilities

By using the 1-h SCAO sequence with 300-msec sampling, we analyse the expected observational capabilities of METIS with respect to several known star-planets systems, such as HR8799 and β Pic. In these simulations, the planets are inserted and processed through ADI-PCA with an optimal number of principal components. With respect to a simple ADI processing, the PCA-ADI delivers images with a clearer detection (whenever possible), and a better aesthetic quality. The optimisation of principal components (PCs) is performed in VIP by maximizing the signal-to-noise ratio (S/N) for a given location in the image, by running a grid search varying the value of PCs and measuring the S/N for the given coordinates. These simulations show the great potential of METIS to increase the sensitivity to faint companions in the thermal infrared range.

7.1 Alpha Centauri

Alpha Centauri (α Centauri or α Cen) is the stellar system closest to our solar system, being located at 1.35pc. It is composed of three stars: α Centauri A (*Rigil Kentaurus*), α Centauri B (*Toliman*) and α Centauri C (*Proxima Centauri*), and contains at least one planet.
α Centauri A and α Centauri B form the binary star system α Centauri AB. Both stars are similar to the Sun, being of classes G and K. With the naked eye, they seem to be a single star, with apparent magnitude of -0.27, the third brightest in the sky after Sirius and Canopus. α Centauri A is 1.1 solar mass star, while α Centauri B is smaller (0.907 solar mass). α Centauri C is a red dwarf, much smaller than the other two stars (only 0.15 solar mass) and much fainter (apparent magnitude of 11.05).
Proxima Centauri b (Anglada-Escudé et al., 2016), discovered in 2016 by Doppler measurements (based on measurements from the High Accuracy Radial velocity Planet Searcher (HARPS) and the Ultraviolet and Visual Echelle Spectrograph (UVES)), is a small planet orbiting Proxima Centauri, with a period of 11.2 days. Being observed only by radial velocity, only the minimal mass of the planet can be established (1.27 Earth masses), while the radius should range between 0.8 and 1.4 Earth radii. It is suggested to be an Earth-like planet, orbiting in the habitable zone of the star. Even though the planet is quite close to the star (with a semi-major axis of about 0.0485 AU), the much fainter star would allow surface liquid water on the planet at such small distance. However, considering the ultraviolet and x-ray flares from the star, life conditions on the surface may be much more difficult than on Earth.

Recently, the possibility of a second planet has been proposed, after analysing additional RV data from HARPS spectrograph (Damasso et al., 2020). This planet would have a mass a few times the one of the Earth (minimum mass $m_c \sin i_c = 5.8 \pm 1.9 M_{Earth}$) and orbital period $P_c = 5.21 years$. Because of its large angular separation from the star ($\sim 1 arcsec$), this planet would be an excellent target for the next

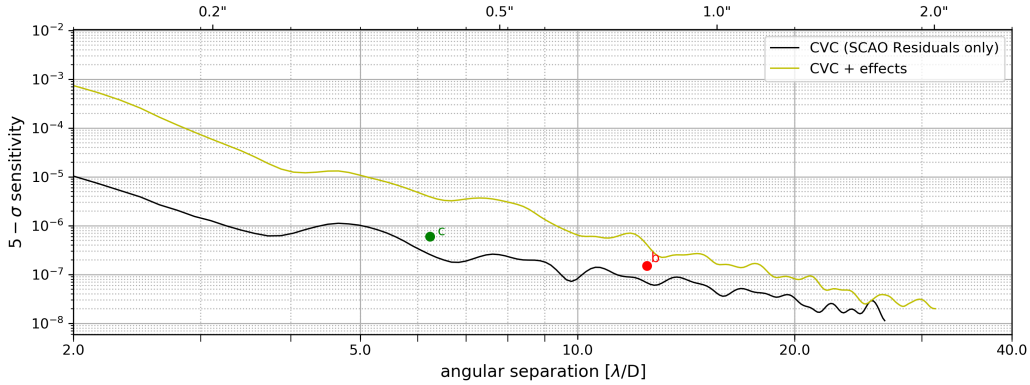

FIGURE 7.1: 5-σ detectability in terms of contrast for point-like companions around αCen in 5h observing time. The two simulated planets are shown for comparison.

generation direct imaging instruments.
The Breakthrough Initiative (https://breakthroughinitiatives.org/) project was launched in 2015 to study more closely the α Centauri system. This project is composed of two parts: one on the ground, with existing telescopes, and the other in space, with new satellites. The NEAR experiment (Kasper et al., 2017, Kasper et al., 2019, Wagner et al., 2021) aims to demonstrate the possibility of directly imaging low-mass planets with current state-of-the-art technology. In particular, the VLT VISIR (Lagage et al., 2004) mid-infrared camera was upgraded with state-of-the-art coronagraphs, a mid-infrared optimized AGPM and a shaped pupil (Carlotti et al., 2012, Ruane et al., 2015), and moved to the UT4, where a deformable secondary mirror enables adaptive optics. Using the data collected during the NEAR observing campaign, a possible companion was identified by Wagner et al., 2021, with mass simular to Neptune. Here, we focus on the detection capabilities of METIS in terms of rocky planets.

TABLE 7.1: α Cen simulated planets summary (contrast level derived from Des Marais et al., 2002).

Planet	Simulation	Observation time [h]	Contrast level	Separation ["]	SNR
b	SCAO only	5	1.5×10^{-7}	0.8	5.26
b	SCAO only	10	1.5×10^{-7}	0.8	5.65
b	SCAO + combination effects	10	1.5×10^{-7}	0.8	3.26
c	SCAO only	5	6×10^{-7}	0.4	7.08
c	SCAO only	10	6×10^{-7}	0.4	7.75
c	SCAO + combination effects	5	6×10^{-7}	0.4	3.82

Our simulations of rocky planet detection around α Cen were performed in N2 band ($Nmag = -1.6$) with the METIS vortex coronagraph (METIS VC), in 5h of observing time, because with a temperature of $\sim 300K$, the simulated planets are barely emitting in L and M bands. Des Marais et al., 2002 predicted $0.4\mu Jy$ for an

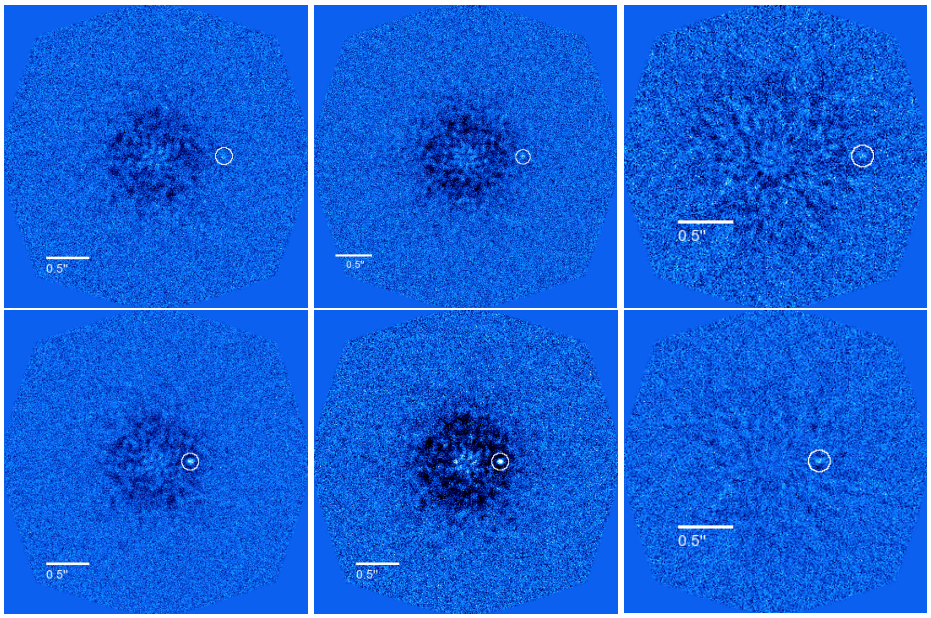

FIGURE 7.2: α Cen planets ADI post-processed images in N2 band with CVC (from top left to bottom right): planet b at 0.8″ with 1.5×10^{-7} constrast level in 5h of observing time (top, left), in 10h of observing time with SCAO Residuals only (top, centre), and in 10h observing time with a combination of effects (top right); planet c at 0.4″ with 6×10^{-7} constrast level in 5h of observing time (bottom, left), in 10h of observing time with SCAO Residuals only (bottom, centre), and in 5h of observing time with a combination of effects (bottom right).

Earth analog at 10 pc at 11.25μm, which translates to 20μJy at 1.35 pc, with αCen A having a flux of 130Jy. We can then simulate (i) hypothetic planet b, a Earth analog in the habitable zone around $\alpha CenA$ at a distance of 1.1 AU (0.8″), with a contrast level of 1.5×10^{-7}, and (ii) hypothetic planet c, twice as close at 0.55 AU (0.4″), with a contrast level of 6×10^{-7}. The 5-σ detectability in 5h observing time is presented in Fig. 7.1 for SCAO residuals only and combinations of effects, with the two planets shown for comparison. The simulated ADI post-processed images are presented in Fig. 7.2.

A planet with 1.5×10^{-7} contrast level is barely detectable (SNR $\simeq$ 5, see Tab. 7.1) in a 5h observing time, while with 10h the planet is slightly more straightforwardly detected. However, when all effects (see Sect. 6.3) are included, the SNR for the 1.5×10^{-7} with 10h observing time drops to 3.26 (with 5h, the planet is not visible), making it even more difficult to detect (see Fig. 7.2). In this case, it would require a planet about 1.4$\times$ larger to allow a detection.
A closer planet at 0.4″ with higher contrast level of 6×10^{-7} is quite easily detected in 5h (SNR of 7.08), but it is slightly drowned in the residual speckles when all effects are included in the simulation (SNR = 3.82 with 5h observing time).

7.2 Beta Pic

Beta Pictoris (β Pic / β Pictoris) is an A-type star located at 19.4 pc from our Solar System. It has a K-magnitude of 3.48, a mass $M = 1.75 M_{Sun}$ and radius $R = 1.8 R_{Sun}$.

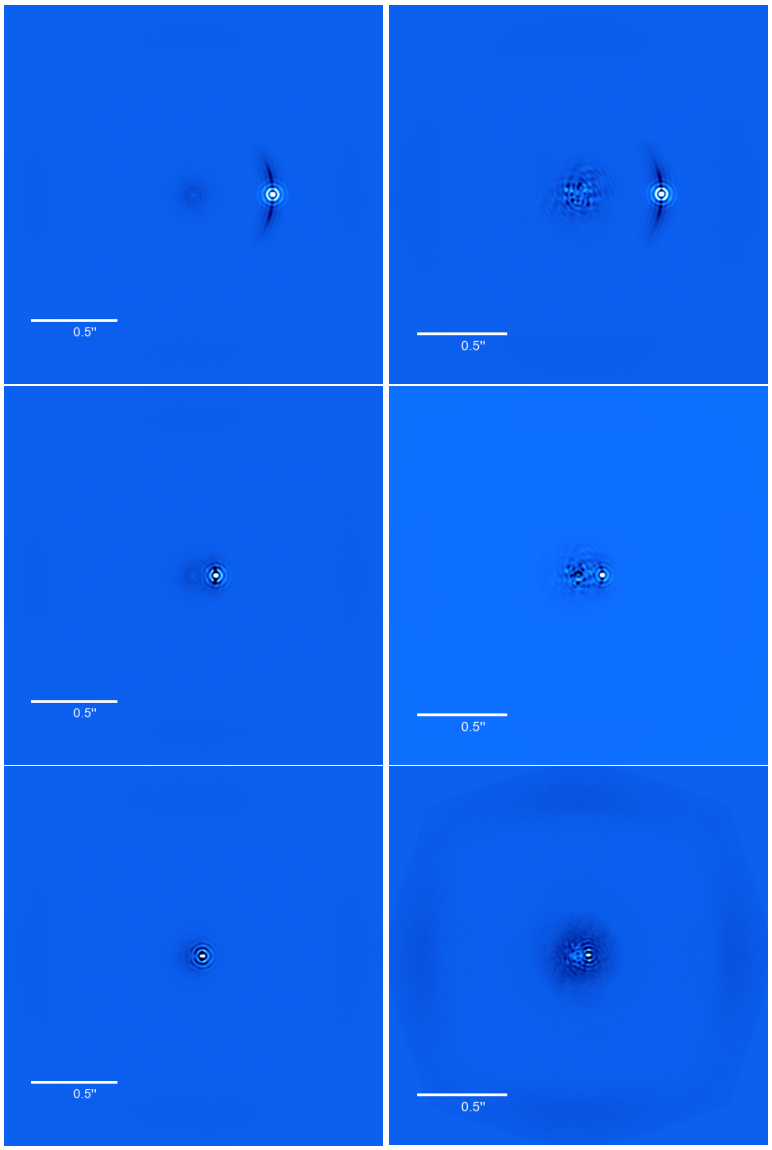

FIGURE 7.3: β Pic planet ADI post-processed images in L band with RAVC in 1h of observing time with 6.3×10^{-4} constrast level at different angular separation (top: 0.46"; centre: 0.13"; bottom: 0.05";) with SCAO only (left column) and with SCAO + combination of effects (right column).

It is a quite young star ($\sim 21 Myr$, Binks et al., 2014), best known for its circumstellar disk (Smith et al., 1984). The star hosts two exoplanets (Lagrange et al., 2009, Lagrange et al., 2019): planet b has a mass of $\sim 8 M_{Jup}$, at $\sim 8 AU$; planet c has a mass of $\sim 9 M_{Jup}$, at a distance of $\sim 2.7 AU$.
Planet b was simulated for a 1h observing time at L band ($Lmag = 3.4$ for the star) with the RAVC and a 6.3×10^{-4} contrast level (Lagrange et al., 2019) at three angular separations: (i) max separation, (ii) shortest separation measured to date, and (iii) shortest separation that can be measured by METIS (see Fig. 7.3). At N2 band ($Nmag = 3$ for the star), the planet was simulated for a 1h observing time with CVC and 1×10^{-3} contrast level (Vandenbussche et al., 2010, Danielski et al., 2018) at max separation, 0.46", (see Fig. 7.4).

In all cases, the planet is very distinctly visible in the post-processed images (see

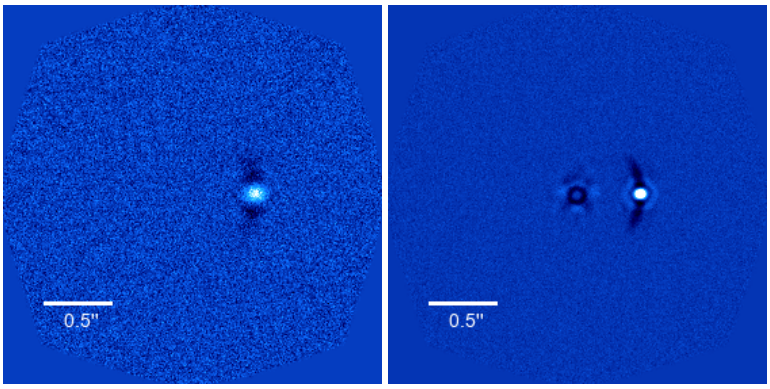

FIGURE 7.4: β Pic planet ADI post-processed images in N2 band with CVC in 1h of observing time with 1×10^{-3} constrast level at 0.46" angular separation with SCAO only (left) and with SCAO + combination of effects (right).

TABLE 7.2: β Pic simulated planets summary (contrast level derived from Lagrange et al., 2019, Vandenbussche et al., 2010, Danielski et al., 2018).

Observation band	Simulation	Contrast level	Separation ["]	SNR
L band	SCAO only	6.3×10^{-4}	0.46	42.63
L band	SCAO + combination effects	6.3×10^{-4}	0.46	62.56
L band	SCAO only	6.3×10^{-4}	0.13	13.69
L band	SCAO + combination effects	6.3×10^{-4}	0.13	24.77
L band	SCAO only	6.3×10^{-4}	0.05	9.18
L band	SCAO + combination effects	6.3×10^{-4}	0.05	11.09
N2 band	SCAO only	1×10^{-3}	0.46	10.17
N2 band	SCAO + combination effects	1×10^{-3}	0.46	18.38

Fig. 7.3 and Fig. 7.4), with only a slight drop in the SNR when all effects are included in the simulation (see Tab. 7.2). Even at the shortest angular separation measurable from METIS, $50mas$, the planet is still clearly detectable.

7.3 HR8799

HR8799 is an A5V star, located at 40.9pc from our Sun, in the constellation of Pegasus. It is quite a young star ($\sim 40Myr$), with mass $M = 1.5M_{Sun}$ and 4.9 times brighter than the Sun. The star hosts two dusty debris belts (Su et al., 2009, Zuckerman et al., 2011) and at least four giant exoplanets (Marois et al., 2008), detected by high contrast infrared direct imaging. The four planets have masses between 7 and $10M_{Jup}$, and they are located between 14 and 64 AU. A possible fifth exoplanet at smaller angular separation ($<$ 10 AU) has been predicted (Goździewski et al.,

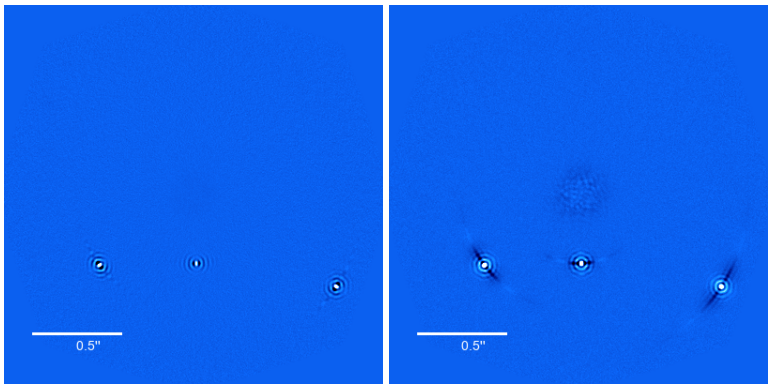

FIGURE 7.5: HR8799 planets ADI post-processed images in L band with RAVC in 1h of observing time with SCAO only (left) and with SCAO + combination of effects (right): planet c with 1.6×10^{-4} at 0.95″ angular separation, planet d with 1.9×10^{-4} at 0.66″ angular separation, and planet e with 1.9×10^{-4} at 0.39″ angular separation.

2014), but further studies (Currie et al., 2014, Defrère et al., 2014, Maire et al., 2015) have failed to find it. A recent study (Thompson et al., 2023) has analysed archival data, using a Bayesian modeling technique while compensating for plausible orbital motion, and it presents a tentative candidate, with mass $4 - 7 M_{Jup}$ at $4 - 5$ AU.

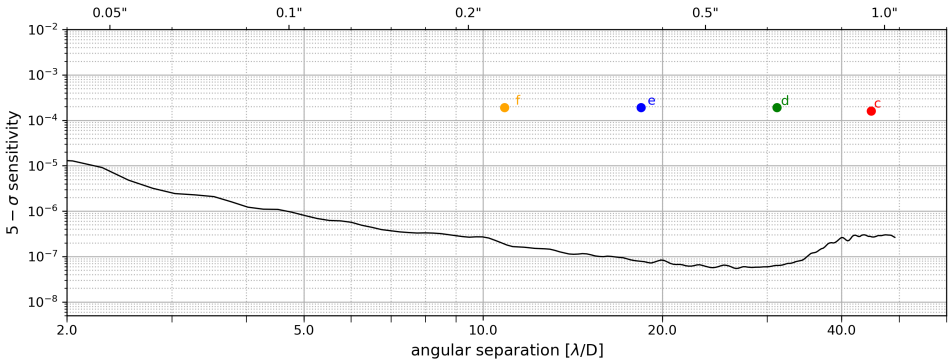

FIGURE 7.6: 5-σ detectability in terms of contrast for point-like companions around HR8799 in 1h observing time. The three planets are shown for comparison. The candidate fifth planet, HR8799 f, could also be easily detected.

Three of the four confirmed planets have been simulated in 1h observing time in L band ($Lmag = 5.2$) with RAVC (see Fig. 7.5). Planet b, at 1.72″, is well within METIS FoV, but outside of our simulation FoV (which stops at 1.2″).
All planets are very easily detected, even when all effects are included in the simulation (see Fig. 7.5). As it can be seen from Fig. 7.6, the contrast reached by METIS would allow us to observe planets with similar contrast level much closer to the star: if present, planet f (Thompson et al., 2023) will be easily detected.

7.4 Radial velocity planets

Up to now, only the β Pictoris planetary system has been studied with both radial velocity and direct imaging techniques, allowing a deep knowledge of its characteristics. In the next section, we will show four planetary systems, well studied via radial velocity, with fairly old planets, for which METIS will be able to deliver direct imaging data, allowing to better constrain the theoretical models for these old planets.

TABLE 7.3: Radial velocity simulated planets summary. Contrast levels were derived from: Quanz et al., 2015 for HD128311; Fischer et al., 2009 for HD87883; Mawet et al., 2019, Pathak et al., 2021, and Llop-Sayson et al., 2021 for ϵ Eridani; Viswanath et al., 2021, and Pathak et al., 2021 for ϵ Indi A

Star	Planet	Simulation	Coronagraphic mode	Observation band	Observation time [h]	Contrast level	Separation ["]	SNR
HD128311	b	SCAO only	RAVC	L band	1	6.9×10^{-6}	0.108	12.06
HD128311	b	SCAO + combination effects	RAVC	L band	1	6.9×10^{-6}	0.108	0.81
HD128311	b	SCAO + combination effects	RAVC	L band	5	6.9×10^{-6}	0.108	0.88
HD128311	c	SCAO only	RAVC	Lband	1	2.7×10^{-6}	0.066	3.20
HD128311	c	SCAO + combination effects	RAVC	L band	1	2.7×10^{-6}	0.066	0.65
HD128311	c	SCAO + combination effects	RAVC	L band	5	2.7×10^{-6}	0.066	1.70
HD87883	b	SCAO only	CVC	Lband	5	8.8×10^{-7}	0.30	5.99
HD87883	b	SCAO + combination effects	CVC	L band	5	8.8×10^{-7}	0.30	4.59
ϵ Eridani	b	SCAO only	RAVC	M band	1	7.5×10^{-7}	1.0	4.55
ϵ Eridani	b	SCAO only	RAVC	M band	5	7.5×10^{-7}	1.0	8.62
ϵ Eridani	b	SCAO + combination effects	RAVC	Mband	5	7.5×10^{-7}	1.0	5.95
ϵ Indi A	b	SCAO only	CVC	N2 band	1	4.4×10^{-5}	1.07	24.45
ϵ Indi A	b	SCAO + combination effects	CVC	N2 band	1	4.4×10^{-5}	1.07	20.99

7.4.1 HD128311

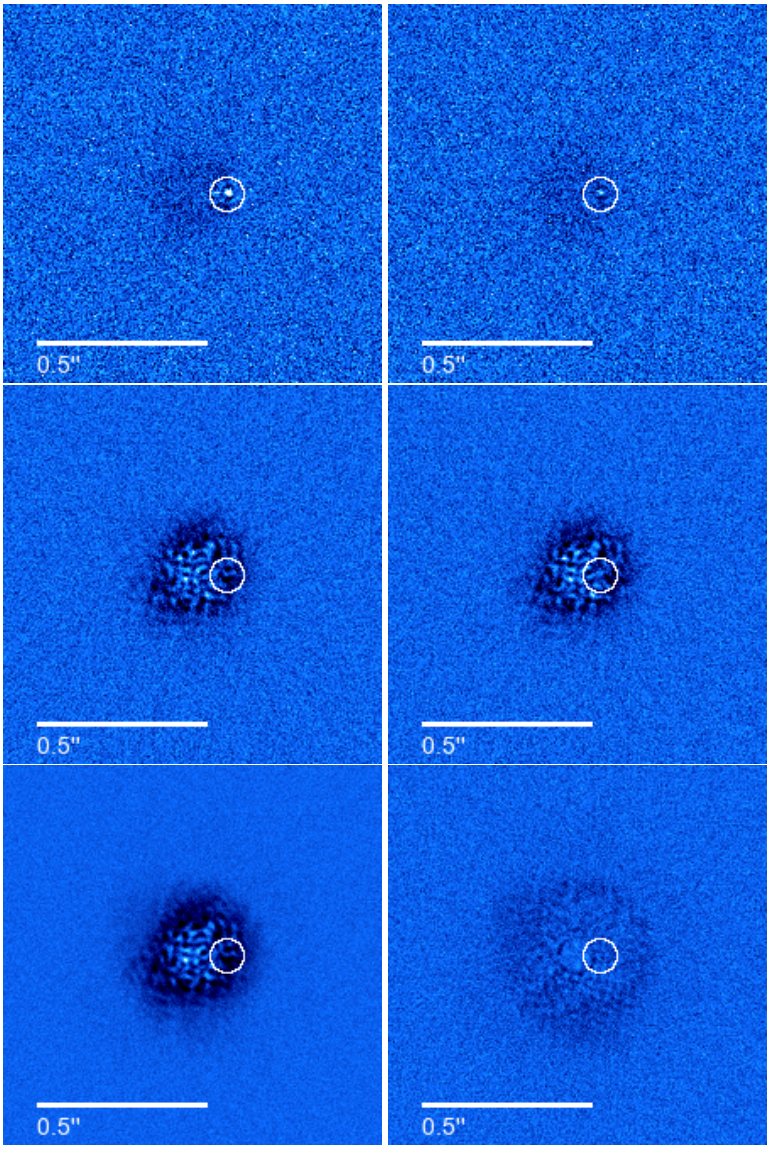

FIGURE 7.7: HD128311 post-processed ADI images (on the left, planet b, with 6.9×10^{-6} at 0.108" angular separation, and on the right, planet c, with 2.7×10^{-6} at 0.066" angular separation) in L band with RAVC with SCAO only (top, in 1h observing time) and with SCAO + combination of effects (center, in 1h observing time, and bottom, in 5h observing time).

HD 128311 is a K0V star, located at 16.34 pc light years from the Sun. The star hosts two exoplanets (Butler et al., 2003, Vogt et al., 2005), discovered by Doppler measurements. HD 128311 b has mass $M = 2.18 M_{Jup}$ and is located at 1 AU, while HD 128311 c has mass $M = 3.21 M_{Jup}$ at 1.76 AU.
The two planets have been simulated in 1h of observing time in L band ($Lmag = 5$) with the RAVC (see Fig. 7.7). The contrast levels were derived from Quanz et al., 2015.

Planet b is very well detectable in 1h observing time when SCAO only is considered (SNR of 12.06, see Tab. 7.3), while planet c is barely visible (SNR of 3.20).

When all effects are taken into account, planet b is not distinguishable in the residual speckles in 5h observing time (see Fig. 7.7). The detectability of these planets will then mostly depend on the capability of METIS to reduce effects as NCPA or petal piston, which are still fairly unknown.

7.4.2 HD87883

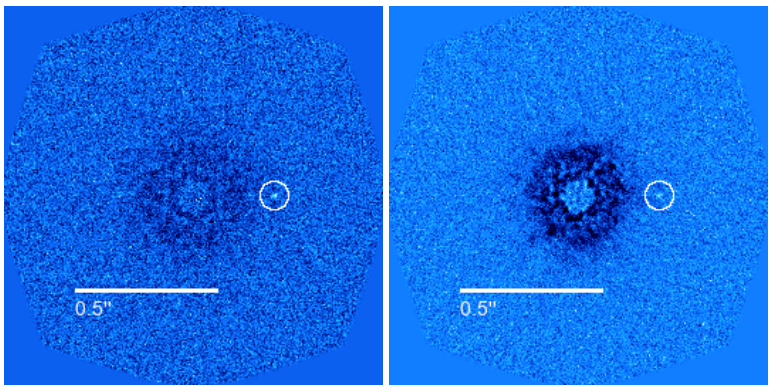

FIGURE 7.8: HD87883 post-processed ADI images in L band with CVC in 5h of observing time with SCAO only (left) and with SCAO + combination of effects (right) with a contrast level of 8.8×10^{-7} at 0.30″ angular separation.

HD 87883 is a K0V star, located at 18.1 pc from the Sun. With an apparent magnitude of 6.27 in the visible range, it is not visible to naked eye. The star has mass $M = 0.82 M_{Sun}$ and radius $R = 0.76 R_{Sun}$, and is aged $\sim$ 9.8 Gyr. The star hosts at least one exoplanet, discovered by radial velocity (Fischer et al., 2009), with mass $M = 1.78 M_{Jup}$, located at 3.6 AU.
The planet was simulated in 1h of observing time in L band ($Lmag = 5.2$) with CVC (see Fig. 7.8). The contrast level was derived from the literature (Fischer et al., 2009).

The simulated planet is clearly visible in 1h observing time when SCAO only is considered, and fairly detectable when all effects are considered (see Fig. 7.8 and Tab. 7.3), even though its SNR is slightly below 5. METIS is essentially background-limited at these angular separations.

7.4.3 ϵ Eridani

ϵ Eridani is a K2V dwarf star, located at 3.2 pc from the Sun, with an apparent magnitude of 3.73 in the visible range. The star is aged 200-800 Myr and hosts a complex debris disk (Aumann, 1985, Walker et al., 2000), and a Jupiter-like planet (Hatzes et al., 2000). The disk is composed of three rings: an inner belt at $\sim$ 3 AU, an intermediate belt at $\sim$ 20 AU, and a main ring between 35 AU and 90 AU. ϵ Eridani b has a mass of $0.65 M_J$ and it is located at 3.53 AU from the star, between the first two belts, and it has an eccentricity of 0.055. Discovered by radial velocity, its orbit is now pretty well constrained, although no direct detection was achieved to date (Mawet et al., 2019, Llop-Sayson et al., 2021).
The planet has been simulated in 1h of observing time in M band ($Mmag = 1.69$) with the RAVC (see Fig. 7.9). The contrast level was derived from the literature (Mawet et al., 2019, Pathak et al., 2021, Llop-Sayson et al., 2021).

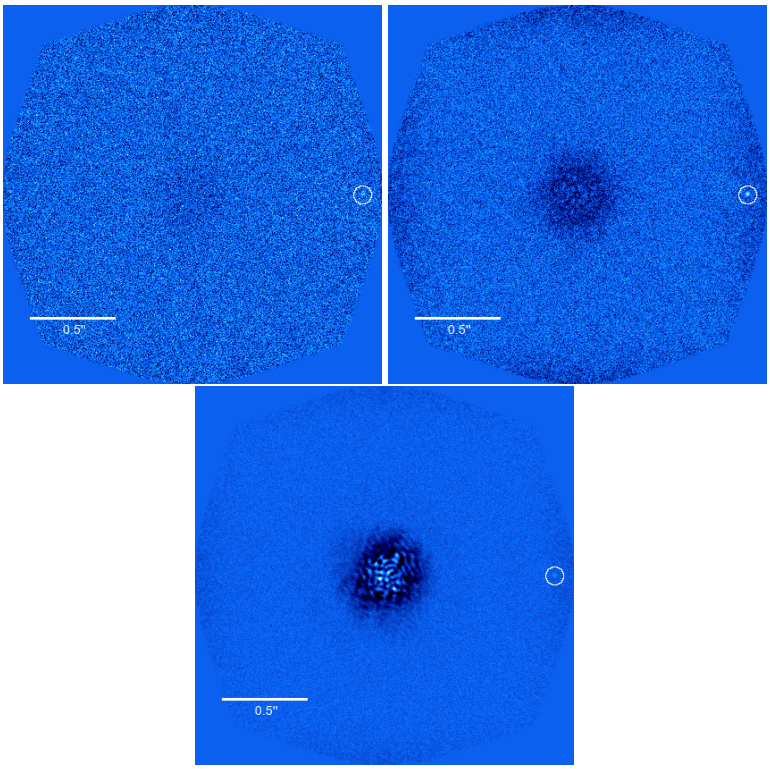

FIGURE 7.9: ϵ Eridani post-processed ADI images in M band with the RAVC with SCAO only, in 1h observing time (top left), and 5h observing time (top right) and with SCAO + combination of effects (bottom, in 5h observing time).

The planet is marginally detected in 1 hour, and more clearly detected with a longer observing time (see Fig. 7.9 and Tab. 7.3), including when all effects are taken into account.

7.4.4 ϵ Indi A

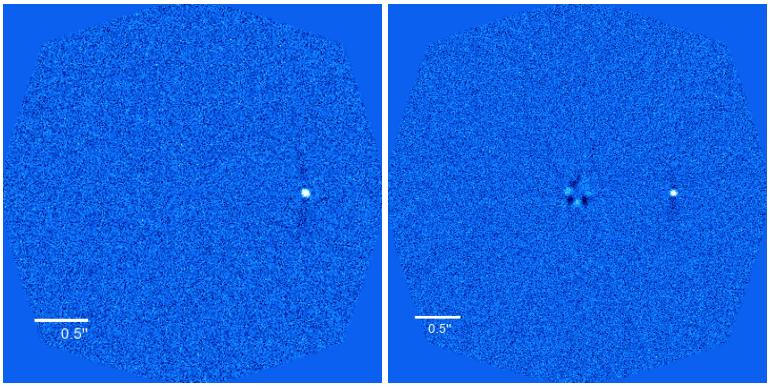

FIGURE 7.10: ϵ Indi planet ADI post-processed images in N2 band with the CVC with SCAO only, in 1h observing time (left), and with SCAO + combination of effects (right).

ϵ Indi is a star system, located at 3.6pc from our solar system. It is composed of 3 stars: a primary star, ϵ Indi A, and a brown dwarf binary system (ϵ Indi Ba and ϵ Indi Bb). The primary star, ϵ Indi A, is a main-sequence star of spectral type K5V, with an apparent magnitude of 6.89 in the visible range. It hosts an exoplanet, a gas giant with $3.25 M_J$, located at 11.55AU (Endl et al., 2002, Feng et al., 2019), with an eccentric orbit (0.26) and period of 45.2yr.
The planet has been simulated with the CVC in 1h observing time in N2-band ($Nmag = 2.0$), at its expected separation (1.07") during the last quarter of 2019 (Pathak et al., 2021, Viswanath et al., 2021). The expected ADI post-processed images are presented in Fig. 7.10, and the final SNR values in Table 7.3, showing a very clear and high SNR detection.

7.5 Expected exoplanets yield

Based on the post-processed ADI contrast curves, it is possible to predict the exoplanet yield from a direct imaging survey of nearby Sun-like stars with METIS (Bowens et al., 2021). By using updated Kepler statistics for the exoplanet population, the expected yield for small planets was obtained via Monte Carlo simulations on eighteen target stars in three bands (L, M, and N2), observed for 1 hour.

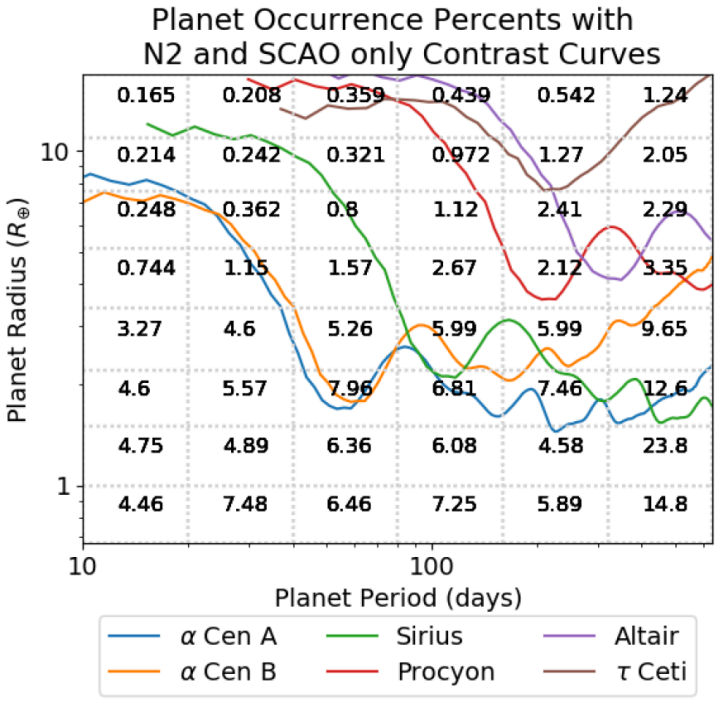

FIGURE 7.11: Occurrence rates from the SAG13 report with contrast curves in the N2 band for the top six candidates stars overlaid. The numbers in each cell are the percent chance of a planet with that radius-period combination appearing around a star. The lowest curve implies the greatest chance of success. The curves shown here are for the N2 band with SCAO effects only for a zero inclination, circular system (from Bowens et al., 2021).

The first step is to generate a synthetic planet population, with known radii and orbits. The occurance rate have been obtained from the NASA ExoPAG SA13 report

(https://exoplanets.nasa.gov/exep/exopag/sag/), a meta-study of other Kepler occurance rate studies. The parameter space of radius and orbital period is divided into cells, each tested randomly. From a Poisson distribution, it is determined if the planet is spawned. Radii and orbital periods are then assigned to the planet within the cell, which is tested once per star. The average system contains 1.72 ± 1.11 planets. The eccentricity is assigned after defining the number of planets in the system (see Van Eylen et al., 2019 for more details). The rest of the planet parameter are assigned either by estimation (inclination, true anomaly, and semi-major axis), either by random generation (longitude of ascending node, argument of periapsis, mean anomaly). The second step consists in generating the contrast curves considering only the CVC at the 3 observing bands (L, M, and N2). Finally, for the sample selection, only nearby (up to 6.5pc) K5 stars are considered. This results in 18 candidates, plus four condidated for a theoretical TMT northern hemisphere survey at a Hawaii or La Palma site. By projecting the contrast curves into the Kepler occurance rate grid, we can determine the star with the greatest chance of detection (see Fig. 7.11). Additional Monte Carlo simulations are performed to determine an optimal observing plan, with multiple epoch observations (each star is re-observed in one month intervals, up to 10 months), to maximize the yield.

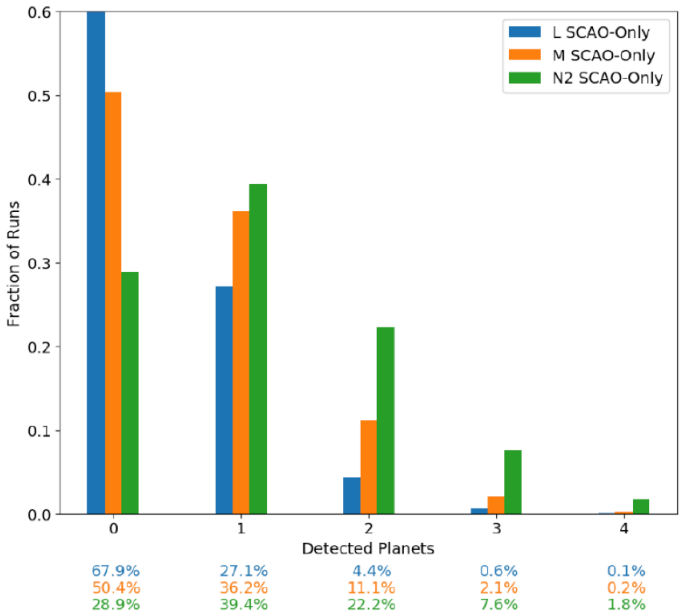

FIGURE 7.12: Detected planets around the top five candidate stars for the SCAO-only case with a 1 hour integration per star and only one epoch observed. There is 71.1% chance of at least one detection in the N2 band (from Bowens et al., 2021).

The results (see Fig. 7.12 and Fig. 7.13) show that there is a high chance (71.1%) of at least one detection in N2 band. These percentages drop to 49.6% in M band, and to 32.1% in L band. For SCAO-only simulations, the expected yield in N2 band is 1.14 planets, 0.66 planets in M band, and 0.38 planets in L band. When all effects are considered, these results are quite different: 0.49 planets for N2 band, 0.14 planets for M band, and 0.06 planets for L band. When all three bands are used for 1-hour exposures, the expected yield increases to 1.41 planets for SCAO-only, and to 0.54 planets for all-effects case. Finally, when more observations are possible, the N2

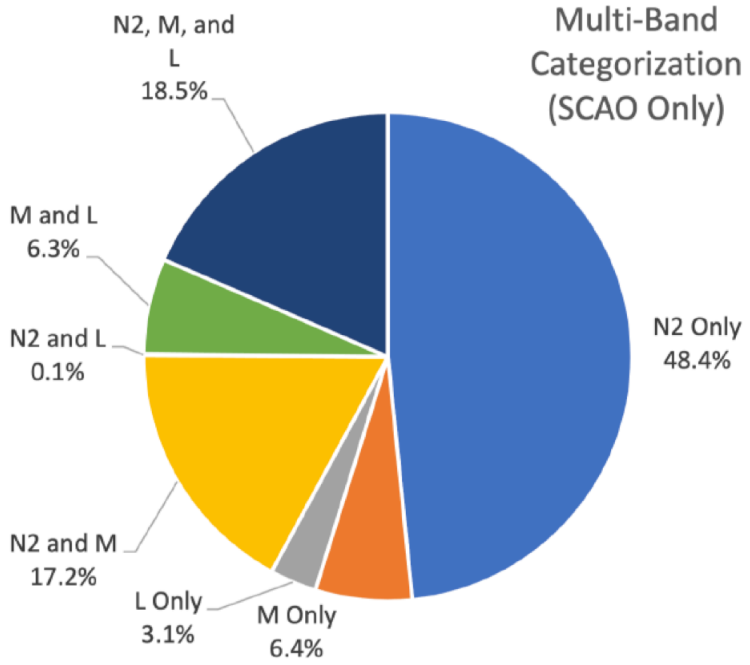

FIGURE 7.13: Percentages of detected planets based on observable band(s) for the SCAO-only case with a 1 hour integration per star and only one epoch observed. There is 42.1% chance of a detection in two or more bands (from Bowens et al., 2021).

yield increases to 1.48 planets. By analysing the heat map of the expected observed planets as presented in Bowens et al., 2021, the N2 band favours planets between 2 to 4 $R_\oplus$ with temperatures from 250K to 400K. The M band has similar radius values, but higher (400K to 700K) temperatures. Finally, L band peaks between 3 to 6 $R_\oplus$ with a wider temperature range (400K to 1000K).

Part IV

Conclusions

Chapter 8

Conclusions and perspectives

8.1 Conclusions

In this dissertation, we have presented the results of our work on the simulated implementation and exploitation of the vortex coronagraph for the future high contrast imaging instrument METIS on the ELT.

The first part of the manuscript introduced the science of exoplanets and the state of the art detection methods. In Chap.1, we firstly presented the essential aspects of exoplanetary science and the main detection methods. Indirect detection methods (see Sect. 1.3) can quite easily detect planets closer to quiet, old stars, giving a good statistics for these objects; while direct methods (see Chap. 2) are less prolific, but can detect planets orbiting farther and/or around younger stars, allowing, with spectroscopy, a more complete analysis of the object spectrum. The complementarity of the two techniques is essential for increasing our knowledge on planets, their formation and evolution. Of course, finding a habitable planet, with biosignatures compatible with life on Earth, is the not-so-hidden objective of the exoplanets community. The critical aspects of the detection methods were presented in Sect. 1.3 and Chap. 2: technical features, observed exoplanets, advantages and disadvantages, with a particular emphasis on the direct detection methods, which are the core of this dissertation.

The second part was dedicated to the design of the coronagraphic modes used in the ELT METIS instrument. Chap. 3 focused on the design and optimisation of the vortex coronagraph (VC) for L, M, and N bands, which are the observational wavebands for the METIS instrument. The latter was presented in Chap. 4, with its principal high contrast imaging features. Aside the vortex coronagraph (VC), the other coronagraphic modes foreseen for METIS are the ring-apodized vortex coronagraph (RAVC), and the apodized phase plate (APP). The three devices have already shown their potential, but an optimised version, together with the increased potential of the ELT, will open a new observational space.

The third part is the core of this dissertation. Chap. 5 introduced the simulation tools used for the end-to-end performance evaluation of the coronagraphic modes of the METIS instrument. The end-to-end simulations are composed of three major steps: (i) AO simulation to obtain residual phase screens, (ii) propagation through the instrument high contrast imaging system, (iii) and finally the ADI post-processing of a mock HCI data set, to get the final performance. The main metric used to evaluate the HCI performance is the post-processed 5σ contrast, as defined in Sect. 5.1.3. For each step, the computation time can become quite prohibitive: a 1-hour SCAO simulation with a sampling of few msec creates $360,000$ phase screens in few days. In order to find the best compromise between computational time and performance simulation, AO sequence duration and sampling have been optimized.

The nominal performance (with only SCAO residual phase screens, and no instrumental effects) for L, M, and N bands were presented in Sect. 6.1. The three coronagraphic modes (CVC, RAVC, APP) were simulated in L, and M bands, while only the CVC is considered at N band, to provide the highest possible throughput. The instrumental and environmental parameters were reviewed in Sect. 6.2, with the L-band RAVC nominal performance as reference. This study demonstrated that the most detrimental effects are the slow variations of observations or misalignments on the timescale of the ADI sequence, while higher frequency jitter largely averages out during post-processing. Static effects, such as misaligned segments, start to have an effect at separations larger than $3\lambda/D$, while other static effects, such as low-frequency pointing drift, have an impact at shorter separations. Even though the contrast is still acceptable (degradation by a factor 5 at $5\lambda/D$, where the contrast requirement is defined), the best option will be to perform HCI observations without misaligned segments. A final interesting analysis is when all instrumental effects are combined (see Sect. 6.3). In this case, we have used the best guess for their nominal values: a pupil with seven misaligned segments under a nominal seeing of 0"65, with 2 mas RMS pointing jitter, 0.4 mas PtV of slow pointing drifts, 20 nm PtV of NCPA drifts (in which the petal piston drift are included), and 2% PtV pupil drift. The simulation shows that the contrast requirement is still achievable, but with a very small margin. We underline that some effects are still missing in our simulations, such as water vapor turbulence, or some SCAO-specific effects, which could decrease the performance, when added to the other effects. There is however also room for improvement, as only the classical ADI postprocessing algorithm has been used for the contrast curves, and more advances algorithms could sensibly ameliorate the result.

Finally, we have simulated the expected observational capabilities of the METIS instrument in Chap. 7. A hypothetic Earth analog around α Cen b, with 1.5×10^{-7} contrast at 0.8" separation, is above the detection threshold when considering only SCAO residuals, for an integration time as short as 5h. However, it is drowned in the residual speckles when all effects are considered. A closer planet at 0.4" with higher contrast level of 6×10^{-7} is more easily detected, even when all effects are considered. β Pic planet b, simulated in L band at three different angular separations, and in N2 band at one angular separation, is clearly detected, even with all instrumental effects considered. The HR8799 case shows that METIS would be able to observe planets with similar contrast level (1×10^{-4}) much closer to the star. Except for ϵ Indi A, whose planet is clearly detected even when all instrumental effects are included, the other radial velocity planet-star system (HD128311, HD87883, and ϵ Eridani) cases demonstrate that the detectability of such planets will mostly depend on the capability of METIS to reduce instrumental effects, which are still partly unknown.

Based on the estimated performance presented in this work, the METIS instrument will provide a major leap in sensitivity to faint companions in the thermal infrared regime. When compared to on-sky results on current large telescopes (Absil et al., 2016), an estimated gain of a factor 100 to 1000 in terms of contrast at 0.1" will allow the detection of planetary-mass objects around the snow line for stars up to 30 pc in L band, and possibly rocky planets around closer stars in N band.

8.2 Perspective

In order to improve the METIS exoplanet detection capabilities, other coronagraphic solutions could be implemented, without modifying the optical train, by simply adding a mask in a pupil plane (CFO-PP1, and/or LMS-PP1 and IMG-PP1) and/or a focal plane (CFO-FP2).

8.2.1 Higher order vortex coronagraph: charge-4 and charge-6

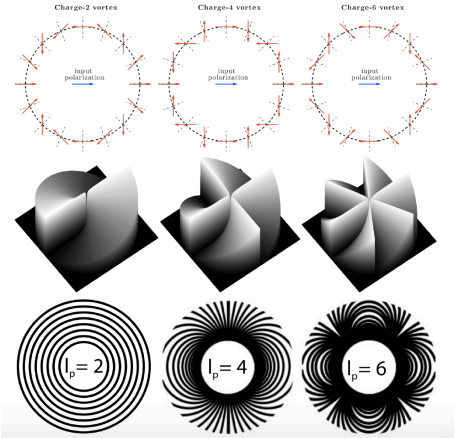

FIGURE 8.1: Charge 2 (left), charge 4 (center) and charge 6 (right) vortex coronagraphs representation (from Delacroix et al., 2014).

Bright stars, such as α Cen, will be partially resolved in the near-infrared by the next generation giant telescopes, leading to reduced HCI performance. To mitigate this effect and the intrinsic sensitivity to low order aberrations (tip-tilt, focus, coma, astigmatism) of the charge 2 vortex phase mask, more advanced focal-plane masks can be implemented. These devices are vortex phase masks where the topological charge is higher than 2 (see Chap. 3).

As illustrated in Fig. 8.1, the subwavelength gratings needed to implement higher charge vortex coronagraphs are not circularly symmetric. These theoretical grating designs cannot be produced in practice, due to state-of-the-art manufacturing limitations (e.g., there is a lower limit on the grating period due to the non-vertical grating walls). Several surrogate designs have been proposed for its fabrication on a diamond substrate (Delacroix et al., 2014).

Being similar to the VC2, these coronagraphs are two-stages devices: a phase mask at the CFO-FP2 and a Lyot stop at the IMG plane. As for the VC2, the Lyot stop is positioned after the pupil stabilization mirror, so it can be optimized to take into account the spiders.

The corresponding PSFs are presented in Fig. 8.2, while the associated performance will be discussed in Sect. 8.2.4.

8.2.2 Polynomial Apodized Vortex Coronagraph

As explained in Sect. 4.5.2, the starlight cancellation potential of the vortex coronagraph (like many other coronagraphs) is very sensitive to the presence of a central obscuration. In order to mitigate it, an apodizer can be implemented in an upstream

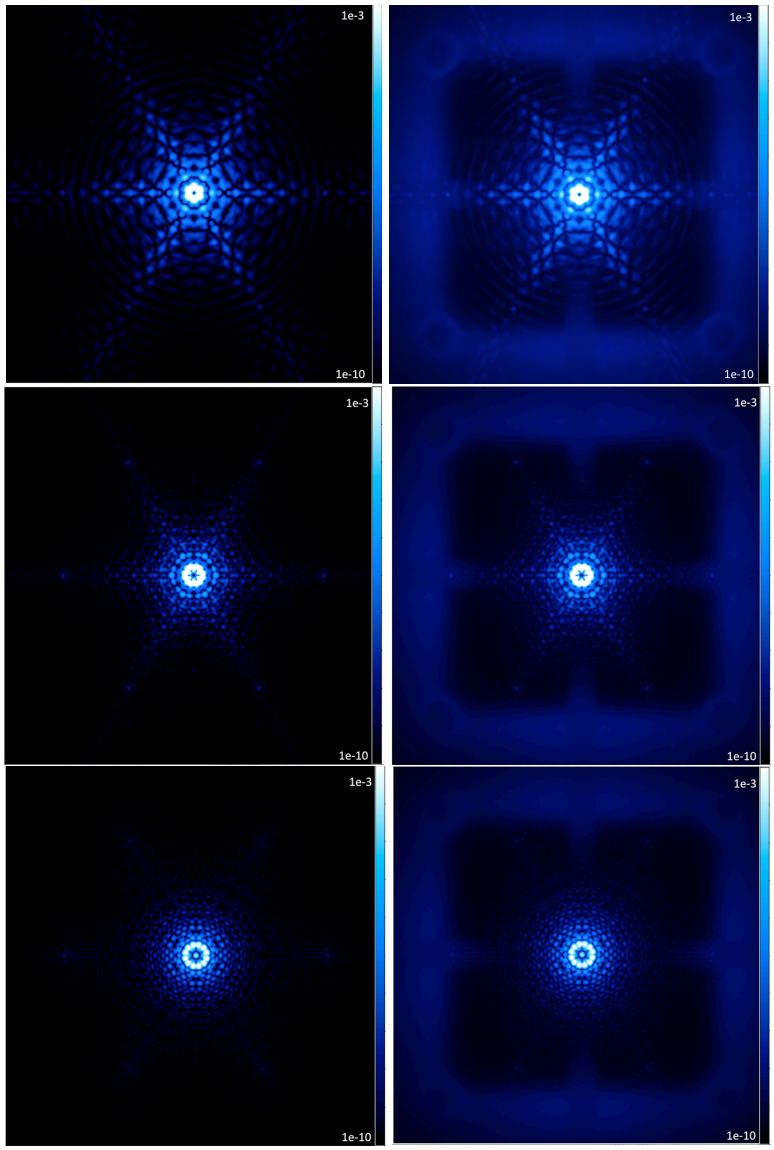

FIGURE 8.2: Representative PSFs at L band for the VC2 (top), VC4 (center), and VC6 (bottom): perfect case (left) and long exposure taking into account SCAO residuals only (right). All images have been cropped to a field-of-view of $100\lambda/D$, i.e., 2″1 at L band.

pupil plane. The RAVC provides a good compromise for charge-2 vortex coronagraph between starlight suppression and throughput. However, the extension of the RAVC concept to higher topological charge impacts negatively the final performance. In particular, the throughput rapidly decreases as the topological charge increases. For a 30% central obscuration (without spiders nor segmentation), the throughput of the RAVC2 is theoretically ∼40%, while it drops to ∼25% for a charge 4 RAVC (see Mawet et al., 2013b). A generalization of the RAVC is the PAVC (Polynomial Apodizer Vortex Coronagraph, see Fogarty et al., 2014 and Fogarty et al., 2017): it uses piecewise polynomial functions to optimize the contrast and keep a high throughput even for higher topological charge vortex coronagraphs. For large central obscurations (typically 30%), PAVC6 keeps a relatively high throughput (∼70%), while PAVC4 drops to ∼50%, at the expense of the IWA ($\sim 2\lambda/D$ for PAVC4 and $\sim 4\lambda/D$ for PAVC6). The PAVC6 seems to be a good compromise for larger central

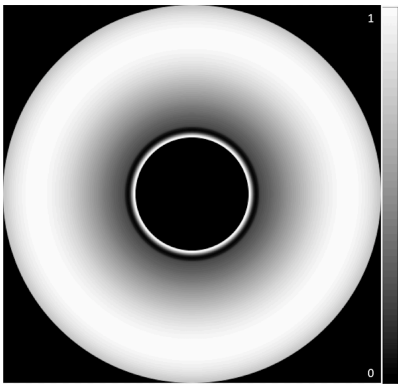

FIGURE 8.3: PAVC6 mask.

obscurations.

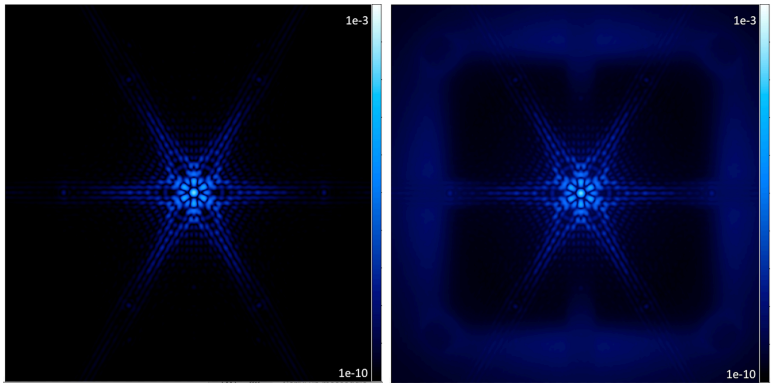

FIGURE 8.4: Representative PSFs at L band for the PAVC6: perfect case (left) and long exposure taking into account SCAO residuals only (right). All images have been cropped to a field-of-view of $100\lambda/D$, i.e., 2"1 at L band.

Similarly to the RAVC2, the PAVC6 is a three-stage device: the apodizer at the CFO-PP1, the vortex phase mask at the CFO-FP2, and the Lyot stop at the IMG plane. As for the RAVC2, the Lyot stop is positioned after the pupil stabilization mirror, so it can be optimized to take into account the spiders, while the apodizer is upstream and it can only be optimized for the rotationally symmetrical pupil of the ELT (no spiders optimization). The apodization mask for the ELT-METIS (without spiders and segments) is presented in Fig. 8.3. The perfect PSF and the long exposure PSF are presented in Fig. 8.4.

8.2.3 Lyot Plane Mask

Since both the RAVC2 and the PAVC6 apodizers are located upstream of the pupil stabilization mirror, they cannot be optimized to take into account the detrimental effect of the spider arms. Without changing the optical train of the METIS instrument, the only option to improve the contrast would be to optimize the Lyot Stop. For the VC and RAVC/PAVC, the Lyot stop is an amplitude mask, without any apodization. However, a phase apodization can be implemented (see Ruane et al., 2015). As for the APP, this apodization can be designed to clear out the full FoV (*Full LPM*) or half

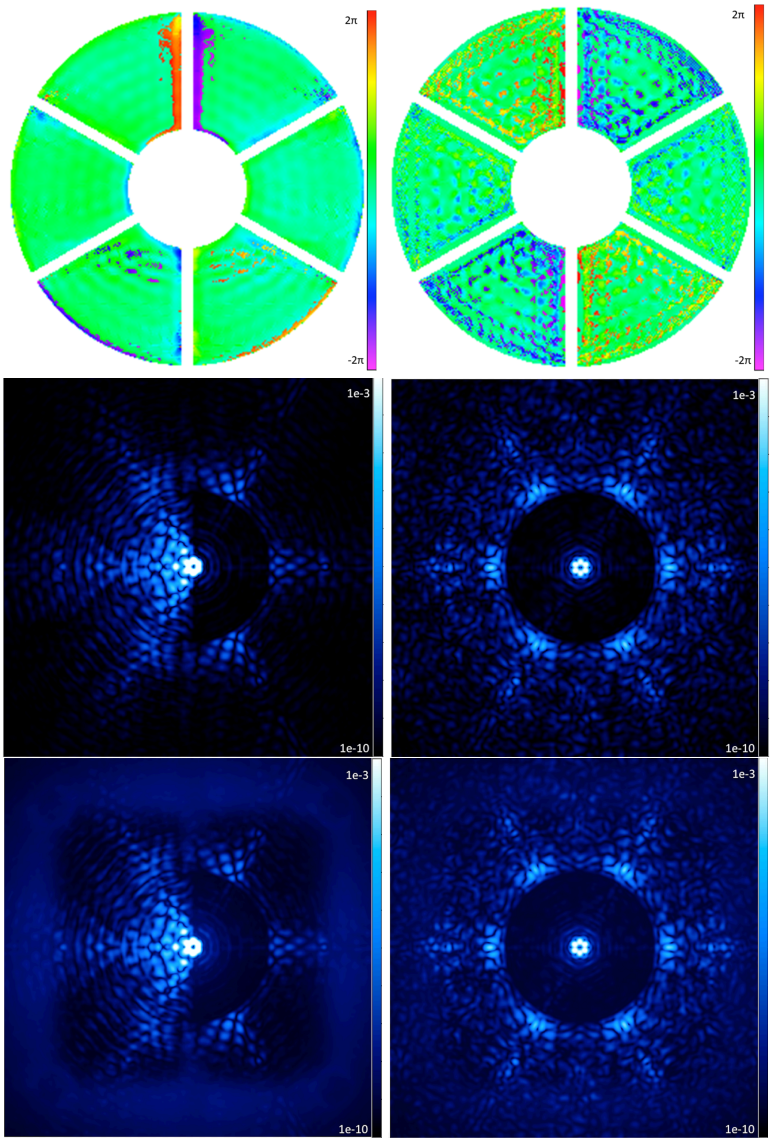

FIGURE 8.5: Pupil phase masks (top) and representative PSFs at L band for the VC2+LPM half FoV (left) and full FoV (right): perfect case (center) and long exposure (bottom). All PSFs images have been cropped to a field-of-view of $100\lambda/D$, i.e., 2″1 at L band.

of it (*Half LPM*). The optimized masks, presented in Fig. 8.5, top row, were designed to create a dark hole between 2 and $20\lambda/D$ (in order to remain inside the DM footprint). The optimization was performed in Matlab, using an iterative phase retrieval algorithm. Being a phase mask, the throughput is virtually 100%, being limited only by the amplitude Lyot stop, as for the VC2.

8.2.4 Performance

Using the 1-hour SCAO sequence, we simulated the L band performance of these coronagraphic concepts.
Figures 8.6 and 8.7 show the raw contrast (top) and ADI contrast curves (bottom) for the vortex coronagraphic concepts presented here: vortex coronagraph of charge 2 (VC2), 4 (VC4), and 6 (VC6), RAVC charge 2 (RAVC2), PAVC charge 6 (PAVC6),

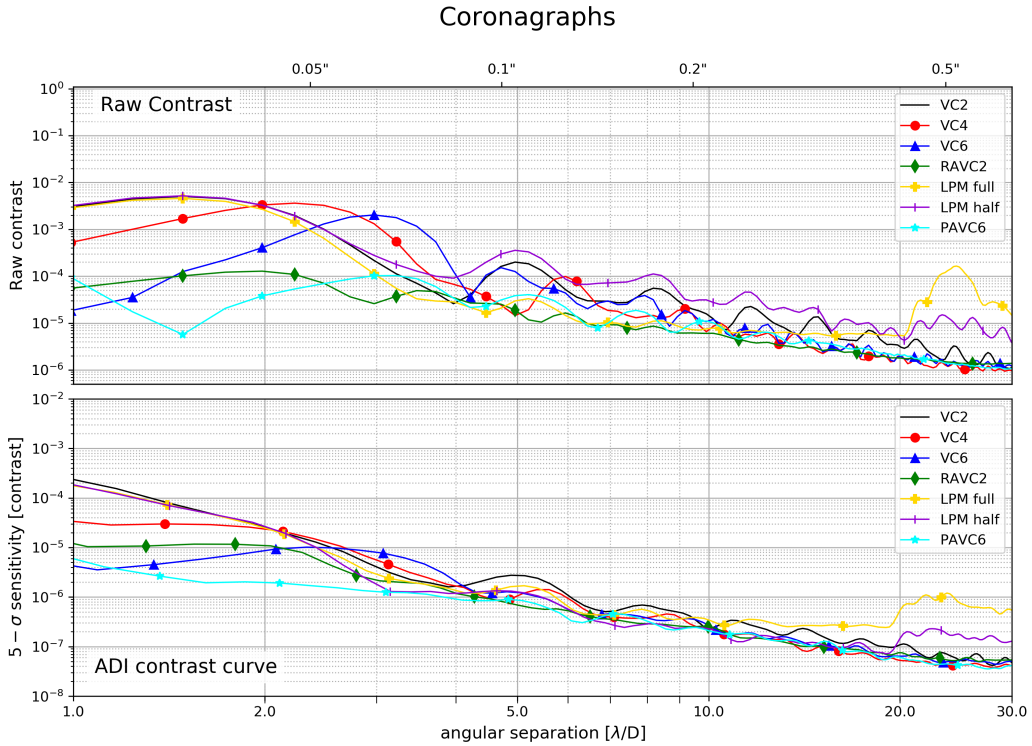

FIGURE 8.6: Raw contrast (top) and ADI contrast curve with SCAO only (bottom) for VC2, VC4, VC6, RAVC2, PAVC6, VC2+LPM half annulus, and VC2 + LPM full annulus observing modes at L band.

and the vortex coronagraph charge 2 with LPM with half (VC2+LPM half) and full (VC2+LPM full) annulus dark hole. Fig. 8.6 presents the results for SCAO only simulations, while in Fig. 8.7, a combination of effects is considered.

TABLE 8.1: α Cen simulated planets summary (contrast level derived from Des Marais et al., 2002).

Planet	SCAO simulation	Coronagraphic mode	Contrast level	Separation ["]	SNR
b	SCAO only	VC2	1.5×10^{-7}	0.8	5.65
b	SCAO + combination effects	VC2	1.5×10^{-7}	0.8	3.26
b	SCAO only	PAVC6	1.5×10^{-7}	0.8	7.03
b	SCAO + combination effects	PAVC6	1.5×10^{-7}	0.8	4.01

We can distinguish three zones in these graphs: one below $4\lambda/D$, one between $4\lambda/D$ and $20\lambda/D$, and one beyond $20\lambda/D$. In the middle zone ($4\lambda/D$ to $20\lambda/D$), the seven coronagraphic concepts have similar contrast, while in the other two zones the results are a bit different. Beyond $20\lambda/D$, as expected, the LPM concept sees a drop in the performance, because of its intrinsic design (optimization between $2\lambda/D$ and $20\lambda/D$). Below $4\lambda/D$, we can see that the PAVC6 shows the best behaviour,

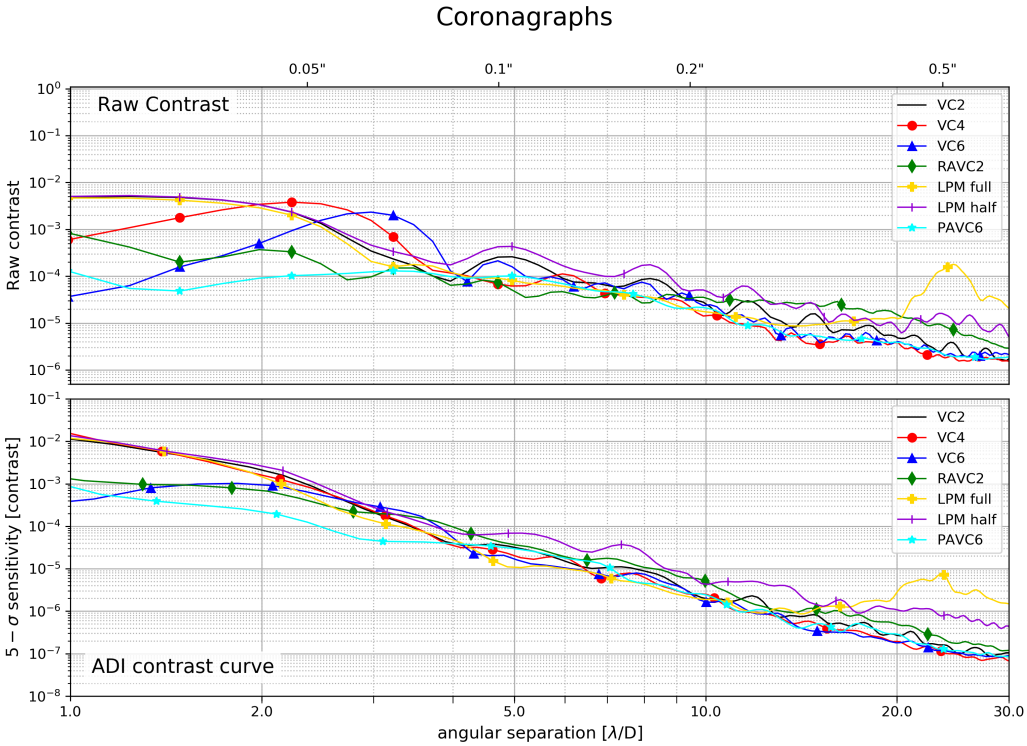

FIGURE 8.7: Raw contrast (top) and ADI contrast curve (bottom) in presence of combination of effects for VC2, VC4, VC6, RAVC2, PAVC6, VC2+LPM half annulus, and VC2 + LPM full annulus observing modes at L band.

with almost one order of magnitude better contrast performance with respect to the other concept. At $5\lambda/D$, where our requirement is defined, all coronagraphic concepts are compliant. However, the goal requirement of 1×10^{-6} at $2\lambda/D$ is never reached: the PAVC6 is the closest, with 2×10^{-6} with SCAO only, but this value increases by 2 orders of magnitudes when a combination of effects is considered. Each coronagraphic mode is more sensitive to different effects: for example, the PAVC6 and RAVC2 are more sensitive to pupil drift.

The better performance of the PAVC6 can be outlined with the hypothetical Earth-like planet around α Cen (see Tab. 8.1): the planet is clearly visible in the FoV (see Fig. 8.8, top, and Fig. 8.9). However, barely any improvement can be seen when a combination of effects is taken into account (see Fig. 8.8, bottom, and Fig. 8.9). Again, this demonstrates that a better understanding and so a better control of the instrumental effects would be extremely beneficial to the detection capability of the METIS instrument.

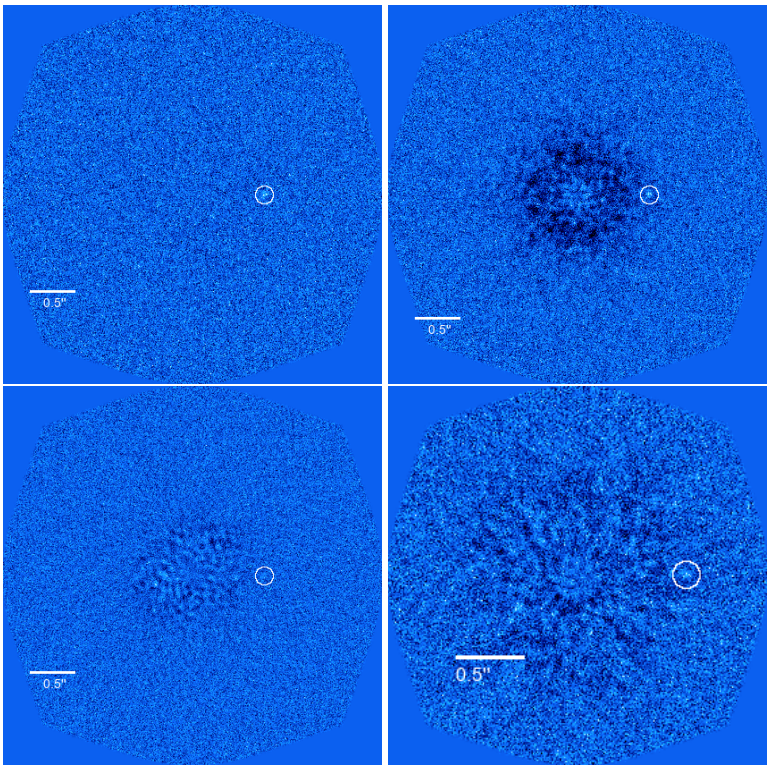

FIGURE 8.8: α Cen planet b ADI post-processed images in N2 band with PAVC6 (left) and VC2 (right) in 10h of observing time at 0.8″ with 1.5×10^{-7} constrast level with SCAO only (top) and in presence of a combination of effects (bottom).

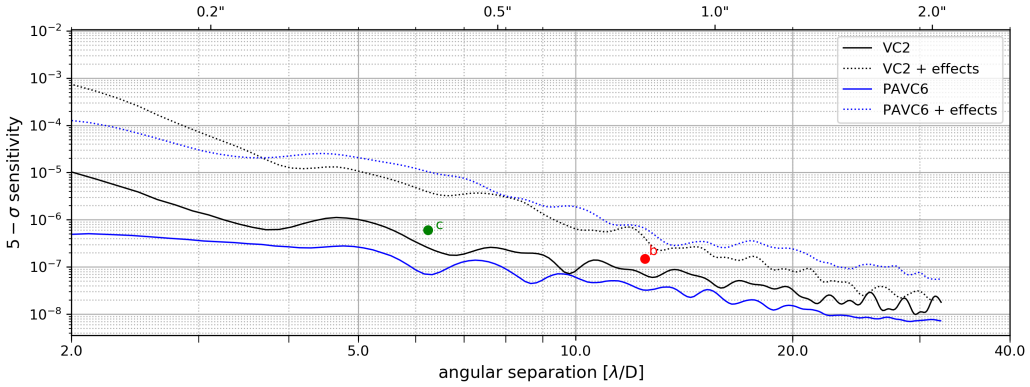

FIGURE 8.9: 5-σ detectability in terms of contrast for point-like companions around αCen in 10h observing time for the VC2, and PAVC6 in presence of SCAO (solid lines), and combination of effects (dotted lines). The two simulated planets are shown for comparison.

Bibliography

Absil, Olivier et al. (2016). "Three years of harvest with the vector vortex coronagraph in the thermal infrared". In: *Ground-based and Airborne Instrumentation for Astronomy VI*. Vol. 9908. Proc. SPIE, 99080Q. DOI: 10.1117/12.2233289.

Amara, Adam and Sascha P. Quanz (2012). "PYNPOINT: an image processing package for finding exoplanets". In: *mnras* 427, pp. 948–955. DOI: 10.1111/j.1365-2966.2012.21918.x. arXiv: 1207.6637 [astro-ph.IM].

Anglada-Escudé, Guillem et al. (2016). "A terrestrial planet candidate in a temperate orbit around Proxima Centauri". In: 536.7617, pp. 437–440. DOI: 10.1038/nature19106. arXiv: 1609.03449 [astro-ph.EP].

Aumann, H. H. (1985). "IRAS observations of matter around nearby stars." In: 97, pp. 885–891. DOI: 10.1086/131620.

Auvergne, M. et al. (2009). "The CoRoT satellite in flight: description and performance". In: 506.1, pp. 411–424. DOI: 10.1051/0004-6361/200810860. arXiv: 0901.2206 [astro-ph.SR].

Beuzit, J. L. (2013). "SPHERE: a Planet Finder Instrument for the VLT". In: *European Planetary Science Congress*, EPSC2013–954.

Beuzit, J. L. et al. (2019). "SPHERE: the exoplanet imager for the Very Large Telescope". In: 631, A155, A155. DOI: 10.1051/0004-6361/201935251. arXiv: 1902.04080 [astro-ph.IM].

Binks, A. S. and R. D. Jeffries (2014). "A lithium depletion boundary age of 21 Myr for the Beta Pictoris moving group". In: 438.1, pp. L11–L15. DOI: 10.1093/mnrasl/slt141. arXiv: 1310.2613 [astro-ph.SR].

Borucki, William J. et al. (2010). "Kepler Planet Detection Mission: Introduction and First Results". In: *American Astronomical Society Meeting Abstracts #215*. Vol. 215. American Astronomical Society Meeting Abstracts, p. 101.01.

Boss, Alan P. (2001). "Gas Giant Protoplanet Formation: Disk Instability Models with Thermodynamics and Radiative Transfer". In: 563.1, pp. 367–373. DOI: 10.1086/323694.

Bowens, R. et al. (2021). "Exoplanets with ELT-METIS. I. Estimating the direct imaging exoplanet yield around stars within 6.5 parsecs". In: 653, A8, A8. DOI: 10.1051/0004-6361/202141109. arXiv: 2107.06375 [astro-ph.EP].

Bowler, Brendan P. (2016). "Imaging Extrasolar Giant Planets". In: 128.968, p. 102001. DOI: 10.1088/1538-3873/128/968/102001. arXiv: 1605.02731 [astro-ph.EP].

Brandl, Bernhard R. et al. (2008). "METIS: the Mid-infrared E-ELT Imager and Spectrograph". In: Proc. SPIE 7014, 70141N, 70141N. DOI: 10.1117/12.789241. arXiv: 0807.3271 [astro-ph].

Brandl, Bernhard R. et al. (2018). "Status of the mid-IR ELT imager and spectrograph (METIS)". In: Proc. SPIE 10702, 107021U, 107021U. DOI: 10.1117/12.2311492.

Burrows, Adam, David Sudarsky, and Ivan Hubeny (2004). "Spectra and Diagnostics for the Direct Detection of Wide-Separation Extrasolar Giant Planets". In: *Astrophysical Journal* 609, pp. 407–416. DOI: 10.1086/420974.

Butler, R. Paul et al. (2003). "Seven New Keck Planets Orbiting G and K Dwarfs". In: 582.1, pp. 455–466. DOI: 10.1086/344570.

Carlomagno, Brunella et al. (2014). "Mid-IR AGPMs for ELT applications". In: *Ground-based and Airborne Instrumentation for Astronomy V*. Ed. by Suzanne K. Ramsay, Ian S. McLean, and Hideki Takami. Vol. 9147. Society of Photo-Optical Instrumentation Engineers (SPIE) Conference Series, p. 914799. DOI: 10.1117/12.2056280. arXiv: 1604.08355 [astro-ph.IM].

Carlomagno, Brunella et al. (2020). "METIS high-contrast imaging: design and expected performance". In: *Journal of Astronomical Telescopes, Instruments, and Systems* 6, 035005, p. 035005. DOI: 10.1117/1.JATIS.6.3.035005.

Carlotti, Alexis et al. (2012). "Fully optimized shaped pupils: preparation for a test at the Subaru Telescope". In: *Ground-based and Airborne Instrumentation for Astronomy IV*. Ed. by Ian S. McLean, Suzanne K. Ramsay, and Hideki Takami. Vol. 8446. Society of Photo-Optical Instrumentation Engineers (SPIE) Conference Series, p. 84463C. DOI: 10.1117/12.927129.

Carter, Aarynn L. et al. (2022). "The JWST Early Release Science Program for Direct Observations of Exoplanetary Systems I: High Contrast Imaging of the Exoplanet HIP 65426 b from 2-16 μm". In: *arXiv e-prints*, arXiv:2208.14990, arXiv:2208.14990. DOI: 10.48550/arXiv.2208.14990. arXiv: 2208.14990 [astro-ph.EP].

Charbonneau, David et al. (2009). "A super-Earth transiting a nearby low-mass star". In: 462.7275, pp. 891–894. DOI: 10.1038/nature08679. arXiv: 0912.3229 [astro-ph.EP].

Chauvin, G. et al. (2004). "A giant planet candidate near a young brown dwarf. Direct VLT/NACO observations using IR wavefront sensing". In: 425, pp. L29–L32. DOI: 10.1051/0004-6361:200400056. arXiv: astro-ph/0409323 [astro-ph].

Chauvin, G. et al. (2017). "Discovery of a warm, dusty giant planet around HIP 65426". In: 605, L9, p. L9. DOI: 10.1051/0004-6361/201731152. arXiv: 1707.01413 [astro-ph.EP].

Codona, Johanan L. and Matthew Kenworthy (2013). "Focal Plane Wavefront Sensing Using Residual Adaptive Optics Speckles". In: *Astrophysical Journal* 767, 100, p. 100. DOI: 10.1088/0004-637X/767/2/100.

Cumming, Andrew et al. (2008). "The Keck Planet Search: Detectability and the Minimum Mass and Orbital Period Distribution of Extrasolar Planets". In: 120.867, p. 531. DOI: 10.1086/588487. arXiv: 0803.3357 [astro-ph].

Currie, Thayne et al. (2014). "Deep Thermal Infrared Imaging of HR 8799 bcde: New Atmospheric Constraints and Limits on a Fifth Planet". In: 795.2, 133, p. 133. DOI: 10.1088/0004-637X/795/2/133. arXiv: 1409.5134 [astro-ph.EP].

Damasso, Mario et al. (2020). "A low-mass planet candidate orbiting Proxima Centauri at a distance of 1.5 AU". In: *Science Advances* 6.3, eaax7467. DOI: 10.1126/sciadv.aax7467.

Danielski, Camilla et al. (2018). "Atmospheric Characterization of Directly Imaged Exoplanets with JWST/MIRI". In: 156.6, 276, p. 276. DOI: 10.3847/1538-3881/aae651. arXiv: 1810.00894 [astro-ph.EP].

Davies, Richard and Markus Kasper (2012). "Adaptive Optics for Astronomy". In: 50, pp. 305–351. DOI: 10.1146/annurev-astro-081811-125447. arXiv: 1201.5741 [astro-ph.IM].

de Wit, Julien et al. (2018). "Atmospheric reconnaissance of the habitable-zone Earth-sized planets orbiting TRAPPIST-1". In: *Nature Astronomy* 2, pp. 214–219. DOI: 10.1038/s41550-017-0374-z. arXiv: 1802.02250 [astro-ph.EP].

Defrère, D. et al. (2014). "L'-band AGPM vector vortex coronagraph's first light on LBTI/LMIRCam". In: Proc. SPIE 9148, 91483X, p. 91483X. DOI: 10.1117/12.2057205. arXiv: 1410.6244 [astro-ph.EP].

Dekany, R. et al. (2011). "Palm-3000 on-sky results". In: *Second International Conference on Adaptive Optics for Extremely Large Telescopes*. P. 4.

Delacroix, C. et al. (2012). "A diamond AGPM coronagraph for VISIR". In: vol. 8446. Proc. SPIE, 84468K–9.

Delacroix, Christian et al. (2014). "Development of a subwavelength grating vortex coronagraph of topological charge 4 (SGVC4)". In: *Ground-based and Airborne Instrumentation for Astronomy V*. Ed. by Suzanne K. Ramsay, Ian S. McLean, and Hideki Takami. Vol. 9147. Society of Photo-Optical Instrumentation Engineers (SPIE) Conference Series, 91478Y. DOI: 10.1117/12.2055798. arXiv: 1412.0384 [astro-ph.IM].

Des Marais, David J. et al. (2002). "Remote Sensing of Planetary Properties and Biosignatures on Extrasolar Terrestrial Planets". In: *Astrobiology* 2.2, pp. 153–181. DOI: 10.1089/15311070260192246.

Doelman, David S. et al. (2017). "Patterned liquid-crystal optics for broadband coronagraphy and wavefront sensing". In: Proc. SPIE 10400, 104000U, 104000U. DOI: 10.1117/12.2273406.

Endl, M. et al. (2002). "The planet search program at the ESO Coudé Echelle spectrometer. III. The complete Long Camera survey results". In: 392, pp. 671–690. DOI: 10.1051/0004-6361:20020937. arXiv: astro-ph/0207512 [astro-ph].

Fang, Julia and Jean-Luc Margot (2012). "Architecture of Planetary Systems Based on Kepler Data: Number of Planets and Coplanarity". In: 761.2, 92, p. 92. DOI: 10.1088/0004-637X/761/2/92. arXiv: 1207.5250 [astro-ph.EP].

Feng, Fabo et al. (2019). "Detection of the nearest Jupiter analogue in radial velocity and astrometry data". In: 490.4, pp. 5002–5016. DOI: 10.1093/mnras/stz2912. arXiv: 1910.06804 [astro-ph.EP].

Fischer, D. A. et al. (2014). "Exoplanet Detection Techniques". In: *Protostars and Planets VI*. Ed. by Henrik Beuther et al., p. 715. DOI: 10.2458/azu_uapress_9780816531240-ch031. arXiv: 1505.06869 [astro-ph.EP].

Fischer, Debra et al. (2009). "Five Planets and an Independent Confirmation of HD 196885Ab from Lick Observatory". In: 703.2, pp. 1545–1556. DOI: 10.1088/0004-637X/703/2/1545. arXiv: 0908.1596 [astro-ph.EP].

Fischer, Debra A. and Jeff Valenti (2005). "The Planet-Metallicity Correlation". In: 622.2, pp. 1102–1117. DOI: 10.1086/428383.

Fogarty, Kevin, Laurent Pueyo, and Dimitri Mawet (2014). "Optimal apodizations for on-axis vector vortex coronagraphs". In: *Space Telescopes and Instrumentation 2014: Optical, Infrared, and Millimeter Wave*. Ed. by Jr. Oschmann Jacobus M. et al. Vol. 9143. Society of Photo-Optical Instrumentation Engineers (SPIE) Conference Series, p. 914326. DOI: 10.1117/12.2056760.

Fogarty, Kevin et al. (2017). "Polynomial Apodizers for Centrally Obscured Vortex Coronagraphs". In: *Astrophysical Journal* 154.6, 240, p. 240. DOI: 10.3847/1538-3881/aa9063. arXiv: 1703.02994 [astro-ph.IM].

Foo, Gregory, David M. Palacios, and Grover A. Swartzlander (2005). "Optical vortex coronagraph". In: *Optics Letters* 30.24, pp. 3308–3310. DOI: 10.1364/OL.30.003308. URL: http://ol.osa.org/abstract.cfm?URI=ol-30-24-3308.

Forsberg, P. and M. Karlsson (2013). "High aspect ratio optical gratings in diamond". In: *Diamond and Related Materials* 34, pp. 19–24.

Forsberg, P. et al. (2014). "Manufacturing of diamond annular groove phase masks for the mid infrared region: 5 years of successful process development of diamond plasma etching". In: vol. 9151. Proc. SPIE, p. 44.

Gillon, Michaël et al. (2016). "Temperate Earth-sized planets transiting a nearby ultracool dwarf star". In: *Nature* 533, p. 221.

Goldreich, P. and S. Tremaine (1979). "The excitation of density waves at the Lindblad and corotation resonances by an external potential." In: 233, pp. 857–871. DOI: 10.1086/157448.

Gomez Gonzalez, C.A. et al. (2017). "VIP : Vortex Image Processing Package for High-contrast Direct Imaging". In: *Astronomical Journal* 154.1, p. 7.

Goździewski, Krzysztof and Cezary Migaszewski (2014). "Multiple mean motion resonances in the HR 8799 planetary system". In: 440.4, pp. 3140–3171. DOI: 10.1093/mnras/stu455. arXiv: 1308.6462 [astro-ph.EP].

Gratadour, D. et al. (2014). "COMPASS: an efficient, scalable and versatile numerical platform for the development of ELT AO systems". In: Proc. SPIE 9148, 91486O, 91486O. DOI: 10.1117/12.2056358.

Guyon, Olivier (2005). "Limits of Adaptive Optics for High-Contrast Imaging". In: *Astrophysical Journal* 629.1, pp. 592–614. DOI: 10.1086/431209. arXiv: astro-ph/0505086 [astro-ph].

Guyon, Olivier et al. (2010). "High Performance PIAA Coronagraphy with Complex Amplitude Focal Plane Masks". In: 190.2, pp. 220–232. DOI: 10.1088/0067-0049/190/2/220.

Hanel, R. A. et al. (1992). *Exploration of the solar system by infrared remote sensing*.

Hatzes, Artie P. et al. (2000). "Evidence for a Long-Period Planet Orbiting Eridani". In: 544.2, pp. L145–L148. DOI: 10.1086/317319. arXiv: astro-ph/0009423 [astro-ph].

Hippler, Stefan et al. (2019). "Single conjugate adaptive optics for the ELT instrument METIS". In: *Experimental Astronomy* 47.1-2, pp. 65–105. DOI: 10.1007/s10686-018-9609-y. arXiv: 1810.07578 [astro-ph.IM].

Hornburg, Kathryn J., Ravi K. Komanduri, and Michael J. Escuti (2014). "Multiband retardation control using multi-twist retarders". In: 9099, 90990Z, 90990Z. DOI: 10.1117/12.2051170.

Howard, Andrew W. (2013). "Observed Properties of Extrasolar Planets". In: *Science* 340.6132, pp. 572–576. DOI: 10.1126/science.1233545. arXiv: 1305.0542 [astro-ph.EP].

Hubbard, W. B., A. Burrows, and J. I. Lunine (2002). "Theory of Giant Planets". In: 40, pp. 103–136. DOI: 10.1146/annurev.astro.40.060401.093917.

Huby, E. et al. (2015). "Post-coronagraphic tip-tilt sensing for vortex phase masks: The QACITS technique". In: *Astronomy and Astrophysics* 584, A74, A74. DOI: 10.1051/0004-6361/201527102.

Huby, E. et al. (2017). "On-sky performance of the QACITS pointing control technique with the Keck/NIRC2 vortex coronagraph". In: *Astronomy and Astrophysics* 600, A46, A46. DOI: 10.1051/0004-6361/201630232. arXiv: 1701.06397 [astro-ph.IM].

Hutterer, Victoria et al. (2018a). "Advanced wavefront reconstruction methods for segmented Extremely Large Telescope pupils using pyramid sensors". In: *Journal of Astronomical Telescopes, Instruments, and Systems* 4.4, pp. 1–18. DOI: 10.1117/1.JATIS.4.4.049005.

— (2018b). "Wavefront reconstruction for ELT-sized telescopes with pyramid wavefront sensors". In: *Adaptive Optics Systems VI*. Vol. 10703. Proc. SPIE, p. 1070344. DOI: 10.1117/12.2312423.

Johnson, John Asher et al. (2010). "Giant Planet Occurrence in the Stellar Mass-Metallicity Plane". In: 122.894, p. 905. DOI: 10.1086/655775. arXiv: 1005.3084 [astro-ph.EP].

Jovanovic, N. et al. (2015). "The Subaru Coronagraphic Extreme Adaptive Optics System: Enabling High-Contrast Imaging on Solar-System Scales". In: 127.955, p. 890. DOI: 10.1086/682989. arXiv: 1507.00017 [astro-ph.IM].

Kasdin, N. Jeremy et al. (2004). "The shaped pupil coronagraph for planet finding coronagraphy: optimization, sensitivity, and laboratory testing". In: *Optical, Infrared, and Millimeter Space Telescopes*. Ed. by John C. Mather. Vol. 5487. Society of Photo-Optical Instrumentation Engineers (SPIE) Conference Series, pp. 1312–1321. DOI: 10.1117/12.552273.

Kasper, M. et al. (2017). "NEAR: Low-mass Planets in α Cen with VISIR". In: *The Messenger* 169, pp. 16–20. DOI: 10.18727/0722-6691/5033.

Kasper, M. et al. (2019). "NEAR: First Results from the Search for Low-Mass Planets in α Cen". In: *The Messenger* 178, pp. 5–9. DOI: 10.18727/0722-6691/5163.

Kasting, James F., Daniel P. Whitmire, and Ray T. Reynolds (1993). "Habitable Zones around Main Sequence Stars". In: 101.1, pp. 108–128. DOI: 10.1006/icar.1993.1010.

Kenworthy, M.A. et al. (2007). "First On-Sky High-Contrast Imaging with an Apodizing Phase Plate". In: *Astrophysical Journal* 660, pp. 762–769.

Keppler, M. et al. (2018). "Discovery of a planetary-mass companion within the gap of the transition disk around PDS 70". In: *Astronomy and Astrophysics* 617, A44, A44. DOI: 10.1051/0004-6361/201832957. arXiv: 1806.11568 [astro-ph.EP].

Krist, John E. (2007). "PROPER: an optical propagation library for IDL". In: *Optical Modeling and Performance Predictions III*. Vol. 6675. Proc. SPIE, 66750P. DOI: 10.1117/12.731179.

Kuhn, J. R., D. Potter, and B. Parise (2001). "Imaging Polarimetric Observations of a New Circumstellar Disk System". In: 553.2, pp. L189–L191. DOI: 10.1086/320686. arXiv: astro-ph/0105239 [astro-ph].

Lafrenière, David et al. (2007). "A New Algorithm for Point-Spread Function Subtraction in High-Contrast Imaging: A Demonstration with Angular Differential Imaging". In: 660.1, pp. 770–780. DOI: 10.1086/513180. arXiv: astro-ph/0702697 [astro-ph].

Lafrenière, David et al. (2009). "HST/NICMOS Detection of HR 8799 b in 1998". In: 694.2, pp. L148–L152. DOI: 10.1088/0004-637X/694/2/L148. arXiv: 0902.3247 [astro-ph.EP].

Lagage, P. O. et al. (2004). "Successful Commissioning of VISIR: The Mid-Infrared VLT Instrument". In: *The Messenger* 117, pp. 12–16.

Lagrange, A. M. et al. (2009). "A probable giant planet imaged in the β Pictoris disk. VLT/NaCo deep L'-band imaging". In: 493.2, pp. L21–L25. DOI: 10.1051/0004-6361:200811325. arXiv: 0811.3583 [astro-ph].

Lagrange, A. M. et al. (2019). "Evidence for an additional planet in the β Pictoris system". In: *Nature Astronomy* 3, pp. 1135–1142. DOI: 10.1038/s41550-019-0857-1.

Léger, A. et al. (2009). "Transiting exoplanets from the CoRoT space mission. VIII. CoRoT-7b: the first super-Earth with measured radius". In: 506.1, pp. 287–302. DOI: 10.1051/0004-6361/200911933. arXiv: 0908.0241 [astro-ph.EP].

Lin, D. N. C. and J. Papaloizou (1979). "Tidal torques on accretion discs in binary systems with extreme mass ratios." In: 186, pp. 799–812. DOI: 10.1093/mnras/186.4.799.

Lin, D. N. C. and John Papaloizou (1986). "On the Tidal Interaction between Protoplanets and the Protoplanetary Disk. III. Orbital Migration of Protoplanets". In: 309, p. 846. DOI: 10.1086/164653.

Lin, Douglas. and Don. Dixon (2009). "La naissance des planètes : tohu-bohu dans les nuages". In: *Dossier Pour la Science*.

Llop-Sayson, Jorge et al. (2021). "Constraining the Orbit and Mass of epsilon Eridani b with Radial Velocities, Hipparcos IAD-Gaia DR2 Astrometry, and Multiepoch

Vortex Coronagraphy Upper Limits". In: 162.5, 181, p. 181. DOI: 10.3847/1538-3881/ac134a. arXiv: 2108.02305 [astro-ph.EP].

Lovis, C. et al. (2009). "Towards the characterization of the hot Neptune/super-Earth population around nearby bright stars". In: *Transiting Planets*. Ed. by Frédéric Pont, Dimitar Sasselov, and Matthew J. Holman. Vol. 253, pp. 502–505. DOI: 10.1017/S1743921308027051.

Lyot, Bernard (1939). "The study of the solar corona and prominences without eclipses (George Darwin Lecture, 1939)". In: 99, p. 580. DOI: 10.1093/mnras/99.8.580.

Macintosh, B. et al. (2015). "Discovery and spectroscopy of the young jovian planet 51 Eri b with the Gemini Planet Imager". In: *Science* 350.6256, pp. 64–67. DOI: 10.1126/science.aac5891. arXiv: 1508.03084 [astro-ph.EP].

Macintosh, Bruce et al. (2014). "First light of the Gemini Planet Imager". In: *Proceedings of the National Academy of Science* 111.35, pp. 12661–12666. DOI: 10.1073/pnas.1304215111. arXiv: 1403.7520 [astro-ph.EP].

Maire, A. L. et al. (2015). "The LEECH Exoplanet Imaging Survey. Further constraints on the planet architecture of the HR 8799 system (Corrigendum)". In: 579, C2, p. C2. DOI: 10.1051/0004-6361/201425185e.

Malhotra, Renu (1993). "The origin of Pluto's peculiar orbit". In: 365.6449, pp. 819–821. DOI: 10.1038/365819a0.

Marois, C. et al. (2006). "Angular Differential Imaging: A Powerful High-Contrast Imaging Technique". In: *Astrophysical Journal* 641, pp. 556–564. DOI: 10.1086/500401. eprint: astro-ph/0512335.

Marois, Christian et al. (2000). "Differential imaging coronagraph for the detection of faint companions". In: *Optical and IR Telescope Instrumentation and Detectors*. Ed. by Masanori Iye and Alan F. Moorwood. Vol. 4008. Society of Photo-Optical Instrumentation Engineers (SPIE) Conference Series, pp. 788–796. DOI: 10.1117/12.395537.

Marois, Christian et al. (2008). "Direct Imaging of Multiple Planets Orbiting the Star HR 8799". In: *Science* 322.5906, p. 1348. DOI: 10.1126/science.1166585. arXiv: 0811.2606 [astro-ph].

Masset, F. S. and J. C. B. Papaloizou (2003). "Runaway Migration and the Formation of Hot Jupiters". In: 588.1, pp. 494–508. DOI: 10.1086/373892. arXiv: astro-ph/0301171 [astro-ph].

Mawet, D. et al. (2005a). "Annular Groove Phase Mask Coronagraph". In: *Astrophysical Journal* 633, pp. 1191–1200. DOI: 10.1086/462409.

Mawet, D. et al. (2005b). "Subwavelength surface-relief gratings for stellar coronagraphy". In: *Applied Optics* 44, pp. 7313–7321. DOI: 10.1364/AO.44.007313.

Mawet, D. et al. (2013a). "L'-band AGPM vector vortex coronagraph's first light on VLT/NACO. Discovery of a late-type companion at two beamwidths from an F0V star". In: *Astronomy and Astrophysics* 552, L13, p. L13. DOI: 10.1051/0004-6361/201321315. arXiv: 1304.0930 [astro-ph.IM].

Mawet, D. et al. (2013b). "Ring-Apodized Vortex Coronagraphs for Obscured Telescopes. I. Transmissive Ring Apodizers". In: *Astrophysical Journal Supplement Series* 209. DOI: 10.1088/0067-0049/209/1/7.

Mawet, D. et al. (2014). "Fundamental Limitation of High-contrast imaging at small angles set by small sample statistics". In: *Astrophysical Journal* 792.

Mawet, Dimitri et al. (2010). "The Vector Vortex Coronagraph: sensitivity to central obscuration, low- order aberrations, chromaticism, and polarization". In: *Modern Technologies in Space- and Ground-based Telescopes and Instrumentation*. Vol. 7739. Proc. SPIE, p. 773914. DOI: 10.1117/12.858240.

Mawet, Dimitri et al. (2011). "Improved high-contrast imaging with on-axis telescopes using a multistage vortex coronagraph". In: *Optics Letters* 36.8, p. 1506. DOI: 10.1364/OL.36.001506. arXiv: 1103.1909 [astro-ph.IM].

Mawet, Dimitri et al. (2019). "Deep Exploration of Eridani with Keck Ms-band Vortex Coronagraphy and Radial Velocities: Mass and Orbital Parameters of the Giant Exoplanet". In: 157.1, 33, p. 33. DOI: 10.3847/1538-3881/aaef8a. arXiv: 1810.03794 [astro-ph.EP].

Mayor, Michel and Didier Queloz (1995). "A Jupiter-mass companion to a solar-type star". In: 378.6555, pp. 355–359. DOI: 10.1038/378355a0.

Meshkat, T. et al. (2013). "Further Evidence of the Planetary Nature of HD 95086 b from Gemini/NICI H-band Data". In: *Astrophysical Journal* 775, L40, p. L40. DOI: 10.1088/2041-8205/775/2/L40.

Michel, K. U. and M. Mugrauer (2021). "Search for (sub)stellar companions of exoplanet hosts by exploring the second ESA-Gaia data release". In: *Frontiers in Astronomy and Space Sciences* 8, 14, p. 14. DOI: 10.3389/fspas.2021.624907. arXiv: 2102.04385 [astro-ph.EP].

Milli, J. et al. (2018). "Low wind effect on VLT/SPHERE: impact, mitigation strategy, and results". In: *Adaptive Optics Systems VI*. Vol. 10703. Proc. SPIE, 107032A. DOI: 10.1117/12.2311499. arXiv: 1806.05370 [astro-ph.IM].

Moharam, M. G. and T. K. Gaylord (1982). "Diffraction analysis of dielectric surface-relief gratings". In: *Journal of the Optical Society of America* 72, p. 1385.

Murray, N. et al. (1998). "Migrating Planets". In: *Science* 279, p. 69. DOI: 10.1126/science.279.5347.69. arXiv: astro-ph/9801138 [astro-ph].

Nakajima, T. et al. (1995). "Discovery of a cool brown dwarf". In: 378.6556, pp. 463–465. DOI: 10.1038/378463a0.

N'diaye, M. et al. (2010). "Experimental results with a second-generation Roddier & Roddier phase mask coronagraph". In: 509, A8, A8. DOI: 10.1051/0004-6361/200911874.

Nielsen, Eric L. et al. (2017). "Evidence That the Directly Imaged Planet HD 131399 Ab Is a Background Star". In: 154.6, 218, p. 218. DOI: 10.3847/1538-3881/aa8a69. arXiv: 1705.06851 [astro-ph.EP].

Pathak, P. et al. (2021). "High-contrast imaging at ten microns: A search for exoplanets around Eps Indi A, Eps Eri, Tau Ceti, Sirius A, and Sirius B". In: 652, A121, A121. DOI: 10.1051/0004-6361/202140529. arXiv: 2104.13032 [astro-ph.EP].

Pearl, J. C. and P. R. Christensen (1997). "Mars Global Surveyor Thermal Emission Spectrometer: Observations of Earth". In: *AAS/Division for Planetary Sciences Meeting Abstracts #29*. Vol. 29. AAS/Division for Planetary Sciences Meeting Abstracts, p. 06.20.

Quanz, Sascha P. et al. (2015). "Direct detection of exoplanets in the 3-10 μm range with E-ELT/METIS". In: *International Journal of Astrobiology* 14.2, pp. 279–289. DOI: 10.1017/S1473550414000135. arXiv: 1404.0831 [astro-ph.IM].

Ragazzoni, R. (1996). "Pupil plane wavefront sensing with an oscillating prism". In: *Journal of Modern Optics* 43, pp. 289–293.

Rameau, J. et al. (2013). "Confirmation of the Planet around HD 95086 by Direct Imaging". In: *Astrophysical Journal* 779, L26, p. L26. DOI: 10.1088/2041-8205/779/2/L26.

Rasio, Frederic A. and Eric B. Ford (1996). "Dynamical instabilities and the formation of extrasolar planetary systems". In: *Science* 274, pp. 954–956. DOI: 10.1126/science.274.5289.954.

Roberts, Jennifer E. et al. (2012). "Results from the PALM-3000 high-order adaptive optics system". In: *Adaptive Optics Systems III*. Ed. by Brent L. Ellerbroek, Enrico

Marchetti, and Jean-Pierre Véran. Vol. 8447. Society of Photo-Optical Instrumentation Engineers (SPIE) Conference Series, 84470Y. DOI: 10.1117/12.926477.

Roddier, F. and C. Roddier (1997). "Stellar Coronograph with Phase Mask". In: 109, pp. 815–820. DOI: 10.1086/133949.

Rouan, Daniel et al. (2007). "The Four Quadrant Phase Mask Coronagraph and its avatars". In: *Comptes Rendus Physique* 8.3-4, pp. 298–311. DOI: 10.1016/j.crhy.2007.05.004.

Ruane, G. J. et al. (2015). "Lyot-plane phase masks for improved high-contrast imaging with a vortex coronagraph". In: 583, A81, A81. DOI: 10.1051/0004-6361/201526561. arXiv: 1509.05750 [astro-ph.IM].

Safronov, Viktor Sergeevich (1969). *Evoliutsiia doplanetnogo oblaka.*

Sahlmann, J. et al. (2013). "Astrometric orbit of a low-mass companion to an ultracool dwarf". In: 556, A133, A133. DOI: 10.1051/0004-6361/201321871. arXiv: 1306.3225 [astro-ph.SR].

Seager, Sara and Drake Deming (2010). "Exoplanet Atmospheres". In: 48, pp. 631–672. DOI: 10.1146/annurev-astro-081309-130837. arXiv: 1005.4037 [astro-ph.EP].

Sivaramakrishnan, Anand et al. (2001). "Ground-based Coronagraphy with High-order Adaptive Optics". In: 552.1, pp. 397–408. DOI: 10.1086/320444. arXiv: astro-ph/0103012 [astro-ph].

Smith, B. A. and R. J. Terrile (1984). "A Circumstellar Disk around β Pictoris". In: *Science* 226.4681, pp. 1421–1424. DOI: 10.1126/science.226.4681.1421.

Smith, W. Hayden (1987). "Spectral differential imaging detection of planets about nearby stars." In: 99, pp. 1344–1353. DOI: 10.1086/132124.

Soummer, R., C. Aime, and P. E. Falloon (2003). "Stellar coronagraphy with prolate apodized circular apertures". In: 397, pp. 1161–1172. DOI: 10.1051/0004-6361:20021573.

Soummer, Rémi, Laurent Pueyo, and James Larkin (2012). "Detection and Characterization of Exoplanets and Disks Using Projections on Karhunen-Loève Eigenimages". In: *Astrophysical Journal* 755, L28, p. L28. DOI: 10.1088/2041-8205/755/2/L28. arXiv: 1207.4197 [astro-ph.IM].

Su, K. Y. L. et al. (2009). "The Debris Disk Around HR 8799". In: 705.1, pp. 314–327. DOI: 10.1088/0004-637X/705/1/314. arXiv: 0909.2687 [astro-ph.EP].

Thompson, William et al. (2023). "Deep Orbital Search for Additional Planets in the HR 8799 System". In: 165.1, 29, p. 29. DOI: 10.3847/1538-3881/aca1af. arXiv: 2210.14213 [astro-ph.EP].

Udalski, A. et al. (1992). "The Optical Gravitational Lensing Experiment". In: 42, pp. 253–284.

Van Eylen, Vincent et al. (2019). "The Orbital Eccentricity of Small Planet Systems". In: 157.2, 61, p. 61. DOI: 10.3847/1538-3881/aaf22f. arXiv: 1807.00549 [astro-ph.EP].

Vandenbussche, B. et al. (2010). "The β Pictoris disk imaged by Herschel PACS and SPIRE". In: 518, L133, p. L133. DOI: 10.1051/0004-6361/201014626. arXiv: 1005.3915 [astro-ph.SR].

Vérinaud, Christophe (2004). "On the nature of the measurements provided by a pyramid wave-front sensor". In: *Optics Communications* 233.1-3, pp. 27–38. DOI: 10.1016/j.optcom.2004.01.038.

Viswanath, Gayathri et al. (2021). "Constraints on the nearby exoplanet Indi Ab from deep near- and mid-infrared imaging limits". In: 651, A89, A89. DOI: 10.1051/0004-6361/202140730. arXiv: 2105.09773 [astro-ph.EP].

Vogt, Steven S. et al. (2005). "Five New Multicomponent Planetary Systems". In: 632.1, pp. 638–658. DOI: 10.1086/432901.

Wagner, K. et al. (2021). "Author Correction: Imaging low-mass planets within the habitable zone of α Centauri". In: *Nature Communications* 12, 2651, p. 2651. DOI: 10.1038/s41467-021-23145-5.

Walker, H. J. and I. Heinrichsen (2000). "ISOPHOT Observations of Dust Disks around Main Sequence (Vega-Like) Stars". In: 143.1, pp. 147–154. DOI: 10.1006/icar.1999.6235.

Wanke, H. (1981). "Constitution of Terrestrial Planets". In: *Philosophical Transactions of the Royal Society of London Series A* 303.1477, pp. 287–301. DOI: 10.1098/rsta.1981.0203.

Ward, William R. (1997). "Protoplanet Migration by Nebula Tides". In: 126.2, pp. 261–281. DOI: 10.1006/icar.1996.5647.

Weidenschilling, Stuart J. and Francesco Marzari (1996). "Gravitational scattering as a possible origin for giant planets at small stellar distances". In: 384.6610, pp. 619–621. DOI: 10.1038/384619a0.

Wolszczan, A. and D. A. Frail (1992). "A planetary system around the millisecond pulsar PSR1257 + 12". In: 355.6356, pp. 145–147. DOI: 10.1038/355145a0.

Wright, J. T. et al. (2011). "The Exoplanet Orbit Database". In: 123.902, p. 412. DOI: 10.1086/659427. arXiv: 1012.5676 [astro-ph.SR].

Zuckerman, B. et al. (2011). "The Tucana/Horologium, Columba, AB Doradus, and Argus Associations: New Members and Dusty Debris Disks". In: 732.2, 61, p. 61. DOI: 10.1088/0004-637X/732/2/61. arXiv: 1104.0284 [astro-ph.SR].